Master Thesis

Mechanical and Elemental Changes at the Bone-Implant Interface in Response to a Low-Alloyed Biodegradable Magnesium Implant in a Growing Rat Model

carried out for the purpose of obtaining the degree of Diplom-Ingenieurin

submitted at TU Wien

Faculty of Mechanical and Industrial Engineering

by

Nicole Zechmann

Matr.Nr.: 00935224

under the supervision of

Univ. Prof. Mag. Dr.rer.nat. Helga Lichtenegger

Dipl.-Ing. Thomas Bretschneider

Institute of Physics and Materials Science (IPM)
University of Natural Resources and Life Science

Vienna, September 2023

Nicole Zechmann

I confirm that the printing of this thesis requires the approval of the examination board.

Affidavit

I declare in lieu of oath, that I wrote this thesis and performed the associated research myself, using only the literature cited in this volume. If text passages from sources are used literally, they are marked as such.

I confirm that this work is original and has not been submitted for examination elsewhere, nor is it currently under consideration for a thesis elsewhere.

I acknowledge that the submitted work will be checked electronically-technically using suitable and state-of-the-art means (plagiarism detection software). On the one hand, this ensures that the submitted work was prepared according to the high-quality standards within the applicable rules to ensure good scientific practice "Code of Conduct" at the TU Wien. On the other hand, a comparison with other student theses avoids violations of my personal copyright.

Vienna, September 2023

Nicole Zechmann

Acknowledgements

First, I want to express my gratitude to my supervisor Helga Lichtenegger for enabling me to work on this exciting project, for her warm welcome, expert advice, and patience. Thanks also to Thomas Bretschneider for supporting me in the execution of my thesis. Appreciation is also extended to the members of the institute for immediately integrating me into the group, for the pleasant working atmosphere, and for always being very kind and helpful. I thank my office mates for the encouragement and pleasant conversations during lunch breaks.

Additionally, I would like to especially thank Verena Maier-Kiener, Anna-Sophie, Burtschi, and Chrisi for the opportunity to perform nanoindentation measurements at the Montanuniversität Leoben and for their technical advice and support.

Furthermore, I would like to thank my friends for their support during my work. My deepest thanks go to my parents and grandparents, who had always stood by me throughout my entire studies with their motivating and encouraging words, who were always proud of me even when I was not, and for their financial support, which made my second degree at TU Vienna possible. Lastly, I would like to thank Christian from the bottom of my heart for his incredible patience, encouragement, understanding, help, always being there for me, and unconditional love.

Abstract

Over the last decade, the demand for developing new, alternative, and biodegradable implant materials in orthopedics and trauma care has become increasingly important to overcome the disadvantages associated with conventional materials. Recently, magnesium (Mg)-based alloys have attracted significant attention as superior alternative materials and are promising candidates to ensure the complex requirements of a biocompatible, homogenously degradable, load-bearing, and functionally supportive implant. These implants completely degrade, eliminating the need for additional removal surgery.

The thesis focuses on characterizing the bone's nanostructural response toward a homogenously degrading Mg-0.45Zn-0.45Ca implant, in wt% (referred to as ZX00 alloy), in a small animal model over a period of 52 weeks. Special attention is paid to the changes in mechanical properties and chemical composition over time at the bone-implant interface, which are crucial factors for the future application of Mg-based implants. For this purpose, nanoindentation experiments were performed to assess the influence of implant degradation on the mechanical properties of the bone, particularly its stiffness and hardness. Furthermore, energy-dispersive X-ray spectroscopy (EDX) measurements were used to evaluate the effects of the degrading implant on the chemical composition.

Kurzfassung

In den letzten Jahren hat die Nachfrage nach der Entwicklung neuer, biologisch abbaubarer Implantate im Bereich der Orthopädie und der Traumaversorgung stetig zugenommen, um die mit herkömmlichen Materialien verbundenen Nachteile zu überwinden. Magnesium (Mg)-Basis-legierungen sind vielversprechende Kandidaten, um die komplexen Anforderungen an ein biokompatibles, homogen abbaubares, tragfähiges und funktionell unterstützendes Implantat zu gewährleisten. Aufgrund vollständiger Degradation dieser Materialien kann eine zusätzliche Operation zur Entfernung des Implantates vermieden werden.

Ziel dieser Arbeit ist es, die nanostrukturellen Änderungen des Knochens auf ein sich langsam abbauendes Implantat aus Mg-0.45Zn-0.45Ca, in wt% (ZX00), im Kleintiermodell über einen Zeitraum von 52 Wochen zu charakterisieren. Besonderes Augenmerk wird auf den Einfluss auf die mechanischen Eigenschaften und die chemische Zusammensetzung an der Grenzfläche zwischen Knochen und Implantat über die Zeit und den damit resultierenden Einsatzmöglichkeiten im Hinblick auf eine zukünftige Verwendung von Mg-basierten Implantaten gelegt. Hierzu wurden Nanoindentierungen durchgeführt, um den Einfluss des Abbaus des Implantates auf die mechanischen Eigenschaften des Knochens, insbesondere auf E-Modul und Härte, beurteilen zu können. Zusätzlich erfolgten energiedispersive röntgenspektroskopische (EDX) Messungen, um die Auswirkungen des sich abbauenden Implantats auf die chemische Zusammensetzung zu bewerten.

Table of Contents

List of abbreviations

BSE	Backscattered electron
Ca	Calcium
E	Young's modulus
EDX	Energy-dispersive X-ray spectroscopy
E_r	Reduced modulus
H_2	Hydrogen
HAp	Hydroxyapatite
h_c	Contact displacement
h_e	Elastic displacement
h_f	Final displacement
h_{max}	Maximum displacement
h_s	Sink-in displacement
μCT	Micro-computed tomography
Mg	Magnesium
MgO	Magnesium oxide
$Mg(OH)_2$	Magnesium hydroxide
$MgCl_2$	Magnesium chloride
O	Oxygen
OH	Hydroxide
OPM	Oliver-Pharr method
P	Load
P	Phosphorus
P_{max}	Maximum load
R^2	Coefficient of determination
S	Contact stiffness
SE	Secondary electron
SEM	Scanning electron microscopy
wt%	Weight percent
Z	Atomic number
Zn	Zinc
ZX00	Mg-0.45wt%Zn-0.45wt%Ca
ν	Poissons's ratio

1 Introduction

The first chapter describes the motivation and aim of the present thesis.

1.1 Motivation

In recent years, the incidence of sports- and leisure injuries has steadily grown [1, 2]. Approximately 10–25 % of all pediatric injuries result in fractures [3]. Therefore, biomedical implants are essential in improving people's health worldwide. The first successfully used material as an implant material was stainless steel [4]. This material prevails due to its high mechanical stress, comparatively cost-effectiveness, relatively simple manufacturing, and availability [5]. Nevertheless, there exist some drawbacks. Stainless steel and other commonly used implant materials like titanium are associated with the phenomena of stress shielding, leading to bone resorption and the requirement for a second implant removal surgery [6]. Bioresorbable polymers may cause inflammatory tissue reactions and are unsuitable for load-bearing applications due to their limited mechanical properties. Thus, new implant materials that combine excellent mechanical properties, biodegradability, and biocompatibility are still needed. An ideal implant should support the healing process, provide immediate stabilization, have an uncomplicated treatment, obviate implant exchange/removal, reduce hospitalization times, and minimize treatment and after-care costs [7]. Further, the implant should degrade uniformly, accompanied by gradual load transfer onto the healing bone, promoting the formation of new bone substance while being simultaneously resorbed. In the last few years, the market for biodegradable implants has constantly been growing, and much progress has been made in its development [7]. Maintaining the patient's quality of life places high demands on implants. In this context, bioresorbable implants play a crucial role. Mg-based alloys have attracted great attention and appear to be promising candidates to fulfill those multifaceted requirements adequately. Compared to commonly used titanium or stainless steel, the major advantages of these temporary degradable biomaterials are their mechanical properties, closely aligned with those of human bone, minimizing stress shielding effects, and their excellent biocompatibility [6,8]. Furthermore, a second surgical intervention for implant removal can be prevented since Mg-based implants completely degrade after a specific period.

1.2 Aim and Hypotheses

This study aims to elucidate the influence of a degrading ZX00 implant on the healing process over time and compare newly formed bone and bulk bone in terms of their mechanical performance. More specifically, the focus is on examining the stiffness, hardness, and chemical composition. The results should provide information about the effects of the degrading implant on bone tissue to evaluate its potential success for future applications. It was hypothesized that the indentation modulus and hardness of bone tissue will vary due to differences in the mineral content arising from tissue age, particularly in the context of fracture healing time. It is anticipated that mature bone tissue will display higher stiffness and rigidity compared to immature bone tissue. Additionally, it was hypothesized that the degradation of the ZX00 implant would not exert any adverse effects on bone healing and formation. For this purpose, a growing animal model was investigated over the course of 52 weeks.

2 Theoretical Principles

The following chapter provides an overview of theoretical principles regarding bone composition, hierarchical structure, mechanical properties, and the process of bone healing. Additionally, different types of implant materials, especially Mg alloys, and their behavior are described. Furthermore, the concepts behind the required measurement methods, such as nanoindentation, are explained.

2.1 Bone

The adult human skeleton comprises about 206 bones in different shapes and sizes [9]. Bones provide several essential functions, including structural support and protection of vital organs. Moreover, they offer an environment for blood-forming bone marrow (hematopoiesis) and act as a reservoir for minerals like calcium (Ca), magnesium (Mg), and phosphorus (P). As a fundamental part of the locomotor system, bones provide attachment sites for muscles and assist in movement [10–12]. In the last decades, more focus has been laid on fracture stabilization due to the growing number of sports and leisure-related injuries [1,2]. Thus, to achieve satisfactory results in terms of bone healing and meet the continuously increasing requirements, a comprehensive understanding of bone structures, properties, healing mechanisms, and their responses to factors such as different implant materials is crucial.

2.1.1 Composition

From an anatomical and macroscopic perspective, bone consists of various components, including osseous tissue, bone marrow, cartilage tissue, blood vessels, and nerves [12]. Histologically, bone can be differentiated into mineralized extracellular and cellular components (Figure 1), see Table 1). From an engineering point of view, bone is an exceptional material designed on the principle of lightweight construction: achieving maximal strength with minimal material usage. Bone demonstrates a high degree of fracture resistance and adaptability to external conditions, a concept first postulated by Wolff [13–15].

Table 1: Bone components and their major functions [16–18].

Component	Type	Major function
Cellular components	Osteoblasts Osteocytes Osteclasts	Bone forming cells Maintain bone tissue Bone resorbing cells
Matrix: Organic	Collagen type I Non-collagenous proteins	Tensile strength, flexibility Regulation of bone formation and mineralization
Matrix: Inorganic	Hydroxyapatite	Compressive strength and hardness
Water		Nutrient diffusion, contributing to viscoelastic properties, mediate mineral-organic matrix interaction

Extracellular Components

Bone is a heterogeneous nanocomposite material with different components contributing to its unique mechanical properties and functions. The extracellular matrix comprises about 65 wt% inorganic matrix, 25 wt% organic matrix, and 10 wt% water [19]. Thus, bone is a combination of elastic organic fibers that provide bone with flexibility and tensile strength, and a rigid inorganic phase that imparts rigidity, hardness, and compression strength [12]. The most abundant organic material in the mineralized extracellular matrix is collagen type I, with about 90–95 %. The rest of the organic matrix includes proteoglycans, lipids, and non-collagenous proteins, such as osteocalcin, osteopontin, and osteonectin [19, 20]. The predominant inorganic material is carbonated hydroxyapatite (HAp; $Ca_{10}(PO_4)_6(OH)_2$), where carbonate ions replace either the hydroxyl groups (A-type) or phosphate ions (B-type) in the crystal lattice. These crystals are deposited inside and around the collagen fibrils. Other substitutions are magnesium, sodium, potassium, fluoride, and chloride [21]. Water facilitates nutrient diffusion, contributes to viscoelastic properties, and mediates the interaction between bone mineral and collagen components [16, 22]. The relative proportions of these components vary with age, body region, gender, or disease [22].

Cellular Components

Bone cells make bone a dynamic living tissue due to the continuous process of tissue

resorption and deposition within a constant remodeling process. The cellular components can be divided into the three major cell types in bone tissue: osteoblasts, osteocytes, and osteoclasts (Figure 1). Osteoblasts, often referred to as "bone-forming cells", are responsible for synthesizing and secreting uncalcified organic components needed to build the extracellular matrix and they initiate calcification. Once these osteoblasts are surrounded and trapped by their secretions, they become osteocytes, which comprise the majority of cells within a mature skeleton, accounting for approximately 95 % [23]. The spaces in which they reside are known as lacunae, interconnected by canaliculi, which enable osteocytes to maintain the bone's daily metabolism, including nutrient and waste exchange with the bloodstream [12]. Osteocytes are responsible for mechanosensation and can secrete substances that regulate osteoblast and osteoclast activity. Osteoclasts enzymatically break down calcified bone tissue through a process known as bone resorption [17]. A summary of the main components of bone and their primary functions is presented in Table 1.

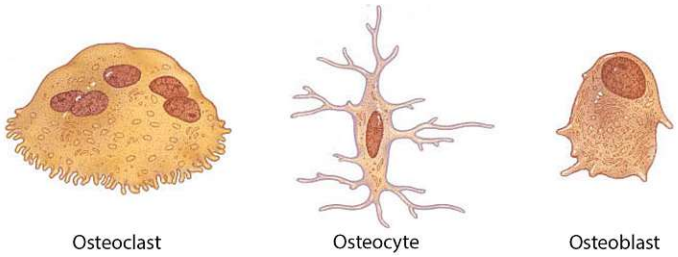

Figure 1: The major cell types. Osteoclasts are responsible for bone resorption, osteocytes are mature bone cells, and osteoblasts are bone matrix synthesizing cells. Adapted from [12].

2.1.2 Hierarchical Structure of Bone

The hierarchical arrangement within bone leads to extraordinary mechanical properties. Bone can be examined across several hierarchal levels of organization, each leading to a specific mechanical, biological, and chemical function, from the macroscopic shape of the bone to the nanometer-sized mineral platelets. Numerous classification schemes with varying subcategories exist, as described in several reviews [8, 24–27]. Figure 2 illustrates one of those classification systems of bone levels, taking a human femur as an example: Macroscale (femur: bone as an organ), mesoscale (cortical and trabecular bone), microscale (osteon and trabeculae), sub-microscale (single lamella), nanoscale (mineralized collagen fibril), and sub-nanoscale (type-I collagen and HAp).

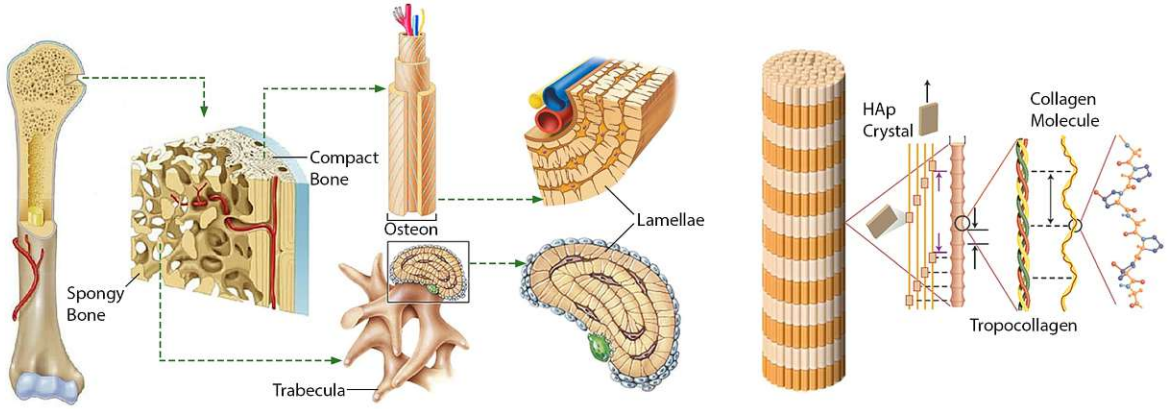

Figure 2: Hierarchical organization levels of bone. Adapted from [8, 12, 28, 29].

Macrostructure

Macroscopically, bone consists of bone tissue, connective tissue, bone marrow, cartilage tissue, blood vessels, and nerves [9]. Bones exhibit different mechanical and functional properties and can be distinguished based on their shapes and appearances. Morphologically, six different shapes can be distinguished: long, short, flat, pneumatic, irregular, and sesamoid bone [9].

Mesoscale

According to its structure, function, inner architecture, and porosity, bone can be classified as cortical (also referred to as dense or compact bone) or trabecular bone (also known as cancellous or spongy bone) (Figure 3) [8, 11, 12].

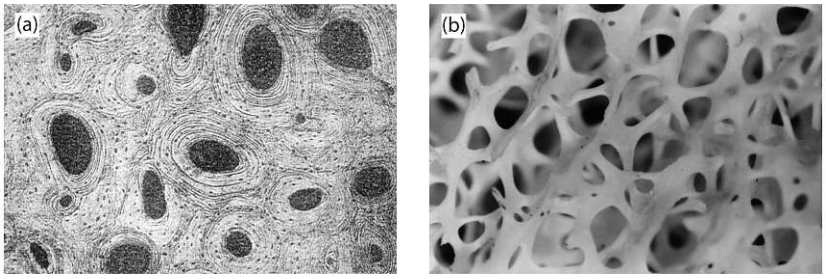

Figure 3: (a) A transverse cross-section showing compact bone, and (b) trabecular bone. Adapted from [30, 31].

Cortical bone constitutes about 80 % of skeletal bone mass [12, 20] and forms the cortex of bones, predominantly in the diaphysis of long bones. It is responsible for protection, support, structural rigidity, and resistance to the stresses associated with movement and weight. Despite having identical basic bone material composition, the two distinct types differ in microstructure and porosity. Cortical bone is comparatively stiffer, with

a markedly lower porosity of approximately 5–10 % compared to 50–90 % in trabecular bone [20, 32, 33]. Typically, the compressive strength and the modulus of elasticity of trabecular bone are lower than those of cortical bone [34–36]. Cortical bone is organized into osteons, whereas trabecular bone exhibits a spongy morphology characterized by interconnected delicate trabeculae. The mechanically most relevant bones - long bones - were chosen for a detailed explanation of the bone structure. A long bone is divided into an epiphysis at each end and a diaphysis as a long tubular central region. The diaphysis contains the medullary cavity filled with bone marrow surrounded by compact bone. The epiphysis exhibits a trabecular internal structure enclosed by a thin layer of cortical bone (Figure 4) [8, 12, 35].

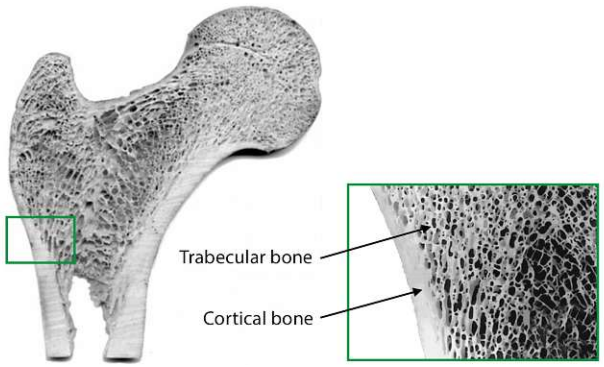

Figure 4: Cortical and trabecular bone of a proximal femur. Adapted from [8, 37].

Microstructure

This level of organization exhibits a structure comprising osteons or single trabeculae (Figure 5).

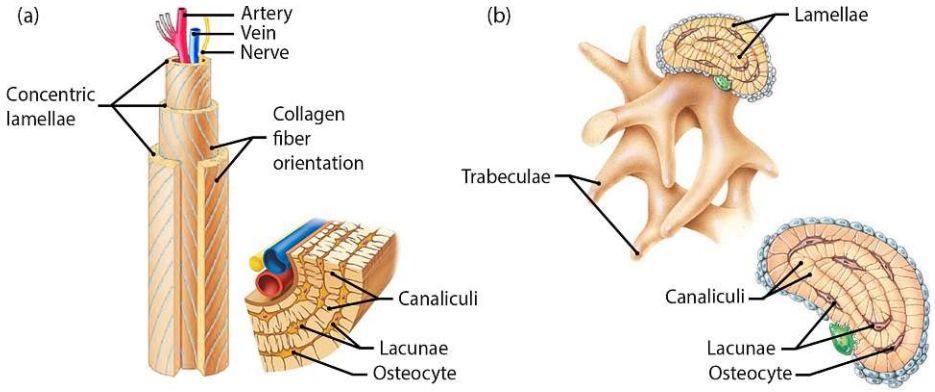

Figure 5: (a) Osteons in cortical bone: The bone tissue is structured with concentric lamellae encircling a Haversian canal. (b) Trabeculae in trabecular bone: The bone tissue is organized in irregularly arranged lamellae. Adapted from [12, 29].

Compact bone displays tube-like nutritive canals known as Haversian canals (diameter: $\approx 50\mu$m [8]) (Figure 5a), containing blood vessels and nerves. They are concentrically surrounded by 5–20 lamellae, like the growth rings of a tree trunk [23]. This main characteristic feature of compact bone is called osteon or Haversian system, preferably arranged along the bone's long axis. An osteon has a diameter of approximately 100–400 μm and a length of a few millimeters [8, 23, 38]. Volkmann's canals connect Haversian canals with each other. Small spaces called lacunae are found between the lamellae, housing osteocytes. The lacunae are interconnected and linked to the Haversian canals through canaliculi, providing routes for nutrients to reach osteocytes and for waste products to leave them (Figure 6).

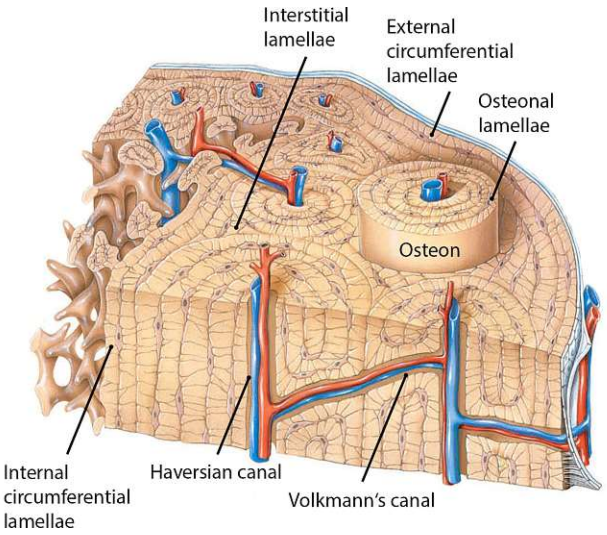

Figure 6: Section through a long bone's diaphysis highlighting various lamellar arrangements. The lamellae within an osteon encircle a Haversian canal, while Volkmann's canals interconnect these Haversian canals. Interstitial lamellae are located between neighboring osteons. Around the entire circumference of the bone shaft, circumferential lamellae can be found. Adapted from [12].

In contrast, trabecular bone lacks osteons. Instead, it consists of a foam-like interconnected network of approximately 50–300 μm thin compartments, known as trabeculae (Figure 5b). Bone marrow fills the interjacent spaces. These trabeculae are made up of packets with irregularly arranged lamellae [8, 12, 39]. The orientation of these trabeculae is impacted by the mechanical loading on the bone [12].

Sub-Microstructure

Both compact and trabecular bone consists of lamellar bone [23]. Within an osteon or a trabecula, each layer is referred to as a lamella (Figure 5). Each lamella has a thickness of approximately 3–7 μm [8] and is built up by mineralized collagen fibers embedded in

an extrafibrillar matrix. Giraud-Guille proposed a so-called “twisted plywood” model, in which a single lamella is composed of multiple sub-layers [40]. Within a thin sublayer, the fibers are predominantly oriented in the same direction and progressively rotate from one sub-layer to another around an axis perpendicular to these layers (Figure 7). The compound of uniformly aligned fibers in a sub-lamella is called a fiber array [40, 41]. Different types of lamellae can be distinguished: inner- and outer circumferential lamellae, osteonal lamellae, and interstitial lamellae (Figure 6) [12, 23].

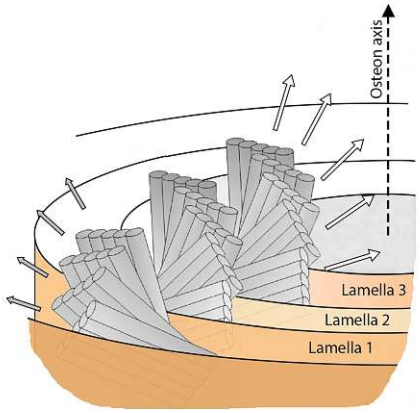

Figure 7: Individual lamellae, illustrated with varying shades of orange, consist of arrays of collagen fibers. These fibers exhibit a consistent orientation within a given sub-layer and transition to a different direction as they move from one sub-layer to the next. Adapted from [42].

Nanostructure

At the nanoscale, self-assembled structures known as collagen fibrils, with a typical tissue-dependent diameter of 50–500 nm, can be found [43, 44]. During a self-assembling process called fibrillogenesis, collagen molecules line up, forming distinct banding patterns with a periodicity of about 67 nm. This pattern can be explained by a quarter-staggered, side-by-side alignment of collagen triple helices. This arrangement leads to alternating regions of overlap zones of 27 nm with a high protein density and gap zones of 40 nm with a low protein density along the fiber axis [45]. The gap zone functions as a nucleation and growing site for the mineral platelets. This mineralized collagen fiber serves as a universal building element for compact and trabecular bones. A representation of the collagen fibril assembly is depicted in Figure 8.

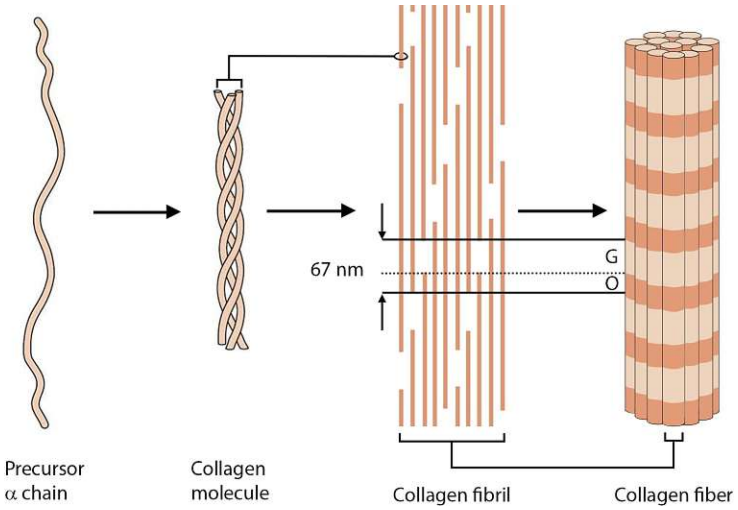

Figure 8: Self-assembly of collagen fibrils (after [46]). Collagen precursor chains are assembled to form triple-helical collagen molecules approximately 300 nm in length. These molecules align in a parallel fashion, following a quarter-staggered arrangement, leading to the formation of a collagen fibril with a staggered period of 67 nm. A periodic density variation along the fibril axis arises from the staggering. One molecule out of five is missing in the stripes, labeled G (gap zone), whereas in the areas labeled O (overlap zone), the molecules overlap. Thus, the density is accordingly higher. The collagen fibrils are then grouped in bundles to form the collagen fiber.

Sub-Nanostructure

Finally, the so-called elementary components can be identified at this observation scale of a few nanometers: collagen, mineral nanoparticles, non-collagenous proteins, and water. At the level of amino acids, type-I collagen is a protein with a highly repetitive sequence often characterized by the following pattern Gly-X-Pro or Gly-X-Hyp (Gly = glycine, Pro = proline, Hyp = hydroxyproline), where X represents various other amino acids [47]. A single collagen molecule, also called tropocollagen, has a length of about 300 nm and a diameter of about 1.2 nm [45,48,49]. Collagen provides tensile strength and flexibility. As mentioned above, the gap serves as a site for the nucleation and growth of mineral platelets during a process called calcification (Figure 9). With time, HAp crystals extend into the overlap zones and can either be found inside (intrafibrillar) or around (extrafibrillar) the collagen fibrils [8, 12].

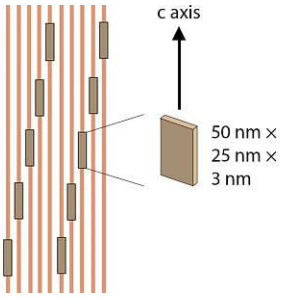

Figure 9: Schematic illustration depicting the mineralization of collagen fibrils with HAp nanoparticles within bone tissue. Adapted from [28].

The size of these mineral crystals is typically in the range of 1–5 nm in thickness, 25 nm in width, and 50 nm in length [28]. Their c-axis is parallel to the long axis of the collagen. The collagen orientation follows the direction of principal stress and adapts to changing conditions during tissue healing or throughout life [50–52]. Bone is an organic-inorganic composite showing excellent tensile and compressive strength. In summary, bone's outstanding qualities are based on the hierarchical structure and its components.

2.1.3 Maturation Level of Bone

Structurally, bone can be categorized into two main types according to the arrangement of the collagen fibers: woven and lamellar (Figure 10). Woven bone is a primary non-lamellar immature tissue type found in embryonic bone, pathological bone, and during fracture healing. This type of bone is later reorganized and remodeled into the biomechanically more resilient lamellar bone [17]. Woven bone is characterized by irregularly oriented collagen fibers in an interlacing network. In contrast, in lamellar bone, the collagen fibers assemble into regularly parallel arranged layers [23]. Lamellar bone represents the mature form and is the main bone type in adults [53].

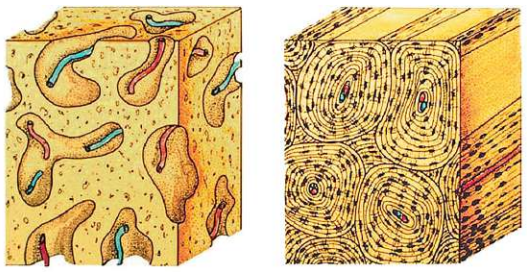

Figure 10: Woven (immature) bone shows irregularly oriented collagen fibers. Lamellar (mature) bone displays a well-organized arrangement of collagen fibers [53].

2.1.4 Bone Remodeling

Bone constantly adjusts itself in response to physiological and mechanical changes. It undergoes constant remodeling according to the principle "form follows function", which was stated in the late 19th century by Wolff and is nowadays known as Wolff's law [13, 17]. It is a continuous and well-coordinated mechanism involving the resorption and formation of bone tissue. Osteoclasts break down and remove old and damaged bone, whereas osteoblasts deposit new bone matrix that subsequently becomes mineralized. A balance between the two processes is maintained in healthy bone to guarantee no significant net

changes in bone mass [54]. Likewise, remodeling plays a role in restoring fully functional bone during fracture healing, as discussed in chapter 2.1.5.

2.1.5 Bone Healing

Bone healing is a complex process of rebuilding bone following a fracture and can be classified into primary (direct) and secondary (indirect) healing [55]. Bone injuries and defects are often a result of trauma, tumors, or infections. Bones possess the ability to repair themselves without the formation of scar tissue [56]. Injured bone has the capacity for complete regeneration to the properties prior to damage (restitution ad integrum), and the newly formed bone becomes eventually indistinguishable from the origin, uninjured bone [57]. A bone fracture disrupts the continuity of the tissue, impairs its supporting structure, ruptures blood vessels, and causes pain. The central goal of any fracture treatment is to restore bone continuity, thereby reinstating the function of the affected extremity or body section and alleviating pain [55,58]. Comprehending the healing process is essential for the development of bone-repairing materials.

Primary Healing

In the case of primary bone healing, absolute contact (fracture gap $< 200\,\mu$m [56]) via exact anatomical reduction and almost complete stability of the fracture ends is required to reestablish continuity between Haversian systems. In this process, no intermediate callus formation occurs [55, 56].

Secondary Healing

Secondary (indirect) healing occurs in the vast majority of bone injuries. It is observed when the fracture ends do not directly contact each other, and relative stability at the fracture exists. In diaphyseal fractures, a large amount of fracture callus is formed. It is typically characterized by distinct but overlapping stages (Figure 11): 1) hematoma formation and inflammation, 2) repair, and 3) remodeling. The stages are defined arbitrarily and exhibit variations in their description across different literature sources [17, 55, 56]. Stage 1) corresponds to Figure 11 (a). Stage 2) is depicted by (b) and (c), and stage 3) is represented by (d). Damaged blood vessels immediately lead to a hematoma formation at the fracture site, which is gradually replaced during the inflammatory phase by fibrin-rich granulation tissue at 3–7 days post-fracture. Osteoclasts start to resorb the necrotic

bone at the fracture ends. Following these initial phases, a soft callus (fibrocartilaginous callus) forms from the granulation tissue approximately 2–3 weeks after fracture. In rat models, the peak of soft callus formation occurs 7–10 days post-fracture [59]. When the fracture ends are bridged by a soft callus, Ca is deposited, leading to the development of a hard callus or woven bone. This hard callus stage might persist for about 12–16 weeks. In the last step of fracture repair, osteoclasts and osteoblasts remodel the immature, woven bone. Although the process is initiated as early as 3–4 weeks in animal models, it may take several months or even years to remodel the woven bone into a more organized lamellar bone adapted to the direction of loading and resembling the pre-fracture morphology [55, 56, 58, 60].

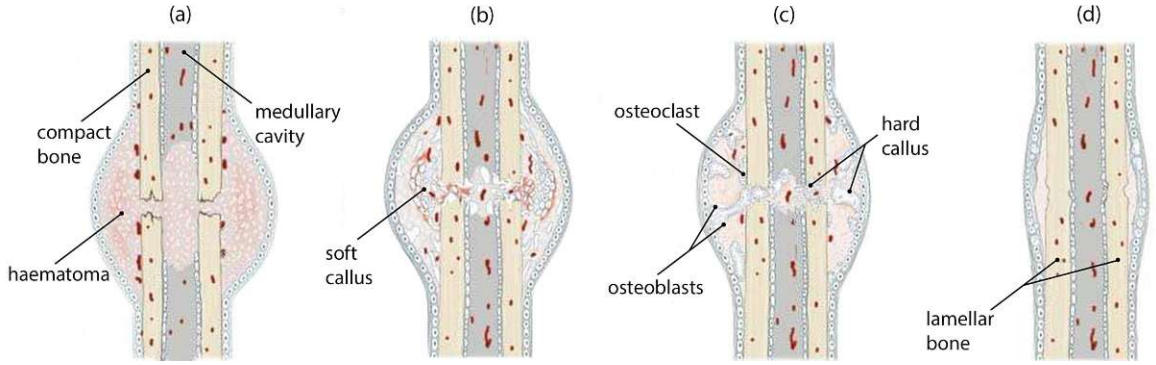

Figure 11: (a) Initial inflammation and hematoma formation at the fracture site corresponding to stage 1) in the text. (b) Soft callus formation. The soft callus bridges the fracture gap. (c) Hard callus formation. Ca is deposited within the soft callus, which develops into a hard callus. (b) and (c) correspond to stage 3) in the text. (d) Remodeling phase. Osteoclasts and osteoblasts remodel the immature woven bone into mature and lamellar bone, aligning with stage 4) in the text. The remodeling phase reestablishes the anatomy and physiology of the bone to its pre-fractured state. Adapted from [58].

The stages closely resemble the conventional fracture healing process upon implantation, with tissue gradually enveloping the implant. The insertion of an implant might, later on, alter stress distribution within the bone, potentially leading to unbalanced osteoblastic and osteoclastic activity. Consequently, a critical aspect in terms of implants is that they should not impede the natural physiology of the bone healing process [61].

2.1.6 The Mineralization Process

Following the secretion of osteoid, an unmineralized collagenous matrix (Figure 12, top) by osteoblasts, bone gets mineralized. In this mineralization process, Ca and P are taken up and form HAp crystals, successively increasing hardness. At the nanoscale, mineralization starts with a nucleation phase in the gap zones (Figure 12, middle), followed by a growth phase where the crystals extend in the overlap zones of the collagen (Figure 12, bottom).

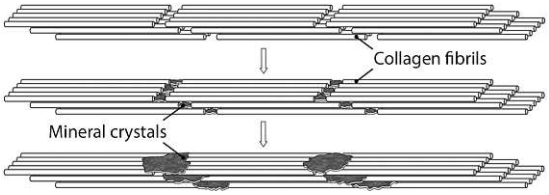

Figure 12: Mineralized collagen fibrils. Top: Staggered collagen molecules. Middle: The mineralization process initiates in the gap zones. Bottom: Crystals grow and extend into the overlap zones of collagen. Adapted from [62].

The mineralization law describes the kinetics behind the process in two steps, known as the primary and secondary stages of mineralization. It has been reported that during the first phase, up to 70 % of the final mineral content of bone is deposited within a few days, followed by the second stage characterized by slow and gradual mineral maturation (Figure 13) [63]. Continuous bone remodeling leads to a nonuniform degree of mineral concentration.

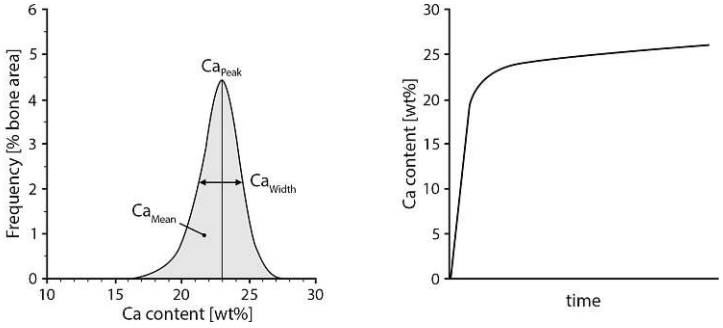

Figure 13: Left: Typical bone mineralization density distribution histogram of a healthy bone. Characterizing parameters: Ca_{Peak}, the most frequent Ca concentration; Ca_{Width}, the full-width at half maximum of the peak (indicating heterogeneity of mineralization); Ca_{Mean}, mean Ca concentration. Right: The mineralization law describes the changes in mineral concentration as a function of time. Adapted from [63, 64].

2.1.7 Bone Characteristics

The following section provides an overview of some essential properties. The structural features and mechanical properties of cortical bone are presented in Table 2. It has to be noted that the mechanical properties depend considerably on various factors, including the test direction (transverse or longitudinal), bone sample age, anatomical location, specific regions within the bone (such as osteonal or interstitial lamellae), gender, health condition, testing environment, and the testing method [44, 65–67].

Table 2: Mechanical and structural properties of cortical bone. Adapted from [8]. These values vary depending on different factors such as species, tissue type, and humidity (wet/dry).

	Cortical bone
Young's modulus [GPa]	7 – 30
Hardness [GPa]	0.62[a] – 0.79[b]
Strength [MPa]	100 – 230
Porosity [%]	5 – 10
Mass density [g/cm^3]	1.6 – 2.0
Total skeletal mass [%]	80

[a] [68], [b] [69]

2.1.8 Differences between Species

Animal bone is of great interest to the research community due to its higher accessibility compared to human bone. Animal studies are widely used to evaluate drug efficacy [22, 70, 71], assess changes caused by osteoporosis [72–75], and to investigate the influence of implants on tissue properties [76–78]. It is important to notice that there exist several limitations due to the structural differences between rat and human bone at the microscale. Human compact bone comprises Haversian systems and Volkmann's canals. In contrast, rats lack Haversian systems, and their bone remodeling process appears less organized than in humans [79]. This inter-species distinction must be considered when interpreting measurement results. Nevertheless, the mechanical values are of the same order of magnitude. Table 3 compares values for mature cortical human and rat bone assessed by nanoindentation using the Oliver-Pharr method (OPM).

Table 3: Properties of mature cortical bone in humans and rats assessed by nanoindentation using the Oliver-Pharr method.

Species	Anatomical site	Mass density [g/cm^3]	Young's modulus [GPa]	Hardness [GPa]
Human	Femur	1.6 – 2.0[a]	19.9 – 26.6[b]	0.60 – 0.84[b]
			18.8_{OL} - 20.8_{OL}[d]	0.55_{OL} - 0.65_{OL}[d]
			26.1_{INTL}	0.80_{INTL}
Rat	Femur	2.0[c]	19.9[b]	0.80[b]

[a] [8], [b] [44], [c] [80], [d] [81]; OL, osteonal lamella; INTL, interstitial lamella.

2.2 Osteosynthesis Material

Osteosynthesis describes an operative technique in orthopedic surgery wherein implants are employed to stabilize and fix fragments of a fractured bone. The goal is to provide temporary support that allows early functional rehabilitation while ensuring healing in an appropriate anatomical position [55]. Depending on various factors such as fracture localization, fracture type, and associated injuries, specific devices like plates, screws, wires, intramedullary nails, and other mechanical devices are used. To ensure meaningful incorporation of an implant into the body, it must adhere to an increasing set of safety requirements [82].

The choice of appropriate materials for osteosynthesis plays a significant role in the outcome and complication rate after the treatment of fractures. Beyond implant stability, other limiting factors exist. An ideal bone-contacting material should be non-toxic, non-allergenic, and should not induce adverse effects on the surrounding connective tissue. Essential prerequisites include good mechanical properties (elasticity modulus, tensile and compressive strength, coefficient of friction, wear resistance), chemical compatibility (chemical composition, corrosion resistance, solubility behavior, influence of pH level), as well as biocompatibility (cell adhesion, toxicity, carcinogenicity, tissue induction, antigenicity) [5, 83, 84]. Due to possible long-term side effects of remaining implants – such as inflammations, discomfort, pain, growth disturbances (especially in pediatric fracture treatment), and bone resorption – implant removal is usually performed after one year [82]. Thus, a second surgery has to be conducted, associated with the risk of further complications and extra healthcare costs [85,86]. Especially in orthopedics, bioresorbable implants offer an exciting alternative to overcome these issues.

2.2.1 Classical Biocompatible Implant Material

Biocompatibility is the ability of an implant material to perform its desired function *in vivo* without causing any harmful local or systematic reactions in the body [83]. Despite the enormous number of available materials in the industry, only a few meet the requirements for development as bio-implants. Conventional non-resorbable metallic implants, including stainless steel, pure titanium, titanium-based alloys, cobalt-based, zirconium-based, and tantalum-based alloys, are the most widely used biomedical implant metals. They played an essential role as osteosynthesis material, mainly regarding load-bearing

applications for repairing damaged bone tissue [4,87–89]. The selection of a specific material to be implanted depends on its medical application. Besides metals, other materials such as polymers, ceramics, bioactive glasses, bone cement, and artificial bone substitutes find applications as alternatives to these non-degradable metallic implants [84, 89]. Generally, the good tensile and compressive properties, mechanical strength, and fracture toughness make metals and their alloys superior to ceramics and polymers, especially in load-bearing situations [89]. Classical biomedical metals cannot degrade *in vivo* and persist in the body after implantation. Disadvantages encompass an elevated risk of localized inflammation due to corrosion debris [90, 91] or the release of toxic elements into the surrounding environment [92, 93]. To avoid these potential hazards, implant removal after the tissue has healed becomes necessary. Another drawback of these classic non-degradable metals is their mismatch in mechanical properties to natural tissues. Bones need mechanical stress produced by everyday movements to become ossified, retain their strength, and regenerate. Metallic implants are notably stiffer, with a Young's modulus of about 100–200 GPa as opposed to 10–30 GPa for the human bone [89, 94]. This difference can cause stress shielding, where the stiffer implant mechanically shields the bone tissue from loading stresses. This effect can cause bone atrophy and osteolysis [95–97], resulting in altered bone morphology [98] and a general delay in the healing process [95].

2.2.2 Biodegradable Implants

Biodegradation refers to the capability of complete degradation. As the full functionality of an implant is generally required only until the lesion has healed, biodegradable materials are an appropriate alternative. Degradable implant materials offer significant advantages over permanent implants.

In orthopedics and trauma surgery, the optimal implant for fracture treatment should be degradable and remain within the body only for a restricted duration – as long as the bone heals – which implies that no additional operation is required [55].

Implants must ensure an adequate fixation and temporary support of diseased or damaged bone tissue until sufficient new bone is formed [89, 99]. In contrast to static implants, the interplay of degradation and simultaneous healing shifts the bone-implant interface and continuous alterations in load distribution. The gradual decline in the implant's mechanical properties during degradation, coupled with increased loading on the

bone tissue, stimulates the healing process and makes it more dynamic, as illustrated in Figure 14 [100]. The ideal implant should degrade uniformly without any residues. It is essential that neither the implant materials nor the degradation products adversely affect the healing process [99].

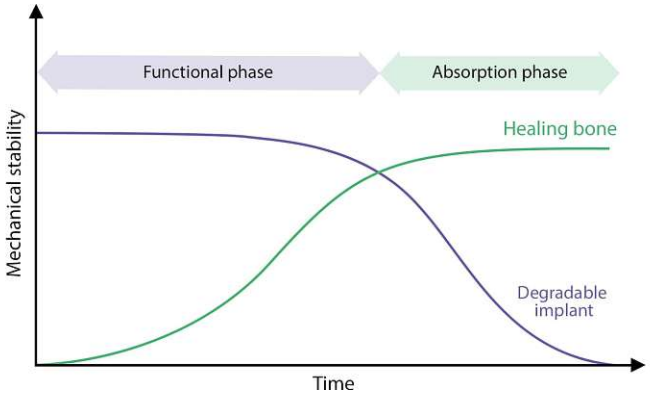

Figure 14: Illustration of the optimal balance between mechanical stability and degradation of the resorbable implant. The implant maintains strong mechanical stability throughout the functional phase to sufficiently support the bone. Whereas during the absorption phase, the implant's stiffness diminishes. This gradual load transfer from the implant to the tissue encourages the healing process, allowing the affected tissue to regain its stiffness as the bone heals. Adapted from [101].

As mentioned before, a major advantage of biodegradable implants is their ability to dissolve harmlessly, eliminating the need for a second surgery. In pediatric surgery, degradable implants are recommended because the growing body necessitates adjustments that permanent implants cannot accomplish [100]. Materials that closely mimic the mechanical properties of natural bone tissue are of particular interest. The following section will focus on the different types of biodegradable materials, including their advantages and disadvantages as implants.

Polymers

The most commonly used biodegradable polymers used in fracture treatment are poly-L-lactic acid (PLLA), poly-lactic-co-glycolic acid (PLGA), or poly-DL-lactic (PDLLA). Polymer-based materials exhibit a slow degradation rate, which can cause chronic inflammations. Their brittleness and the low Young's modulus restrict the usage of polymers to non-load-bearing regions or soft tissue reconstruction, making them unsuitable for all types of fractures [102, 103].

Composites

For instance, bioactive glasses are biocompatible and enable optimal bone growth on the

implant surface. The major drawback is their weak biomechanical properties. They are usually brittle, possess low strength, and cannot be used in load-bearing regions [102].

Ceramics

Ceramics, together with polymers and composites, are among the synthetic bone replacement materials. Bioceramics are composed of HAp, or α- and β-tricalcium phosphates (TCPs). Besides their high compressibility and biocompatibility, they exhibit good osteoconductivity, osseointegration, and non-immunogenic characteristics. However, biodegradable ceramics exhibit a low tensile strength, limited ability to deform, high brittleness, and relatively low crack-resistance properties. Their application is also limited to non-load-bearing regions [102, 104]. Moreover, HAp-based ceramics degrade far too slowly and cannot be sufficiently used as bioresorbable implants [105].

Metals

Polymers, composites, and bioceramics have significant disadvantages arising from issues related to their tissue interaction, resorption behavior, or inadequate mechanical properties. In contrast, metals are generally more suitable for load-bearing applications due to their combination of high mechanical strength and fracture toughness. Biodegradable metals such as iron (Fe) have shown promising properties in *in vivo* studies, such as high strength and ductility. According to Kraus et al., they do not provoke any local or systemic toxic and inflammatory reactions. However, their degradation rate is relatively low, thus, the application as a temporary implant is questionable. Similarly, zinc (Zn)-based alloys are also non-toxic, but their usage as biodegradable implant material is hindered by the low rigidity and deformability [102, 106].

In general, metals exhibit a slow degradation rate [102, 107, 108] and can cause stress-shielding due to the disparities in Young's modulus, subsequently affecting bone tissue degradation. Therefore, materials that provide adequate mechanical stabilization, properties close to natural bone tissue, as well as a homogeneous and moderate degradation rate are of interest [92, 109]. Particularly, Mg and its alloys are promising biodegradable materials due to their properties. According to Kammer [110], no other implant material has a Young's modulus that is as close to that of cortical bone. Additionally, Mg demonstrates good biocompatibility. The capability of Mg-based implants to support

bone fracture healing has been demonstrated, confirming their potential as an auspicious implant material [111].

2.3 Magnesium-Based Implants

Mg is one of the most promising materials for biodegradable implants with appropriate biomechanical parameters and excellent biocompatibility. Despite its first practical use as an implant reported by Lambotte already in 1907, Mg implants are still the subject of current research [112,113]. Mg and its alloys have attracted great attention as degradable biomaterials due to their mechanical and bio-corrosive properties. It is a lightweight material, showing several favorable characteristics. Mg is osteoinductive, thereby supporting the healing process [114]. The elastic modulus, yield strength, and ductility align more closely with those of bone when compared to conventional implant materials (Figure 15). Additionally, the density of approximately 1.74–2.0 g/cm^3 is similar to the bone density of 1.8–2.1 g/cm^3 (Table 4) [92, 115, 116]. The slight difference in Young's modulus between Mg alloys (41–45 GPa) [92, 116, 117] (pure Mg $\approx$ 37 GPa [118]) and cortical bone (5–23 GPa) [119–121], prevents the stress-shielding effect [92, 100].

Table 4: A comparison of the mechanical properties between Mg and natural bone [122].

Properties	Magnesium	Natural bone
Density [g/cm^3]	1.74 – 2.0	1.7 – 2.0
Young's modulus [GPa]	41 – 45	3 – 30
Tensile strength [MPa]	170 – 270	80 – 150
Compressive yield strength [MPa]	65 – 100	130 – 180

From a physiological perspective, Mg is well-suitable as a biodegradable implant material. It is an essential element and the fourth most abundant cation (Mg^{2+}) [123, 124], with approximately 20–28 g in a healthy adult human body [125, 126]. About half of the total amount is stored within the skeleton and positively influences bone strength [127]. Less than one percent is found in the blood [128]. The remaining portion is bound in the muscles and soft tissue. It plays a major role in membrane stabilization, neuromuscular excitation, and central nervous system functions [129]. It acts as a cofactor in almost all enzymatic systems, stabilizes structures like DNA or RNA, and is involved in metabolic pathways [130]. Some studies suggest that the exposure of bone to a degrading Mg implant

might exert a positive impact on the biological process of bone growth and regeneration. This is attributed to locally high amounts of available Mg and stimulatory effects such as osteoblastic differentiation, which in turn promotes bone formation [76,131–133]. Mg ions may integrate into the apatite crystal lattice, enhancing cell adhesion and accelerating the growth of bone tissue [134–136].

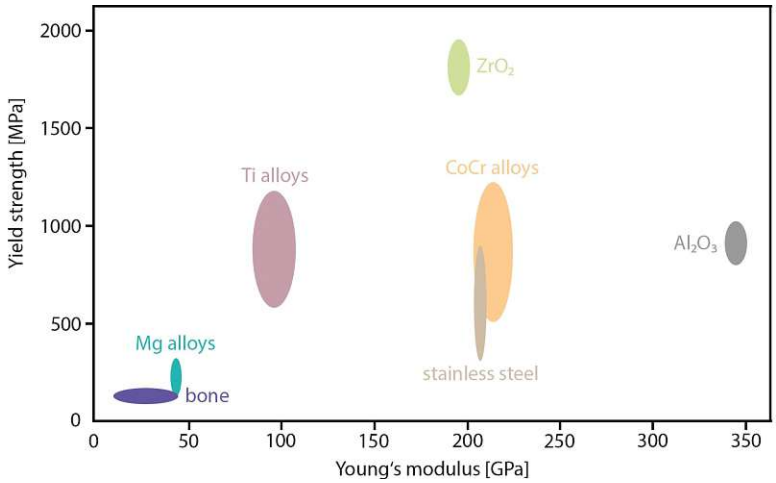

Figure 15: A comparison of the mechanical properties among different metallic materials reveals that the Young's modulus and yield strength of Mg closely resemble those of bone. Adapted from [102].

As mentioned, the usage of Mg as an implant material dates back to the early 20$^{\text{th}}$ century. Mg can be degraded *in vivo* by corrosion, thereby forming soluble and non-toxic corrosion products that can be excreted in the urine [137]. Biodegradable implants based on Mg are unlikely to cause hypermagnesemia – an excess of Mg – and allergic or toxic reactions [128, 138]. Furthermore, Mg is non-magnetic, available for roentgenoscopy, and exhibits good machinability [139, 140]. During degradation, the Mg implants release Mg^{2+} ions, which might positively contribute to bone formation. Furthermore, osteoclastogenesis-inhibiting properties were shown in the adjacent areas of an Mg implant, meaning that the formation and the activity of bone-resorbing cells are lowered [141]. Based on all the aforementioned properties, Mg alloys have increasingly attracted scientific research attention in recent years.

2.3.1 Corrosion of Magnesium

According to DIN EN ISO 8004, the term corrosion is defined as the physicochemical interaction between a metal and its environment, which leads to a change in the properties of the material and can lead to a considerable impairment of its function, the environment, or the technical system [142].

Even though degradation is disadvantageous in many engineering applications, this major drawback can be regarded as an advantage in clinical applications and makes the usage of resorbable implants feasible. The mechanism of the corrosion of the orthopedic biomaterial is a complex multifactorial phenomenon depending on various parameters like geometry, mechanical and chemical influences, as well as their interactions.

Despite the highly advantageous properties of Mg alloys as implants, their major drawback is the enormously high corrosion rate. Pure Mg is one of the most electronegative engineering materials, possessing a low standard potential of -2.37 V [116,143]. Therefore, it is highly susceptible to corrosion in various environments, including the physiological conditions within the body [144]. An excessively high corrosion rate results in premature loss of mechanical stabilization of the implant before the injured bone can sufficiently heal. Due to the redox reaction, hydrogen gas is generated near the implant, potentially causing inflammation and delaying the healing process [122]. To meet the requirement of a medical implant, corrosion resistance has to be enhanced by adding alloying elements to slow down the degradation rate and increase implant stability.

Corrosion Reaction

The corrosion process of Mg is an electrochemical process, different in air than in aqueous environments. In Figure 16 the existing theoretical regions are illustrated: passivation ($Mg(OH)_2$), corrosion (Mg^{2+}), and immunity (Mg).

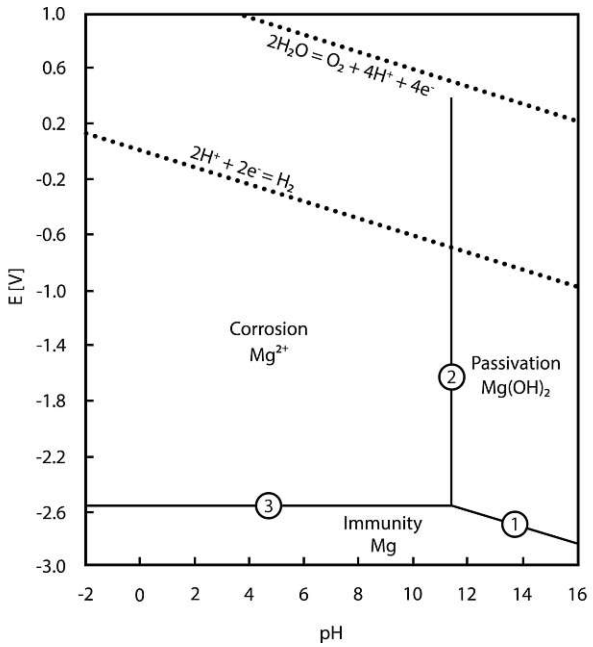

Figure 16: Pourbaix (potential (E)-pH) diagram for the system of pure Mg and water at 25 °C, showing the theoretical regions of corrosion, passivation, and immunity. Adapted from [145].

According to this Pourbaix diagram [145], it can be seen that the stability area of Mg lies below that of water. In an aqueous environment, Mg enters the solution as Mg^{+} and Mg^{2+} with simultaneous hydrogen evolution. Below the phase boundary line ③ Mg remains stable. To the right of line ② and above ① $Mg(OH)_2$ is stable. When exposed to air, Mg reacts with oxygen, forming a thin, gray, and stable Mg oxide (MgO) layer on its surface, preventing it from further atmospheric corrosion (Equation (1)).

$$2Mg + O_2 \rightarrow 2MgO \tag{1}$$

In the presence of moisture, this layer is transformed into magnesium hydroxide $Mg(OH)_2$, which is thermodynamically more stable. The third region, above ③ and to the left of line ② corresponds to the pH region, where corrosion occurs [145].
The reactions in most aqueous environments, including the physiological environment, proceed electrochemically to the following. The anodically initiated Mg dissolution takes place according to Equation (2). This counterbalances the cathodic reaction, wherein the hydrogen gas develops (Equation (3)). The product formation of $Mg(OH)_2$ proceeds electrochemically accordingly to Equation (4).

$$Mg \rightarrow Mg^{2+} + 2e^{-} \tag{2}$$

$$2H_2O + 2e^{-} \rightarrow H_2 + 2OH^{-} \tag{3}$$

$$Mg^{2+} + 2OH^{-} \rightarrow Mg(OH)_2 \tag{4}$$

The corrosion reaction of Mg in aqueous environments is given below:

$$Mg_{(s)} + 2H_2O_{(aq)} \rightarrow Mg(OH)_{2(s)} + H_{2(g)} \tag{5}$$

$Mg(OH)_2$ forms a protective layer around the implant while hydrogen gas (H_2) is produced (Equation (5)). It is indicated that one mole of hydrogen gas is generated for one mole of Mg dissolved. In other words, the degradation of one gram of pure Mg yields approximately one liter of hydrogen gas. In sufficiently alkaline solutions ($pH > 11.5$), the implant is covered with a protective hydroxide layer, effectively shielding the metal from rapid degradation [146]. As the pH value decreases, the surface layer becomes thinner and more fragile, providing only limited protection and generally accelerating the corrosion of

Mg [145]. At a pH value of approximately 7.4, such as in *in vivo* conditions, this hydroxide layer is neither stable nor complete and will continuously be dissolved [147]. Further, permanent corrosion protection cannot be ensured as the hydroxide layer is prone to chloride ions (Cl^-). These ions quickly convert the layer into highly soluble magnesium chloride ($MgCl_2$) if the chloride concentration in the surrounding medium exceeds 30 mmol/l. As the chloride content within the body fluid is about 150 mmol/l, accelerated corrosion on the Mg implant can be observed according to Equation (6) [119, 144]:

$$Mg(OH)_2 + 2Cl^- \rightarrow MgCl_2 + 2OH^- \tag{6}$$

This product is soluble and thus can be transported or degraded by macrophages [102,119].

2.3.1.1 Hydrogen Gas Formation

The process of Mg degradation is accompanied by the undesirable hydrogen gas evolution following Equation (5), which can pose challenges in biomedical applications. Once the local hydrogen saturation of blood and tissue is reached, diffusion and solubility of hydrogen in surrounding tissues become hindered. In this way, hydrogen gas accumulates, creating gas bubbles subcutaneously and in the tissue around the implantation site. This may cause the separation of tissue layers [119, 144]. The effect of gas formation depends on its spatial expansion and temporal existence [148]. Higher corrosion rates result in increased gas formation. Song postulated that a slow hydrogen evolution rate of 0.01 ml/cm^2/day could be tolerated by the body painlessly without causing serious harm if the gas can be transported away from the site of its generation. Hence, local gas accumulation can be prevented [149]. However, excessive hydrogen gas formation creates pressure, inducing some disturbances and potentially leading to an embrittlement of the implant. Further, it can interfere with the bone healing process, resulting in cortical defects, excessive callus formation, and other issues since gas pockets harm the surrounding tissue [150, 151]. Via the bloodstream, the gas can accumulate in organs and exert harmful effects, especially in organs like the brain and lungs. If the pockets are large and gas simultaneously enters the blood circulation, they may lead to a patient's death by blocking the bloodstream [129]. Therefore, it is essential to adjust the corrosion rate and, consequently, the rate of gas formation through appropriate alloying elements.

2.3.1.2 Influences on the Degradation Rate

Corrosion within the aqueous environment of the body is highly complex. Controlling the degradation rate is challenging and plays a fundamental role in bone formation. The actual corrosion rate in the body varies depending on several factors, like the pH of body fluids, the concentration and types of ions present, the presence of proteins, temperature, impurities in the metal, alloying elements, and the surrounding tissue as could be shown in several *in vitro* and *in vivo* investigations [150, 152–158].

Other factors, including the species under study, the implantation site, thus the corresponding flow and composition of body fluids, the type of implant (screw, plate, nail), material purity, and alloying elements, all contribute significantly to the degradation behavior [159].

2.3.2 Alloying Elements

Developing Mg alloys with different alloying elements is aimed at adjusting material properties. Appropriate element alloying is an effective method to significantly improve and adapt mechanical, physical, and electrochemical properties, like enhancing yield strength and ductility. Based on the high corrosion rate of Mg, the alloying element should be able to improve its corrosion resistance [149]. Pure Mg is relatively weak and is almost exclusively used as an alloy for engineering and medical applications. Its hexagonal close-packed crystal structure contributes to its limited ductility [115, 116]. In terms of biomedical products, the choice of alloying elements is somewhat limited as the resulting by-products should exert minimal effects on the body, must be non-toxic, and be capable of either being absorbed by surrounding tissues or dissolved and excreted naturally [160, 161]. The following section will only discuss specific elements present in the alloy under investigation and their respective influences.

2.3.2.1 Calcium

Ca is a promising alloying element for biodegradable Mg alloys due to its biocompatibility arising from its natural occurrence within the human metabolism. It positively influences bone health and can help to accelerate growth and healing [162, 163]. It has been reported that Ca enhances both the mechanical properties and the corrosion resistance of Mg-based alloys [94, 164]. The addition of Ca to a Mg alloy results in grain refinement [164, 165],

which is an effective method to enhance the strength by grain boundary hardening, described by the Hall-Patch relationship [166, 167]. Another notable advantage of Ca is its influence on elevated ductility [163, 168]. Previous studies have demonstrated that the mechanical properties and corrosion resistance are relatively low in Mg-Ca binary alloys [169, 170]. Thus, adding another alloying element, like Zn, becomes necessary to overcome these drawbacks and optimize the alloys for their application in biodegradable implants.

2.3.2.2 Zinc

The yield strength of Mg alloys can be enhanced by adding Zn due to grain refinement [119,144,171]. One advantageous aspect of Zn as an alloying element is its potential to decrease the amount of hydrogen gas evolution resulting from Mg corrosion [161, 172]. Zn has been observed to enhance osteoblastic cell proliferation and positively influence bone healing when used as an alloying element in Mg-based biomaterials. Generally, Zn enhances the corrosion resistance of Mg alloys, but the effect varies based on the specific alloy composition [163]. Cihova et al. conducted experiments with two ZX-alloys, Mg-1.5Zn-0.25Ca (in wt%; ZX20) and Mg-1.0Zn-0.3Ca (in wt%; ZX10), showing that even a minor change of 0.5 wt% Zn lead to a reduction in the degradation rate [102, 173].

2.3.2.3 Previous Alloys based on Magnesium

Numerous studies investigated Mg-based alloys and reported their advantages and disadvantages, with a primary focus on addressing the challenge of enhancing the relatively low degradation resistance of pure Mg. Efforts to decelerate the degradation process have led to the investigation of alloys containing rare-earth elements like yttrium, which not only improve implant stability but also impact the degradation kinetics [174]. Rare-earth elements are not part of the human body and have been described as mildly toxic. Some studies have revealed the persistence of alloying element precipitates years after implantation, yet the potential adverse effects of rare-earth elements on the developing skeleton remain largely unexplored [174]. However, the aim was the development of a resorbable metallic implant based on elements occurring naturally within the body. Therefore, different compositions of Mg-Zn-Ca, denominated as ZX-alloys, were investigated. The Mg-Zn-Ca alloying systems exhibit an attractive combination of good biocompatibility,

adequate strength, and simultaneously appropriate ductility [175]. The Mg-alloy ZX50 exhibited excessive degradation and thus cannot be used as an orthopedic implant [150,174]. Consequently, Zn was gradually reduced (ZX20 and ZX10). Studies demonstrate a significantly slower degradation rate and a decreased hydrogen gas evolution [173]. Finally, a Mg-based implant (ZX00), especially for the stabilization of bone fractures in children and adolescents, was developed and will be investigated in this thesis [102].

2.3.2.4 Mg-Zn-Ca Alloy (ZX00)

This study focuses on the investigation of a Mg-0.45Zn-0.45Ca (in wt%, ZX00) alloy. It exhibits an ultimate tensile strength of about 285.7 MPa and an elongation at fracture of 18.2 % [175]. Theoretically, the organism could safely metabolize the implanted alloy since these three alloying elements are naturally occurring within the human bone. The corrosion behavior of this low-alloyed material is characterized by a slow and controlled homogenous degradation. Furthermore, ZX00 implants showed excellent biocompatibility, osteoconductivity, and established a robust implant-bone interface [102, 175].

2.4 Scanning Electron Microscopy

Scanning electron microscopy (SEM) is an imaging technique utilized for material characterization, offering a spatial resolution in the nanometer range [176]. The major components of an SEM include the electron column, a sample stage, a detector, and a control console. The electron beam column, in turn, is composed of an electron gun that generates the electrons, the anode, several electron lenses, and the deflector coils. The electrons emitted by the cathode are attracted by the anode. The magnetic lens system guides the electron beam down the evacuated tube to the specimen chamber, demagnifies the beam's spot size, and focuses it [177]. Within the sample chamber, the sample stage and electron detector are positioned. The narrow-focused, primary electron beam sweeps across the sample and scans the surface of interest by pushing the beam back and forth using deflector coils. Interactions between incident electrons and the specimen lead to an emission of secondary electrons (SE), backscattered electrons (BSE), auger electrons, photons, X-rays, and heat (Figure 17) [178].

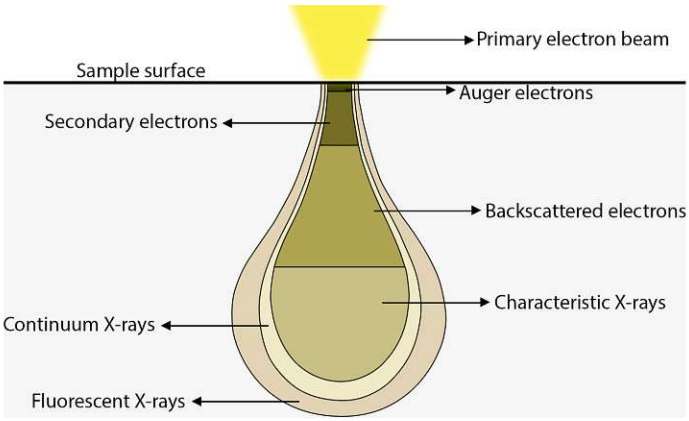

Figure 17: Electron interaction volume within a sample and the different types of signals produced: Backscattered electrons (BSE), secondary electrons (SE), characteristic X-ray radiation, continuum X-ray, Auger electrons, and fluorescence are generated after the impingement of the primary electron beam at different depths within the sample. These signals can be collected and analyzed to provide information about the morphology, microstructure, and composition.

The electron interaction volume and penetration depth of the primary electrons depend on the energy of the incident beam and the atomic weight of the specimen. In this study, mainly BSEs were used to investigate the samples. They are high-energy electrons of the primary beam that are deflected back due to elastic scattering. BSE images are widely used because of their atomic number (Z) contrast. Heavier elements with a higher Z efficiently backscatter electrons, rendering them brighter in the acquired image compared to lighter elements with lower Z, which appear darker. This BSE Z-contrast enables the distinction of different regions on the sample surface. In contrast, SEs are inelastic scattered low-energy electrons. They typically originate from within a few nanometers of the sample surface. Due to the distinct energy levels, they are collected by various detectors and are translated into a signal, generating an image that provides insights into surface topography and composition [177,179]. Energy-dispersive X-ray (EDX) detectors are able to collect the emitted characteristic X-rays and thus allow the elemental composition of the specimen.

Bone Imaging

Bone tissue exhibits a heterogeneous distribution of mineralization, a consequence of the ongoing remodeling process. The use of the BSE operating mode allows for the discrimination of areas with varying levels of mineralization, as revealed by the BSE Z-contrast (Figure 18).

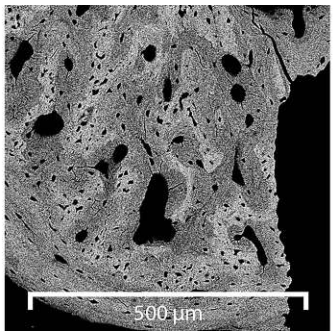

Figure 18: Bone exhibits a heterogeneous mineral distribution. SEM-BSE imaging of bone shows distinct shades of gray, depending on their mineralization degree and localized variation in Ca content.

2.5 Nanoindentation

The origin of nanoindentation, also known as instrumented indentation testing, goes back to Moh's Hardness scale [180] and is derived from the classical hardness concept based on scratching. In the late 19th century, Martens implemented an instrumented indentation measurement technique that recorded force-indentation depth curves [181]. However, the groundbreaking work of Oliver and Pharr in 1992 [182] established nanoindentation as a versatile and powerful tool to evaluate mechanical properties. Since then, the capability of this tool has made a remarkable evolution. Nowadays, nanoindentation is one of the leading techniques for quantitative characterization, providing the opportunity to extract mechanical properties, such as the elastic modulus and hardness of the specimen material on the micro- or nanoscale [65,182–185]. Nanoindentation allows for determining material properties of bone at the tissue scale without being affected by the bone's size, shape, or porosity, as would be the case in whole bone mechanical testing [186]. Additionally, it eliminates the need for optical measurements of the residual plastic imprint of the indent, as it is done with classical methods for hardness measurement [180, 187]. Many studies have demonstrated the use of nanoindentation and applied it to bone analysis, revealing its potential for assessing disease-related changes in tissue properties [183, 188], capturing regional variations in tissue properties [68,81], and correlating tissue mechanical properties with mineral content [189, 190].

2.5.1 Conventional Nanoindentation Testing

Due to the miniaturization, the optical measurement of the projected contact area of the remaining impression is in the order of microns and is still too small to be measured directly [180]. Instead, the projected contact area is computed from indentation depth.

A conventional nanoindentation experiment involves applying a prescribed load to an indenter with well-known properties, which is in contact with the specimen of interest whose mechanical properties are unknown. The force and depth of penetration at the tip are simultaneously and continuously recorded during the loading and unloading phases. From the corresponding load-displacement curve, the hardness (H) and Young's modulus (E) of the specimen material can be extracted. This is done without directly observing the residual impression under a microscope, following the analytical approach introduced by Oliver and Pharr [182]. The fundamentals of this method are briefly outlined in the following section. For further details, the reader is referred to [180, 182, 191]. An indenter profile is shown in Figure 19, along with a schematic representation of a typical force-displacement graph from the nanoindentation experiment, illustrating the various parameters extracted for analysis.

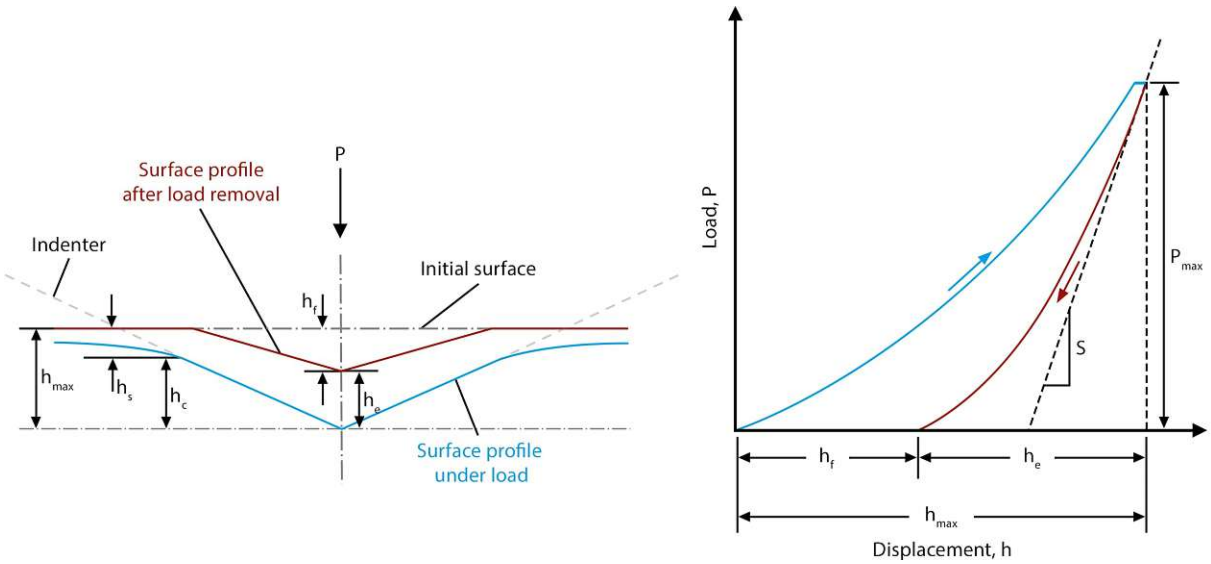

Figure 19: Nanoindentation analysis according to the method outlined by Oliver and Pharr [182]: Left: Schematic view of the surface profile under full load (blue) and after load removal (red). Right: Load-displacement curve: Load vs. displacement for elastic-plastic loading (blue) followed by elastic unloading (red). Key parameters include the maximum load P_{max} and the corresponding maximum penetration depth h_{max}; h_f denoting the depth of the residual (=final) impression, h_s representing the depth from the edge of the contact at P_{max} to the initial specimen surface, h_e indicating the elastic displacement during unloading, and h_c denoting the contact depth. S signifies the slope of the unloading curve dP/dh at h_{max} for calculating the specimen's modulus and hardness.

To obtain a load-displacement curve, the displacement (h) and the load (P) are continuously monitored as the indenter is pushed into and withdrawn from a specimen. A trapezoidal load function (Figure 20) is applied to the indenter tip, characterized by a constant loading phase, a period of holding the peak load, and a constant unloading phase.

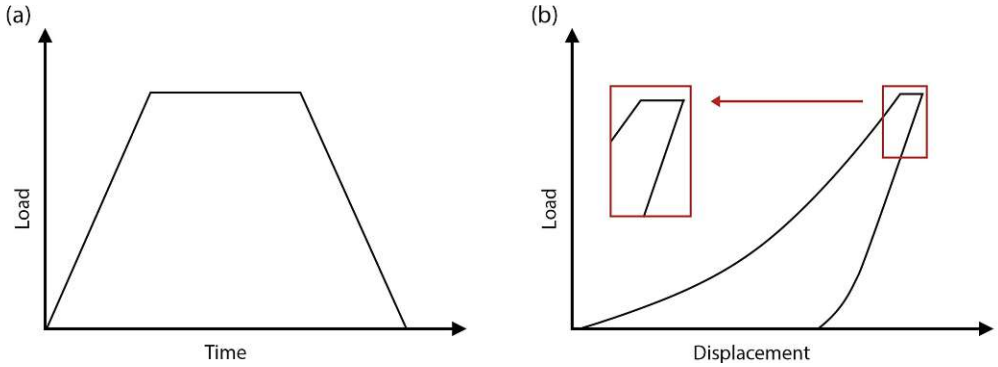

Figure 20: A typical trapezoid load-time curve (left) and the corresponding load-displacement curve (right). The holding period at the maximum load should minimize the impact of viscoelastic attributes. The trapezoidal testing profile is usually used for OP analysis on viscoelastic materials. [185].

This is done for two reasons. First, elastic properties cannot be measured from the loading curve since both elastic and plastic deformation in the material occurs. In contrast, it can be assumed that only the elastic deformation is recovered during unloading. Thus, the slope of the unloading curve can be directly related to the elastic stiffness of the material. Second, the creep holding period for a few seconds at maximum peak load should minimize the contribution of the viscoelastic behavior of viscoelastic materials such as bone [185, 186, 192–194].

During the loading process, the load steadily increases from zero to some predetermined maximum load P_{max} while the indenter penetrates the sample (force-controlled). At P_{max}, the corresponding penetration depth is referred to as h_{max}. Alternatively, it is possible to increase the displacement from zero to a predetermined maximum penetration depth while the related load is measured and referred to as P_{max} (displacement-controlled). The loading curve is represented by the region between ($h = 0$, $P = 0$) and (h_{max}, P_{max}) (Figure 19). This curve characterizes the plastic and elastic behavior of the material. The indenter is then retracted from the sample by steadily reducing the load until it returns to zero. While unloading, only the elastic deformation can be recovered. Consequently, the unloading curve, represented between (h_{max}, P_{max}) and (h_f, $P = 0$), enables conclusions concerning the material's elastic recovery. Based on plasticity, a residual penetration depth after entirely unloading (h_f) and a displacement (h_e) due to elastic recovery can be measured. Three quantities are required to further calculate H and E from a load-displacement curve, shown in Figure 19. These are P_{max}, the corresponding h_{max}, and the contact stiffness S as the slope (dP/dh) of the upper portion of the unloading curve

during its initial stage [195]. The amount of so-called sink-in (h_s) is given by:

$$h_s = \varepsilon \cdot \frac{P_{max}}{S} \tag{7}$$

with ε being a geometry factor of 0.75 for a standard Berkovich indenter (Equation (7)) [195]. As indicated in Figure 19, the depth h_c (Equation (8)) at which contact occurs between the sample and the indenter is:

$$h_c = h_{max} - h_s = h_{max} - \varepsilon \cdot \frac{P_{max}}{S} \tag{8}$$

The relationship between the projected area A_c of the indentation and the depth h_c (Equation (9)) beneath the contact is:

$$A_c(h_c) = 3\sqrt{3} \cdot h_c^2 \cdot tan^2\theta \tag{9}$$

where $\theta = 65.27°$, and thus

$$A_c(h_c) = 24.494 \cdot h_c^2 \approx 24.5 \cdot h_c^2 \tag{10}$$

for a perfect Berkovich tip (Equation (10)). The geometry of the indenter is known to affect the load-displacement response. Therefore, accurately defining the projected area is crucial to account for deviations from non-ideal indenter geometry. This ensures the correct determination of the unknown material properties. Given that a perfect indenter tip seems unrealistic, the actual area function (A_c) can be obtained from a calibration procedure on a reference material. Conventionally, fused quartz is used for that purpose. The OPM is based on the experimental finding that a power law relationship (Equation (11)) can approximate the unloading portion of indentation data:

$$P = \alpha \cdot (h - h_f)^m \tag{11}$$

where α and m are constants that depend on the indenter geometry.
The stiffness S (Equation (12)) is obtained from the slope (dP/dh) of the power-law fit of the initial part of the unloading curve derived from measurements with various peak loads.

$$S = \left.\frac{dP}{dh}\right|_{h_{max}} = m \cdot \alpha \cdot (h_{max} - h_f)^{m-1} \tag{12}$$

The reduced modulus, E_r (Equation (13)), which is a combined modulus of the sample material and the indenter, can be calculated with:

$$\frac{1}{E_r} = \frac{1-\nu_{cm}^2}{E_{cm}} + \frac{1-\nu_i^2}{E_i} \tag{13}$$

where E_{cm} and ν_{cm} are the elastic modulus and Poisson's ratio of the calibration material, and E_i and ν_i are the elastic modulus and Poisson's ratio of the indenter, respectively (Table 5). The actual projected contact area A_c (Equation (14)) can be calculated for different penetration depths with the obtained S (Equation (12)) and E_r (= 69.6 GPa) (Equation (13)) using:

$$A_c(h_c) = \frac{\pi}{4\beta} \cdot \left(\frac{S}{E_r}\right)^2 \tag{14}$$

The correction factor β is related to the geometry of the indenter, which for a Berkovich tip ranges from 1.023 to 1.085 [195].

It is common practice to fit a 5^{th} order polynomial to contact area-displacement data:

$$A_c(h_c) = a_0 h_c^2 + a_1 h_c + a_2 h_c^{\frac{1}{2}} + a_3 h_c^{\frac{1}{4}} + a_4 h_c^{\frac{1}{8}} + a_5 h_c^{\frac{1}{16}} \tag{15}$$

Where a_0 is a geometry factor depending on the opening angle of the indenter (24.5 for a perfect Berkovich tip) and a_i are fitting parameters used to describe the deviations of the indenter from the ideal shape (Equation (15)) [191]. This obtained function is then stored in the software and used for further measurements.

Ultimately, from the knowledge of $A_c(h_c)$, H, and E_r, which is now a combined modulus of the sample material with unknown properties and the indenter, can be calculated at the point of unloading (Equation (16) and (17)) following Oliver and Pharr:

$$H = \frac{P_{max}}{A_c(h_c)} \tag{16}$$

$$E_r = \frac{\sqrt{\pi}}{2\beta} \cdot \frac{S}{\sqrt{A_c(h_c)}} \tag{17}$$

E_r can finally be used to assess the indentation modulus E of the investigated sample

material (Equation (18) and (19) after transposition):

$$\frac{1}{E_r} = \frac{1-\nu^2}{E} + \frac{1-\nu_i^2}{E_i} \tag{18}$$

$$E = \frac{E_i \cdot E_r \cdot (1-\nu^2)}{E_i - E_r \cdot (1-\nu_i^2)} \tag{19}$$

where ν and E represent the Poisson's ratio and Young's modulus of the test material, and E_i and ν_i denote the elastic modulus and Poisson's ratio of the indenter, respectively. Suppose the sample material, such as bone ($\approx E < 30\,GPa$), is substantially less stiff than the tip material, the second part of Equation (18) can be ignored since this correction term has a negligible impact ($< 3\,\%$) on the calculated modulus [185]. Finally, E can be calculated according to Equations (20) and (21):

$$\frac{1}{E_r} = \frac{1-\nu^2}{E} \tag{20}$$

$$E = E_r \cdot (1-\nu^2) \tag{21}$$

Table 5: Values of Young's modulus and Poisson's ratio for both the diamond indenter tip and the calibration material.

	Fused quartz	Diamond
Young's modulus [GPa]	72	1140
Poisson's ratio	0.17	0.07

The validity and comparability of the obtained results strongly rely on the analysis method [180]. Ideally, the indentation modulus and the elastic modulus would be equal. However, the indentation modulus can be significantly affected by piling-up, a factor not considered in this analysis of the load-displacement data [195]. Limitations of nanoindentation and the analysis with OPM are, for instance, the accurate assessment of the contact area. Furthermore, OPM is based on several assumptions. It assumes that the behavior of the sample is elastic with time-independent plasticity without damage. It also assumes that the Poisson's ratio is known and the sample is an isotropic solid [67, 182]. However, bone is not purely elastic. Further, the Poisson's ratio for bone was found to

be direction and load-dependent. In cortical bone, the Poisson's ratio ranges from 0.15 and 0.45 but is usually set to 0.3 in most studies when calculating Young's modulus from the indentation load-displacement curve [196]. It was shown that the variations in the measured moduli remain within $\pm 10\,\%$ by varying the Poisson's ratio in the range of 0.2 to 0.4 [67]. Additionally, bone is a heterogeneous and anisotropic solid. In summary, bone does not meet all the assumptions required by the OPM. Thus, these quantitative values must be treated cautiously and cannot be directly compared with values from the literature. However, this is much less of an issue for comparative studies, which aim to point out differences among various groups with all samples prepared and tested equally.

2.5.2 Dynamic Nanoindentation Analysis

Static nanoindentation allows the determination of Young's modulus and hardness only at the initial point of unloading, yielding a single result for a given indentation depth (Figure 21, 1a and 2a). On the other hand, the dynamic method, known as continuous stiffness measurement (CSM), enables an increasing data output. Superimposing a small sinusoidal force signal onto the primary loading function (Figure 21, 1b) causes the indenter to oscillate with amplitude and a phase shift based on the material's stiffness. Measuring the resulting displacement amplitudes, as well as the phase shift, allows for assessing the contact stiffness (S) at any point along the loading curve (Figure 21, 2b) instead of determining the slope just at the point of unloading as in the conventional measurement [195, 197–199]. Consequently, hardness and Young's modulus can be continuously calculated over the displacement (Figure 21, 3b). Thus, a depth profile of mechanical properties can be achieved. Such measurements can be made even at minimal penetration depths, making it ideal for assessing the mechanical properties of extremely thin sample slices. A frequency of 45 Hz and displacement amplitude of 2 nm are often recommended [197, 200].

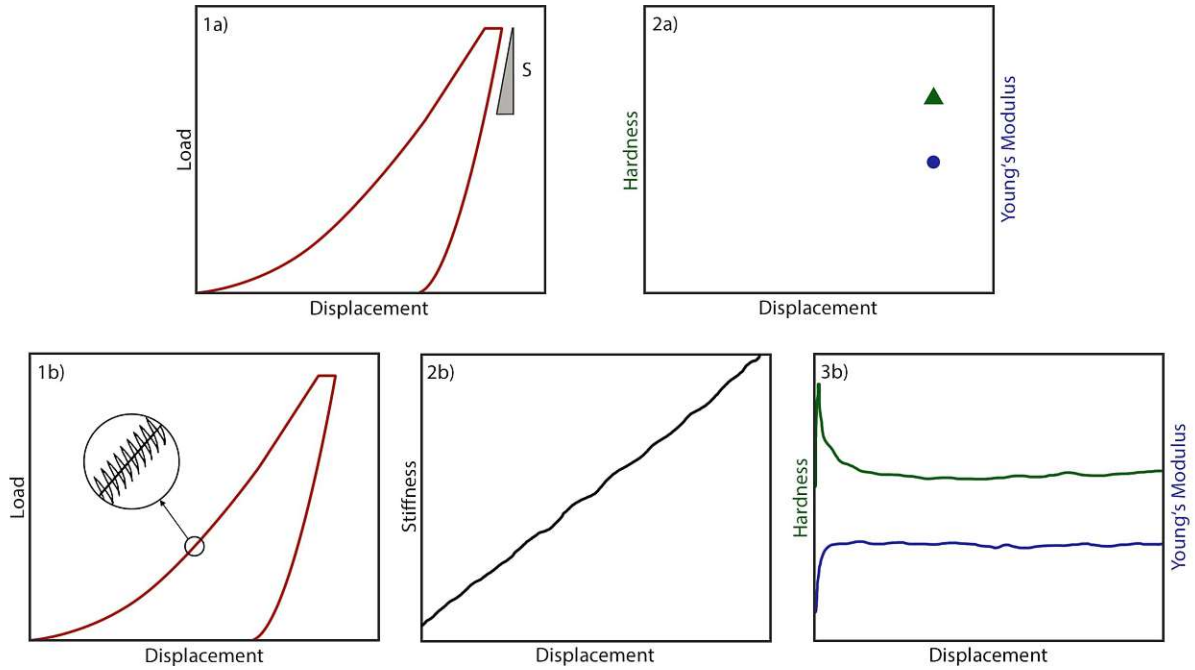

Figure 21: Static and dynamic testing modes. 1a) Schematic indentation load-displacement curve for static testing mode, with 2a) hardness and Young's modulus obtainable only at the unloading point. 1b) Schematic indentation load-displacement curve for dynamic testing mode, displaying the CSM signal with a small overlapping oscillation onto the basic loading signal. 2b) Continuously recorded stiffness over indentation depth. 3b) Continuously measured hardness and Young's modulus over displacement.

2.5.3 Indenter Tip

The results are influenced by both the geometry and hardness of the indenter tip, and these factors play a crucial role in accurately interpreting the indentation results. The choice of the indenter depends on the information one wishes to obtain, and it is necessary to specify the method used. Different tip geometries can be used for imprinting into the material surface. The indenter can usually be found as a 3- and 4-sided pyramid, such as Berkovich [201] and Vickers tips, as a cube-corner, conical or spherical tips [187, 202]. The selected indenter material should be hard and stiff, ensuring minimal influence on the measurement. This requirement reduces the choice of potential candidates, and there is only a small selection of materials like diamond, sapphire, or tungsten [203]. However, diamond is typically the material of choice for tips because of its high hardness and elastic modulus, remarkable thermal conductivity, and chemical inertness [187, 202].

The Berkovich indenter is characterized by a sharp three-sided pyramid with a face angle of 65.27° with respect to the vertical indentation axis [180,201]. It has a radius in the range of 100–150 nm [180,186]. Compared to other tip shapes, the sharp Berkovich tip maintains a self-similar geometry to small scales, ensuring precise control over the indentation process. This tip design is mainly used in measurements in the nanometer range [180, 201, 202].

3 Materials

This section gives an overview of the materials used in the present work.

3.1 Animals

The samples were kindly provided by Assoz. Prof.in Priv.-Doz.in Dr.in Weinberg and Priv.-Doz.in Dr.in Sommer from the Medical University of Graz. To achieve the utmost accuracy of results, animals of the same breed were chosen, minimizing discrepancies in weight and size. Therefore, four-week-old female Sprague Dawley® (SD) rats were purchased from Janvier Laboratories (Saint Berthevin, France). All individuals received the same care and treatment during the experiments. They were housed in conventional cages and maintained on a 12-hour light-dark cycle throughout the study, with access to water and standard pellet food ad libitum.

3.1.1 Ethical Statement

All animal experiments were performed at the Medical University of Graz under animal ethical respect. The Austrian Federal Ministry of Science and Research approved these small animal studies, complying with the guidelines on the accommodation and care of animals formulated by the European Convention for the Protection of Vertebrate Animals Used for Experimental and Other Scientific Purposes.

3.2 Implants

For this study, cylindrical pins with dimensions of 8 mm in length and 1.6 mm in diameter (Figure 22) were used. These implants are composed of an alloy called ZX00, solely based on materials occurring naturally in the bone. The alloy consists of ultra-high pure Mg (99.999 %), alloyed with Zn (99.9999 %) and Ca (99.9 %) in a nominal composition of 0.45 wt% Zn and 0.45 wt% Ca. The pins were utilized as bicortical implants. The reader is referred to a more detailed description of the implant fabrication [175].

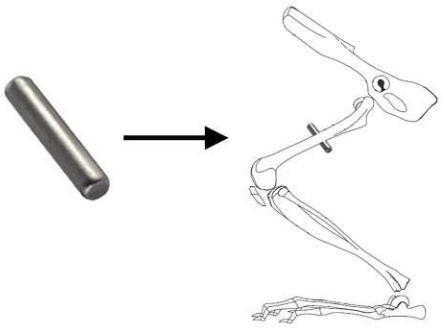

Figure 22: A cylindrical ZX00 pin was used as a bicortical implant. Adapted from [79].

4 Methods

In this section, the main focus lies on the sample preparation and the investigation methods.

4.1 Surgery – Bicortical Implantation

At six weeks of age, bicortical implantation of cylindrical ZX00 implants into the rat's diaphysis was performed. Volatile isoflurane was administered for general anesthesia, preceded by subcutaneous sedation. The leg was shaved and antisepticized with alcohol pads. A skin incision was made over the femur, followed by removing blood and connective tissue to expose the bone (Figure 23).

Figure 23: Pin implantation. Left: A skin incision was made over the femur. Right: Blood and connective tissue were removed. A retractor was used to gently separate the tissue, providing access to the bone. The bicortical implant is visible in the middle of the wound.

A bicortical hole with a diameter of approximately 1.55 mm was carefully drilled into the mid-diaphyseal region of the femur. Drilling was performed at a relatively low rotational speed to minimize frictional heat and the risk of thermal necrosis. The cylindrical implants were inserted into the prepared implantation bed by gentle tapping, resulting in a uniform press fit since the drill's diameter was smaller than that of the implant. The wound was closed with a self-absorbable suture, and all animals received an analgesic postoperatively. After the operation, the animals were allowed to move freely in their cages and bear weight without restriction.

4.1.1 Euthanasia

To be able to make a statement about the degradation behavior of the implants and any change in the mechanical properties in the area of the implanted pin over time,

samples with distinct implantation times were used. More precisely, the animals were randomly assigned to different euthanasia time points, namely 2, 6, 18, 24, and 52 weeks post-implantation. At these defined time points, the rats were euthanized. Therefore, isoflurane was administered, followed by direct injection of thiopental into the heart, resulting in cardiac arrest. The rat's femurs were extracted, freed from adhering soft tissue, and deep frozen at -80 °C. A summary of all samples and their corresponding euthanasia time points is provided in Table 6.

Table 6: Overview of the used samples. Euthanasia time points are given in weeks.

Euthanasia time points [weeks]	Sample identifier (ID)
2	2672
6	2642
	2644
18	2570
24	2642
	2466
52	2646

4.2 Sample Preparation

Before starting with nanoindentation measurements, the bone samples were prepared according to the following protocol. Figure 24 exemplifies the initial state of an extracted and deep-frozen femur, with the pin visible in the mid-diaphysis region.

Figure 24: Initial state of an extracted right femur. The implant is visible in the middle of the diaphysis.

Particular caution was required during sample preparation, especially for the 2-week sample, to prevent any movement of the implant as it had not yet been connected to the bone

tissue. The proximal and distal epiphysis of the femur were trimmed (Figure 25, left) using a precision saw, Accutom-50 (Struers GmbH, Germany), with a diamond cut-off wheel (MOD13, Struers GmbH, Germany) at low speed. All samples were fixed in ethanol for seven days to conserve the structure. Given that the water content of bones affects the mechanical properties significantly, all samples were dehydrated in ethanol for three more days. Next, removing the remaining lipids from the tissue was necessary to facilitate the penetration of embedding materials. The samples were defatted in a 1:1 mixture of ethanol and acetone for eight hours and inserted again into ethanol for six days. The subsequent steps included preinfiltration and infiltration, both for 24 hours in the refrigerator, necessary to replace the ethanol with a xylene mixture gradually. When the tissue is finally embedded in Technovit®9100 according to the manufacturer's protocol (Kulzer GmbH, Wehrheim, Germany), the molten embedding medium will replace the xylene [204]. This resin embedding system, based on methyl methacrylate (MMA), was specifically designed for mineralized tissues [205]. The components, such as poly methyl methacrylate (PMMA)-powder and a regulator, allowed controlled polymerization at low temperatures that guaranteed a complete dissipation of the polymerization heat. Special embedding molds (Kulzer GmbH, Wehrheim, Germany) were used to position the samples. The molds were filled with the prepared mixture and placed in a vacuum furnace to prevent air inclusions. Subsequently, the samples were stored in a refrigerator.

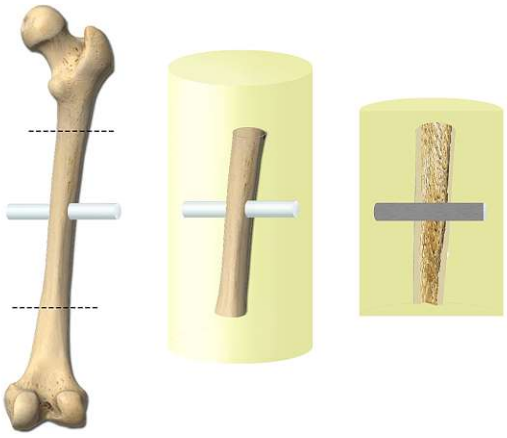

Figure 25: Cutting procedure. The proximal and distal epiphysis of the femur were trimmed along the dashed lines (left), followed by embedding the diaphysis. The yellow cylinder represents the embedding material (middle). The embedded bone was then longitudinally sectioned (right), and thin slices were cut off from this block for subsequent mechanical tests. Adapted from [29].

To prepare thin sections, the embedded bone was trimmed parallel to the longitudinal axis of the femur diaphysis and through the central axis of the pin (Figure 25, right).

Bone tissue slices in the range of 200—300 μm were cut along the diaphysis using the Accutom-50 saw and a diamond wheel under constant water irrigation. To minimize sample heating and tissue damage, the feed rate was set to 0.05 mm/s with 3000 rotations per minute. Corrozip (Struers, Germany), a corrosion inhibitor, was added to the cooling water. For the sake of completeness, it has to be mentioned that the chosen thickness for the bone slices was determined considering the utilization of the same samples in other experiments. The fixation of the bone slices onto the aluminum SEM sample holder required the use of a two-component glue, UHU® Plus Endfest, based on an epoxy-resin formulation. The glue has to cure for at least 24 hours to reach optimal hardness.
For nanoindentation experiments, the samples were carefully ground and polished in several steps to produce plan-parallel slices containing the cross-sectional area of the diaphysis with the implanted pin (Figure 25). The grit size of the silicon carbide abrasive papers (Struers GmbH, Willich, Germany) decreased from 500 to 4000 in four steps. To avoid contamination of the samples with a liquid suspension, the polishing process was based on the usage of diamond foils (Allied, CA, USA), starting from 6 μm and successively decreasing to 0.01 μm to ensure that surface roughness is lower than the final indentation depth. Unless otherwise stated, all steps and measurements were performed at room temperature.

4.3 Microscopy

To get an overview and to visualize the microstructure, bone-implant interface, and implant degradation progress, two imaging instruments were employed: a digital light microscope VHX 5000 (Keyence, Osaka, Japan) and a scanning electron microscope (SEM) Quanta 250 FEG, (FEI, OR, USA) for enhanced resolution. The SEM was operated in the backscattered mode at an accelerating voltage of 20 kV. Since elements with higher Z backscatter primary electrons more efficiently than lighter elements (low Z), they have a brighter appearance in the image [176]. This property facilitates the differentiation of individual areas, such as mineralized tissue or unmineralized callus. A Schottky field emission gun (FEG) serves as an electron source. The overview images were captured at 55 × magnification with an image resolution of 2048 × 1768 and a dwell time of 3 μs. The working distance was kept at approximately 11 mm ensuring optimal imaging conditions.

4.4 Micro-Computed Tomography (μCT)

Micro-computed tomography is a non-invasive and non-destructive imaging method. To visually analyze implant degradation over time, *in vivo* μCT scans (Siemens Inveon) were performed at different time points after implantation, depending on the sacrifice time points. Therefore, the animals were anesthetized by volatile isoflurane. Usually, scans were made at weeks 2, 4, 6, 12, 18, 24, and 52 post-operation with a resolution of 56 μm per voxel.

4.5 Nanoindentation

To investigate the mechanical properties, particularly the local variations in stiffness (quantified through Young's modulus) and hardness at the bone-implant interface compared to areas further away from it, nanoindentation experiments were performed on a Nanoindenter G200 (KLA, CA, USA) (Figure 26) in the transversal direction of the femurs.

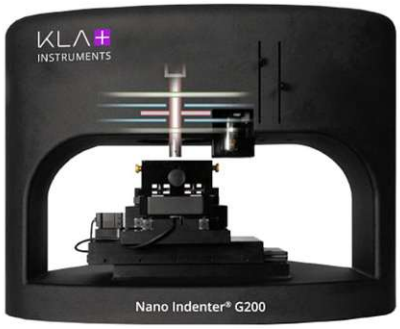

Figure 26: Nanoindenter G200 used for all experiments.

The system is equipped with a continuous stiffness measurement unit that enables the recording of contact stiffness, along with load and displacement data. Thus, a direct and continuous acquisition of Young's modulus and hardness as a function of indentation depth is feasible. This method is relatively insensitive to thermal drift [197]. The superimposed force signal operated at a frequency of 45 Hz, using a displacement amplitude of 2 nm. The experimental protocol comprises several steps, illustrated as a trapezoid loading scheme in Figure 27a. The first step encompasses loading until reaching a maximum indentation depth of 1 μm at a constant strain rate of 0.05 s^{-1}. Then, the load was maintained constant for 5 s, followed by a load reduction, and after 90 % of unloading, another hold was executed for thermal drift correction. The corresponding load-time (P-t) and load-displacement (P-h) profiles are depicted in Figure 27a and b.

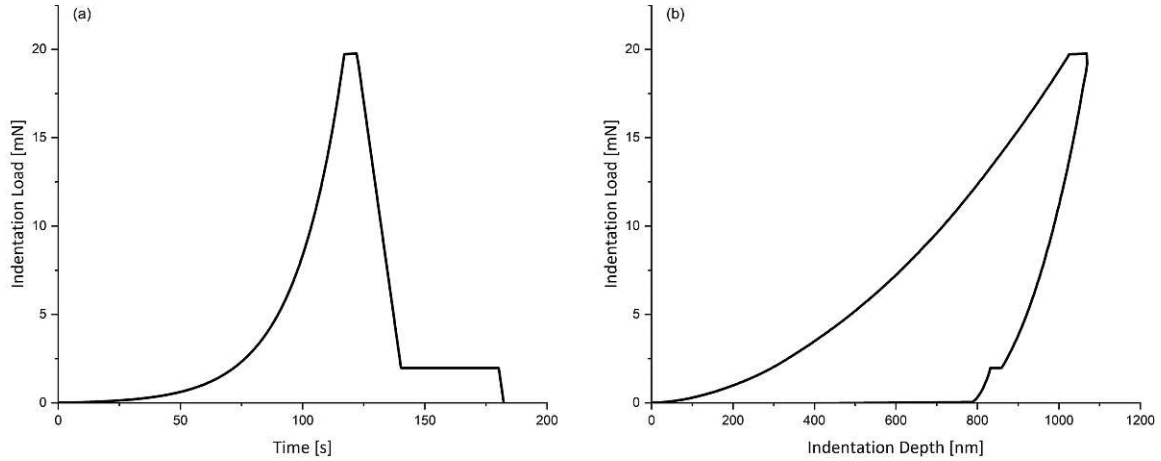

Figure 27: a) A typical load-time (P-t) curve for nanoindentation tests conducted with a trapezoidal loading scheme to determine the mechanical properties. The different steps of the measuring protocol are represented: loading to a maximum penetration depth; holding plateau (5 s); unloading until the ratio (P/P_{max}) reaches 90 %; another holding plateau, followed by the final unloading. b) A typical load-displacement (P-h) curve.

To avoid mutual interference of the indents, a minimum distance was set to at least 25 μm (Figure 28). This choice aligns with the established criteria to prevent overlap of neighboring plastic strain zones beneath the indents [206]. For each sample, indentations were made, starting adjacent to the implant-bone contact area and progressing perpendicularly away from that interface in 25 μm increments. Along the x-axis, which is parallel to the implant, a distance of 50 μm was chosen, resulting in an overall array with dimensions of $400 \times 200\,\mu$m. As a reference, two additional arrays were made further away from the implant into the intact host bone, which is not directly affected by implantation. The region of interest was selected individually based on bone morphology. A diamond Berkovich tip (Synton-MDP, Nidau, Switzerland) was utilized for all experiments. As tips commonly deviate from this perfect behavior, the actual area function was determined through indentation tests on a reference sample of fused quartz ($E = 72$ GPa, $\nu = 0.17$), according to the analysis established by Oliver and Pharr [182]. Measurements were performed for each sample in both newly formed and bulk bone tissue. The reported hardness and Young's modulus values represent the average within the indentation depth range of 500 nm to 1000 nm. Only indents in mineralized tissue were considered, while those in resin-filled structures, such as osteocyte lacunae, blood vessels, and cracks, were excluded.

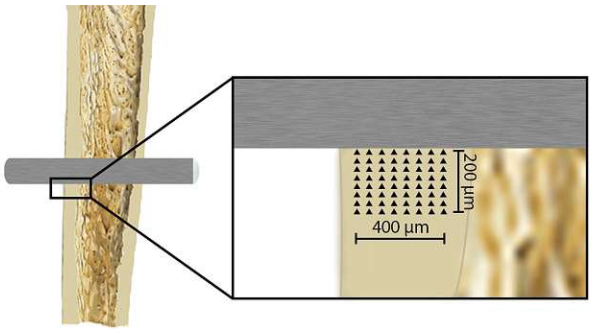

Figure 28: A nanoindentation array of $400 \times 200\,\mu$m in size, positioned at the bone-implant interface, displaying indents marked with black triangles. Note that this illustration is schematic. Adapted from [29].

4.6 Energy-Dispersive X-Ray Spectroscopy

Energy dispersive X-ray spectroscopy (EDX) is a non-destructive technique based on an interaction between some source of X-ray excitation and a sample. It is employed to analyze a material's elemental composition. Incident high-energy electron beams excite and eject inner shell electrons, creating electron holes. As another higher-energy-shell electron transitions into this vacancy, the energy difference between the two energy levels is emitted as characteristic X-rays [207]. The position of the measured peaks in the resulting spectrum gives information about the present elements, while the peak height offers insights into their concentration. The Ca concentration was measured in the same regions where the previous indentation measurements were positioned to establish a correlation between composition and mechanical parameters. Following mechanical testing, specimens were sputter-coated with a thin conducting layer of carbon using the scancoat six (Edwards GmbH, Burgess Hill, UK) to avoid sample charging. The samples were examined using an SEM equipped with an EDX detector, operated at 20 kV accelerating voltage, $140\times$ magnification, and 11 mm working distance.

4.7 Statistical Analysis

Statistical tests were conducted to assess the impact of the degrading implant on both the mechanical properties and the chemical composition, using the Kruskal-Wallis and Welch test. The statistical significance level was set at $p < 0.05$. Furthermore, linear regression analyses were performed to identify correlations between mechanical parameters and chemical composition. Correlations were reported as the coefficient of determination (R^2).

5 Results

In this work, seven female Sprague Dawley rats® aged six weeks were subjected to bicortical implantation of cylindrical ZX00 pins in the femur diaphysis. These animals were randomly assigned to different euthanasia time points, specifically 2, 6, 18, 24, and 52 weeks post-implantation. At these designated intervals, the femurs were extracted to investigate influences resulting from degradation at the bone-implant interface. The bone specimens were embedded, sectioned, and prepared through grinding. Afterward, the microstructure was analyzed using light and scanning electron microscopy. Additionally, μCT images were taken. Nanoindentation experiments were performed to estimate the influence of the degrading implant on the mechanical properties of the bone in regions of differing tissue age. Finally, EDX measurements were used to evaluate the effects of the degradation on the chemical composition.

This chapter presents the acquired measurement outcomes. The first section mainly entails a visual characterization of different samples, while the second part focuses on nanoindentation tests, mechanical properties, and tissue composition. In this study, the area directly surrounding the implant was defined as the bone-implant interface. The regions lying in close proximity to the implant (approximately 400 μm perpendicular to the implant) are referred to as newly formed bone tissue, whereas bone tissue located further away from the implant is denoted as bulk or mature bone.

The following results elucidate the mechanical changes of bone in proximity to the implant as well as at a distance from it and show the relation with age. Additionally, these mechanical properties were also correlated with the bone's composition.

5.1 Micro-Computed Tomography

After the implantation procedure, micro-computed tomography scans were performed at different time points to evaluate the degradation rate of the implants and to monitor the osseointegration in the femoral diaphysis. The Medical University of Graz kindly provided the data. The μCT images were then edited using the medical image processing software Mimics® (Materialise NV, Leuven, Belgium). In general, the results indicated fast osseointegration. Immediately 2 weeks after implantation, a network between the implant surface and the adjacent bone, along with new bone formation, could have been observed.

One sample (Figure 29) exhibited a slightly damaged bone (lateral side), which might be assigned to the drilling procedure during the implantation operation. An enhanced neo-formation of bone tissue around the implant was observable. At the medial side, a network between the implant and the adjacent bone started to be formed.

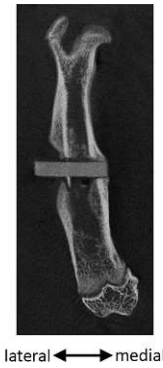

Figure 29: A μCT image (ID: 2644) taken 2 weeks postoperative reveals minor damage to the bone, likely incurred during the implantation procedure.

A discrepancy between the left and right femur of the 24-week sample was noted. Two weeks after the surgery, the two femurs looked almost similar (Figure 30, yellow). Whereas at 24 weeks, a clear difference was detectable (Figure 30, orange). No gap between implant and bone was present on the left femur, and a tight bone-implant interface was built with increasing implantation time. In contrast, a gap was formed on the right femur. At the bone-implant interface on this side, osteoconduction and osseointegration were inadequate at 24 weeks postoperative. Interestingly, this gap between bone and implant was more prominent and better detectable at the proximal end. Additionally, a darker shadow was visible in the μCT image, potentially indicating the presence of a gas bubble (Figure 30, turquoise arrow). Moreover, it seems that sclerotic rim formation took place. Notably, augmented bone formation was observed at the proximal site.

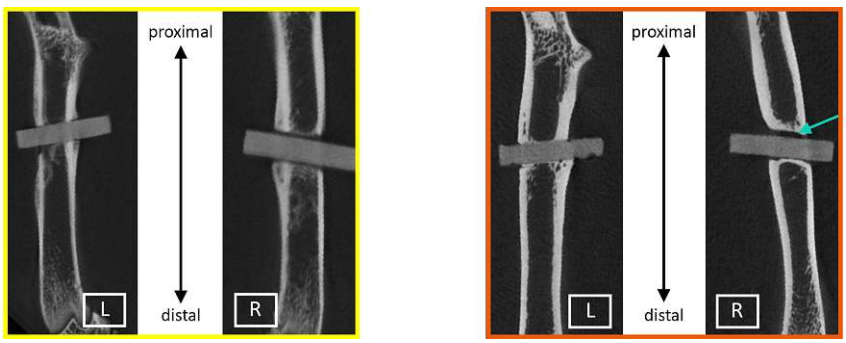

Figure 30: μCT images of the left and right femur (ID: 2466) depict distinct conditions. Yellow: 2 weeks post-implantation. Orange: 24 weeks post-implantation. The left side shows a tight bone-implant interface without gaps. Conversely, no network between bone and implant was formed on the right side. A gas bubble is noticeable at the proximal side of the implant (turquoise arrow).

In Figure 31, a μCT model is shown, representing the mentioned gap at the proximal side of the implant in the right femur. Despite the occurrence of new bone formation, no network between the bone and implant was established on this side.

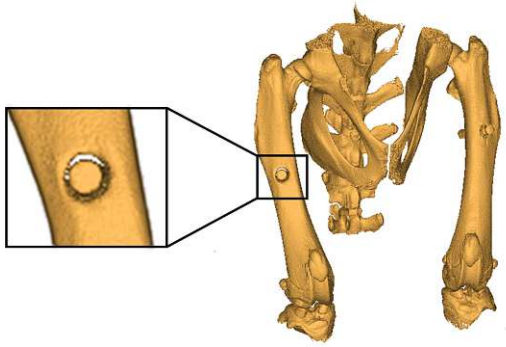

Figure 31: A μCT model of both femurs (ID: 2466) taken 24 weeks after the implantation. On the right femur, neither sufficient osteoconduction nor osseointegration occurred at the bone-implant interface (black rectangle). A noticeable proximal gap exists between the implant and the bone.

5.2 Microscopy

In addition, a visual characterization was performed using light microscopic imaging (Figure 32) to provide a comprehensive overview of callus and new bone formation, implant degradation, and the interface between the implant and bone. These images represent the trimmed femurs described in Section 4.2, where the implants were oriented perpendicular to the long axis of the diaphysis. In the images, the callus and medullary cavity appeared brownish. Two weeks after implantation, fibrocartilaginous callus formation around the pin was noticeable (Figure 32A). A close contact between bone and implant can already be seen 6 weeks after implant placement. Figure 32C shows the damaged bone mentioned in the previous section. The bone initiates healing this relatively big gap (left corticalis, below implant) by new bone formation. It seems that the callus and newly formed bone tissue were tightly attached to the implant. The aforementioned bubble between the implant and bone is visible in Figure 32F. In general, the corticalis tended to get thicker in the vicinity of the implant. The degradation rate was relatively slow. During the preparation procedure, the implant of the 52-week sample fell out. However, it is evident that the implant would still be preserved to a large extent even after the entire study period of 52 weeks (Figure 32G). Visually, the implant was degraded by only a few percent of its original volume. For a more detailed representation, SEM images were also captured.

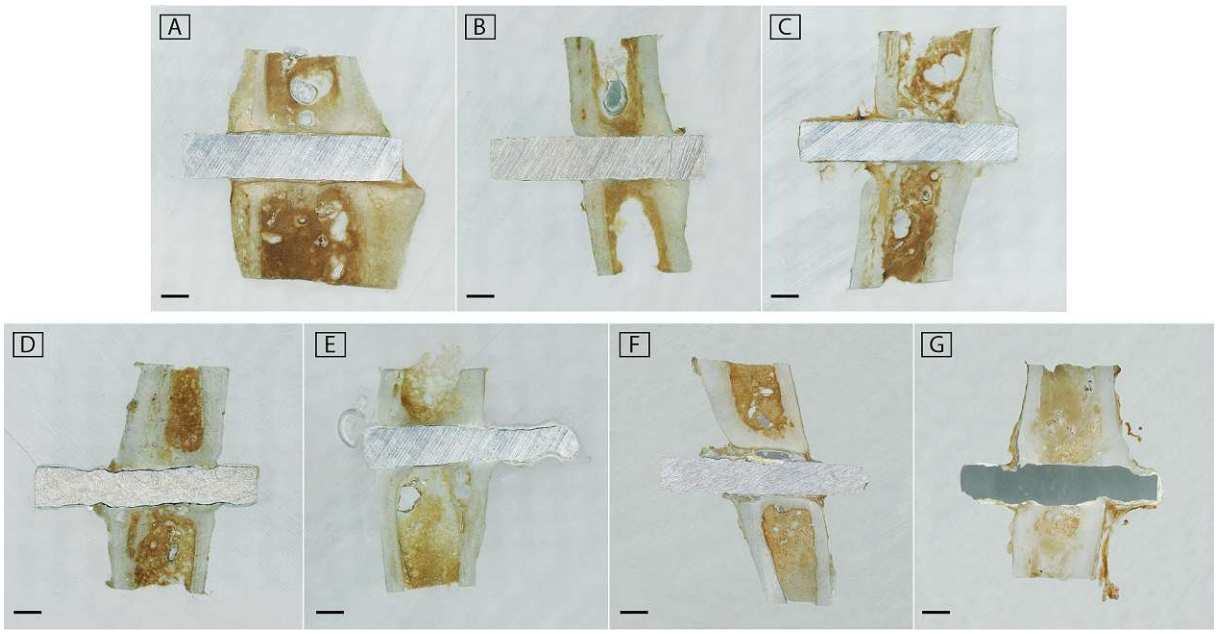

Figure 32: Light microscopic images of extracted and prepared femurs at various time points are presented: A) 2 weeks, B) and C) 6 weeks, D) 18 weeks, E) and F) 24 weeks, and G) 52 weeks postoperative. The scale bar corresponds to a length of 1 mm.

SEM images allowed the identification of successful bone and implant surface contact 6 weeks post-implantation. Subsequently, this contact resulted in bone adherence, consequently leading to the formation of new bone around the implant surface, as visible at 6, 18, 24, and 52 weeks postoperatively (Figure 33). No gas formation was observed throughout the study except for the t24_2466 sample. Two weeks after implantation, the healing process was characterized by a large amount of endosteal and periosteal primary bony callus (Figure 33A, pink and violet arrows). The implant was surrounded by fibrous tissue (Figure 33A, yellow arrow), appearing black in the SEM image. However, when compared to the light microscopic image (Figure 32A) or even to the SEM image taken with SE (Figure 34), it was feasible to distinguish new tissue from a gap. Enhanced neo-formation of bone tissue, especially around the implant, was observable (Figure 33A). The endosteal callus filled the bone marrow cavity near the implant site (Figure 34, labeled EC). As healing progressed, it gained in compactness, thus sealing off the marrow cavity at both sides of the implant between the cortices (Figure 34, labeled as CO). SEM images reveal that the implant was covered with this thin layer of newly formed bone, evident along the implant's surface at the top and bottom side after 6 weeks (Figure 33B, red arrow). The periosteal callus exhibited a porous appearance with numerous holes (Figure 34, labeled as PC). The first corrosion pits on the implant surface became visible 6 weeks postoperative (Figure 33B, orange arrow). Pits and dents were detected, espe-

cially where the implant was surrounded by tissue until the end of the period of 52 weeks (Figure 33B and E). Increased endosteal bone mass was noticeable (Figure 33E). In some instances, augmented periosteal bone mass was also observed (Figures 33A, C, and G). The bone in Figure 33A exhibited slightly different bone characteristics compared to the other samples. The corticalis appeared thinner and had a spongy structure, potentially attributed to a higher turnover rate in this sample. A noticeable gap between the bone and the implant surface was marked by a green arrow (Figure 33B, E, and F). A substantial gas formation occurred in the intramedullary cavity (Figure 33F). Generally, cortical bone structures were thicker around the implant, indicating bone remodeling and good osteoconduction. At the end of the 52-week observation period, the implant was still intact, and remainders could have been detected. In two cases (Figure 33D and G), the implant had broken out since these samples are delicate and had been used for other experiments before being affixed to the sample holder. Thin, unfixed slices tended to curl, making it even more challenging for further undamaged processing, which was not possible in two cases where a part of the cortical bone was damaged (Figure 33D and F).

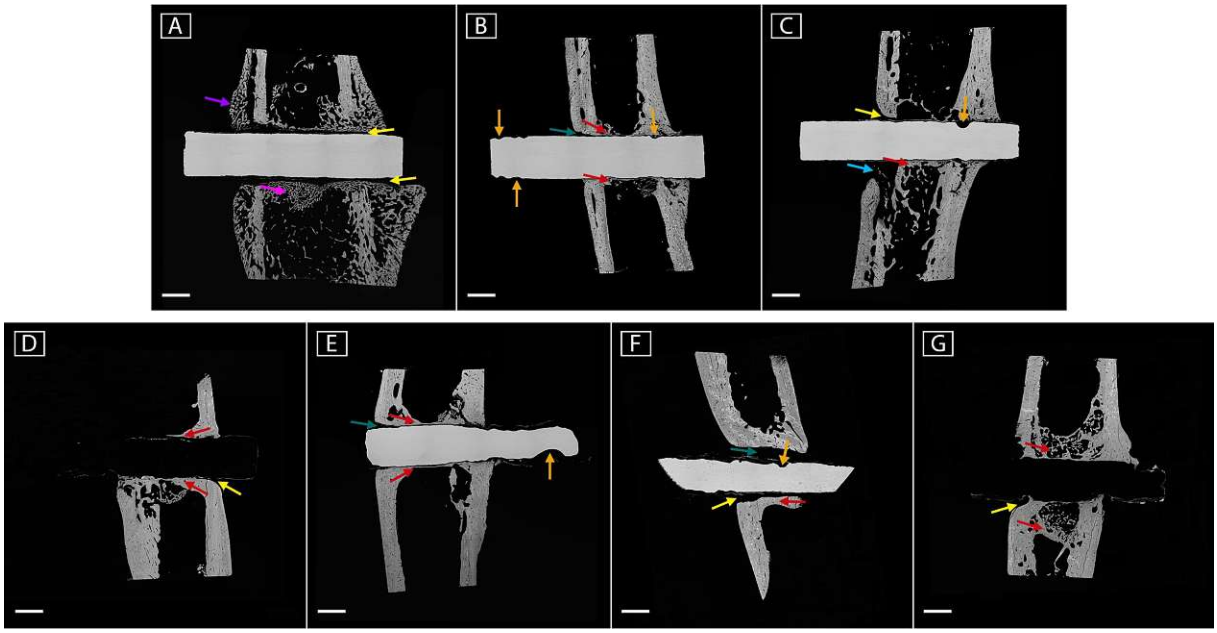

Figure 33: SEM/BSE images of explanted and prepared rat femurs at various time points are presented: A) 2 weeks, B) and C) 6 weeks, D) 18 weeks, E) and F) 24 weeks, and G) 52 weeks postoperative. Different arrows are used to highlight specific regions: fibrous tissue in yellow; implant corrosion in orange; endosteal and periosteal callus in pink and violet; new bone in red; the gap between the implant surface and bone in turquoise; damage due to implantation in light blue. The scale bar corresponds to a length of 1 mm.

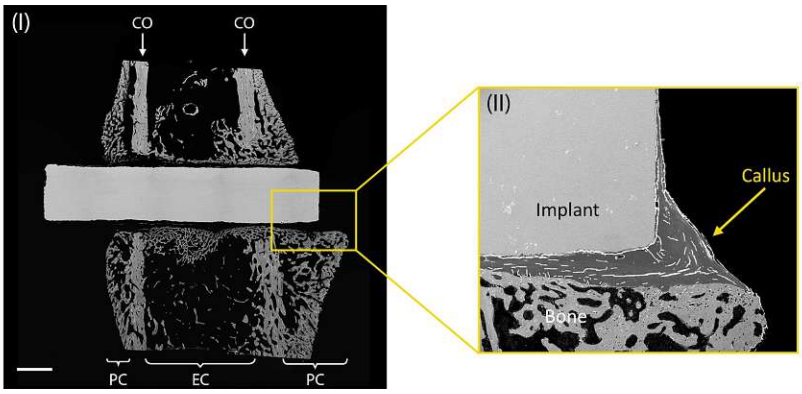

Figure 34: Callus formation (I): BSE image (t02_2672). The cortices are labeled as CO, and the areas of endosteal and periosteal callus are denoted as EC and PC, respectively. (II): Magnified SE image of the highlighted yellow region. The gap between the implant and bone is mainly filled with soft callus (fibrocartilaginous tissue). The callus is evident between the implant and the bone. The scale bar corresponds to a length of 1 mm.

Using SEM imaging, variations in the mineral density are distinguishable through differing shades of gray, as evident in Figure 35 for a 6-week (I, II) and 24-week (III, IV) sample. The magnified views in the right panels show the interfacial area between the implant and bone, highlighted by the red rectangles in the left panels.

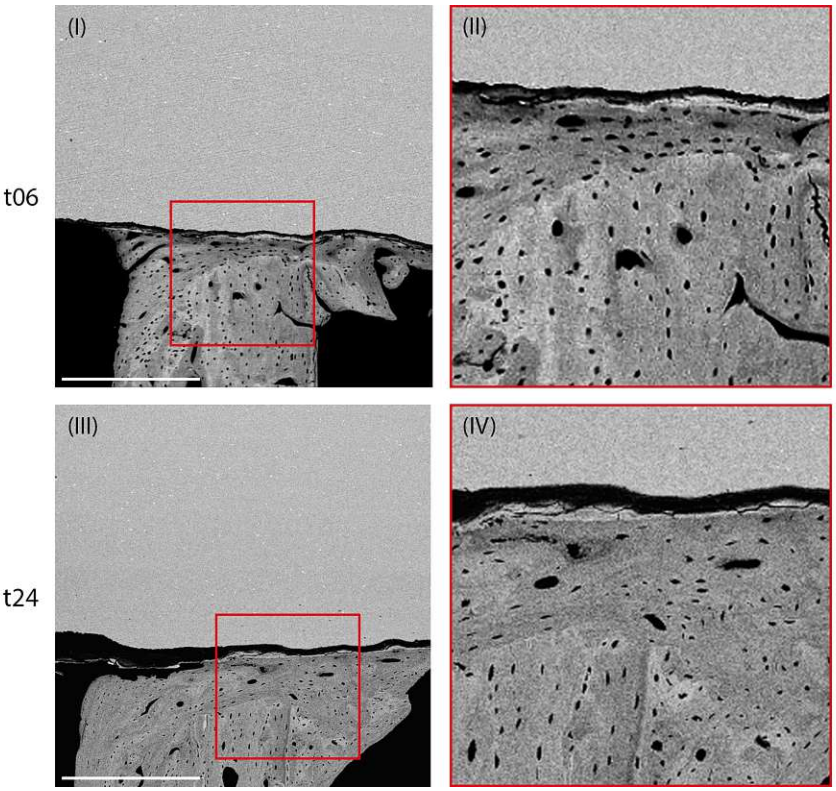

Figure 35: SEM/BSE images exhibit variations in mineral density shown as different shades of grey for samples at 6 weeks (top: I, II) and 24 weeks (bottom: III, IV). The images on the right illustrate the magnified areas (red rectangle). Notable differences in osteocyte lacunar density (appearing as black dots) can be detected between 6- and 24-week samples. The prominent dark canal at the lower right corner of the magnified t06 sample indicates a blood vessel canal extending from the bone marrow cavity into the bone. The scale bar corresponds to a length of 500 μm.

As the bone structure evolves from immature woven to mature lamellar bone with age, changes in osteocyte lacunar density (appearing black) can be observed. It seems to decrease with time (Figure 35), consistent with findings presented in [208] for human bones. Notably, in the magnified image of the t06 sample (Figure 35, II), a conspicuous dark canal is visible, representing a blood vessel extending from the endosteal surface into the bone.

5.3 Nanoindentation

To be able to make a statement about local variations in hardness and stiffness induced by implant placement and subsequent implant degradation, nanoindentation measurements were conducted, facilitating the differentiation of the mechanical properties at the implant-bone interface and those further away. In the subsequent section, the mechanical properties acquired through nanoindentation are presented.

Nanoindentation tests were performed using the protocol described in Section 4.5 on thin longitudinal slices in the transversal direction. The regions of interest (ROI) were selected manually to account for differing junction widths between the implant and bone. The aim was to maintain similarity between the chosen ROI, ensuring identical dimensions to enhance result comparability and minimize errors. The appropriate choice of ROI should avoid falsifying the measurement arising from the presence of pores and lacunae within the bone. Previous studies have shown that implantation can induce microdamage in bone extending up to hundreds of micrometers. Furthermore, the modulus tends to increase until about 150 μm with increasing distance from the implant site, adjacently flattens out, and remains relatively constant [209]. Hence, for this study, the indentation array size was set to 200 μm perpendicular to the implant. An SEM image after a nanoindentation measurement, demonstrating an indentation array, is displayed in Figure 36. To establish a relationship between femoral mechanical parameters and the age of the animals, these parameters were plotted against healing time. The resulting data is visually illustrated using boxplot diagrams, additionally depicting bone heterogeneity.

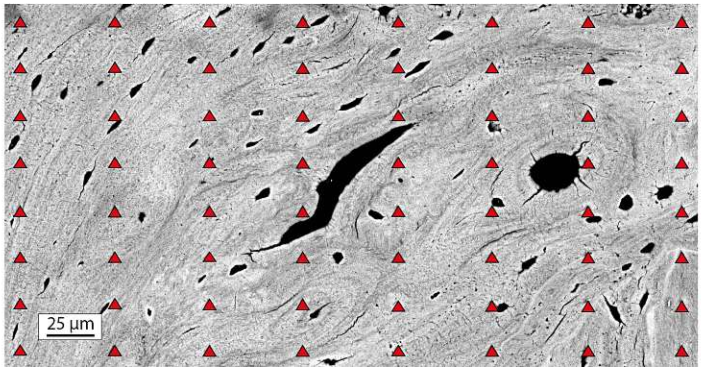

Figure 36: The scanning electron microscope image displays a typical nanoindentation array on bone. Since the indents are tiny, they are highlighted by red triangles. However, these triangles do not perfectly match the actual size of the indents.

5.3.1 Load-Displacement Curve

In Figure 37, load-displacement curves of newly formed and mature bone are presented and illustrate their distinct behavior. The plot depicts a representative curve for new bone (shown in red) and mature, bulk bone (shown in blue) oriented in a transverse measuring direction. Given that the nanoindentation experiments were path-controlled, the load-displacement curve for the new bone deviates from the mature bone in terms of the maximum load. At a maximum displacement of 1000 nm, the harder and more calcified mature bone attained a higher load, a steeper curve inclination, and a higher Young's modulus compared to the newly formed bone tissue.

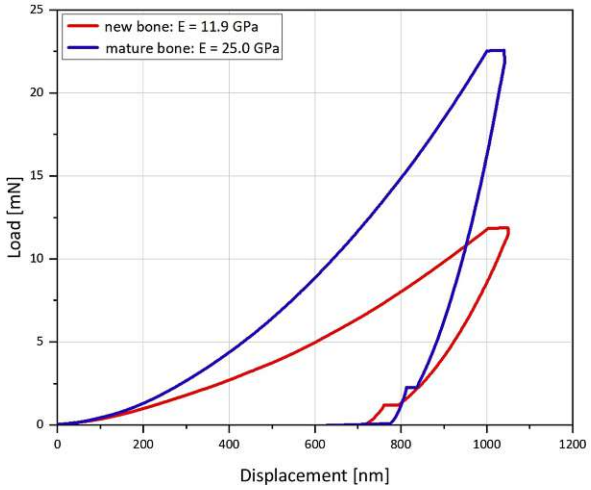

Figure 37: Representative load-displacement curves. Two randomly selected nanoindentation measurements demonstrate the load-displacement curves of newly formed bone (red) and mature bone (blue). At the same maximum displacement, mature bone achieved a higher load and Young's modulus.

5.3.2 Mechanical Properties

The results obtained from nanoindentation experiments for the indentation modulus and hardness, conducted on both newly formed and bulk bone at each healing time, have been

summarized in Table 7. These values are expressed as the mean ± standard deviation. In this context, the term "healing time" pertains to the duration for which the implant remained in the bone and thus aligns with the different euthanasia time points.

The measured findings are graphically illustrated in Figure 38, showing Young's modulus of newly formed bone and bulk bone tissue. The data corresponds to regions close to the bone-implant interface as well as those situated further from the implant, all depicted as a function of the healing time (2, 6, 18, 24, and 52 weeks postoperative). Concerning the labeling, for instance, "t02" (t = time point) signifies 2 weeks postoperative euthanasia. The mean value of Young's modulus and hardness, measured in newly formed bone tissue, displayed an increase over healing time. A variation in mechanical response with distance from the implant was noticeable. In particular, the mechanical properties were higher for bulk bone tissue compared to those of newly formed bone within the healing period up to week 24. Moreover, the Kruskal-Wallis test (E: $p < 0.05$; H: $p < 0.05$) demonstrated a significant effect of healing time on mechanical properties. The initially assumed hypothesis, suggesting enhanced biomechanical properties of bone as the distance from the implant increased, could be corroborated at first glance.

Table 7: The mean values ± their standard deviations for the mechanical properties obtained from nanoindentation experiments on newly formed bone close to the bone-implant interface and bulk bone further away from the implant. The measurements were conducted in the transverse direction of the rat femoral cortical bone.

Sample ID	Healing time [week]	Young's modulus [GPa]		Hardness [GPa]	
		New bone	Bulk bone	New bone	Bulk bone
2672	2	11.0 ± 4.8	16.2 ± 2.1	0.51 ± 0.23	0.72 ± 0.12
2642	6	15.1 ± 3.3	18.1 ± 1.0	0.61 ± 0.16	0.77 ± 0.05
2644	6	14.2 ± 5.2	18.2 ± 4.0	0.61 ± 0.22	0.77 ± 0.22
2570	18	16.7 ± 5.0	21.1 ± 2.3	0.77 ± 0.26	0.94 ± 0.15
2460	24	22.4 ± 1.9	23.9 ± 2.7	0.95 ± 0.11	1.03 ± 0.14
2466	24	23.7 ± 2.9	23.3 ± 1.8	1.03 ± 0.16	1.01 ± 0.12
2646	52	23.2 ± 3.8	21.9 ± 2.3	1.01 ± 0.19	0.90 ± 0.08

Figure 38 demonstrates the change in Young's modulus with healing time and, by extension, its correlation with distance from the implant. The Young's modulus values of newly formed bone tissue were notably distinct from those of the bulk bone tissue for almost all healing time conditions, except for one instance at 24 weeks (ID: 2466) and the

sample at 52 weeks. Statistical tests revealed, for example, that the Young's modulus of newly formed bone tissue (2 weeks, 11 GPa) in the bone-implant interface region varied from that of bulk bone tissue (2 weeks, 16.2 GPa) at a level of 0.001 significantly.

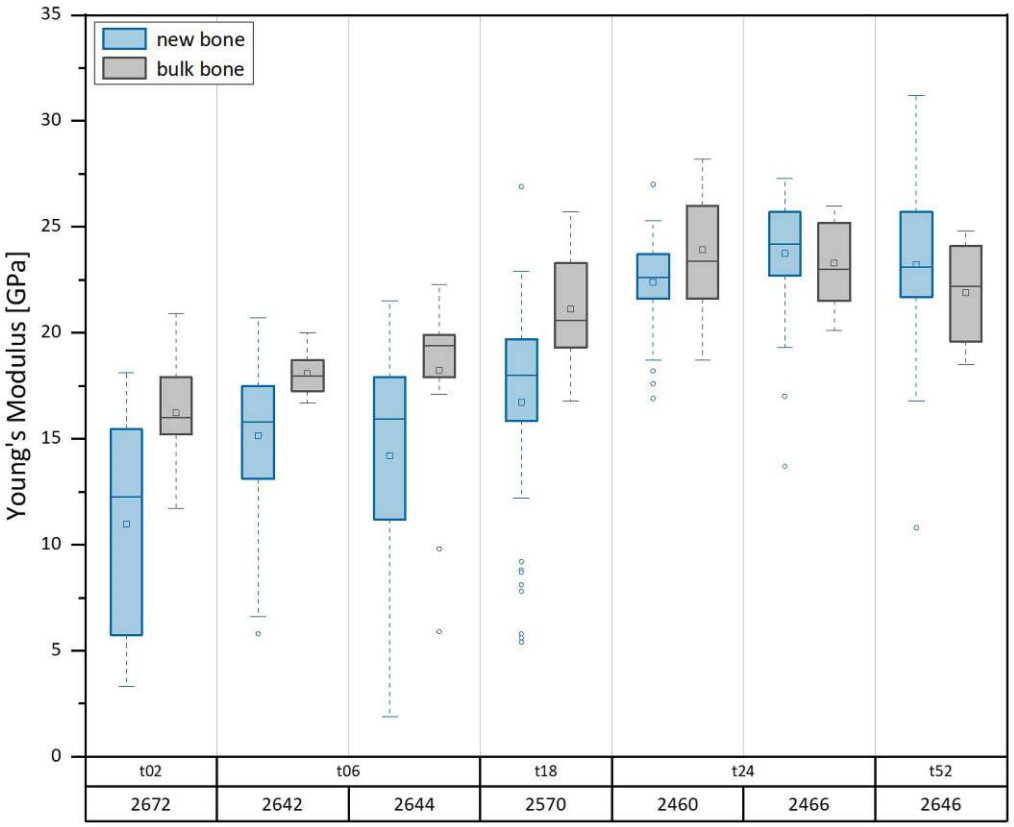

Figure 38: The Young's modulus exhibits variations with time and distance from the implant. The Young's modulus of newly formed bone, corresponding to the regions close to the bone-implant interface, as well as the Young's modulus of bulk bone corresponding to regions more distant from the implant, were measured using nanoindentation. These values were plotted against healing time (2, 6, 18, 24, and 52 weeks postoperative). Denotation: for instance, 2 weeks postoperative euthanasia is indicated as t02 (t = time point). The sample ID numbers are provided below each time point. Box limits indicate the range of the central 50 % of the data, with a horizontal line within the box representing the median. The rectangles show the mean values. Lines extend from each box to capture the range of the remaining values, with circles placed past the line edges to represent outliers. The corresponding numerical values are given in Table 7.

This behavior is visually illustrated in Figure 39, which presents a Young's modulus profile obtained from nanoindentation measurements. Based on the scale bar, lower values (blue, green) are assigned to regions near the implant, whereas higher values (red) correspond to areas further away from it. With increasing healing time, the Young's modulus values of newly formed bone progressively approached those of bulk bone. At 24 weeks, no significant difference was evident between the values near and away from the implant. The Young's modulus also increased with tissue age. The mechanical parameters of newly formed tissue showed a rapid initial change from 2 weeks to 6 weeks postoperative.

Subsequently, the Young's modulus slightly increased up to 18 weeks, followed by a more pronounced rise thereafter (week 24). The difference between the values in the newly formed bone at 2 and 24 weeks is statistically highly significant ($p < 0.001$). The values increased by more than 100 % in the period of 22 weeks from 11.0 GPa to 23.7 GPa. Linear regression analysis yielded a coefficient of determination of $R^2 = 0.98$ for the mean values. However, for a healing time of 52 weeks, the Young's modulus seemed to decrease again. The orders of magnitude of the obtained values are consistent with previous studies, as stated in Section 2.1.7.

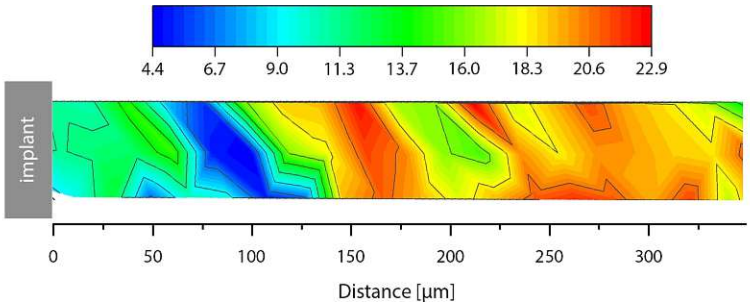

Figure 39: A Young's modulus profile derived from nanoindentation measurements. The scale bar is given in GPa. The trend observed indicates an increase in Young's modulus with increasing distance from the implant.

The hardness values, examined by nanoindentation experiments, for both newly formed and bulk bone, and different healing time points as detailed in Table 7, have been visually summarized in Figure 40. Bone hardness, predominantly governed by the inorganic mineral component, was assumed to increase over time and with distance from the implant. Comparing the hardness values between bulk bone tissue and newly formed bone for healing conditions by week 24, the former demonstrated higher values. This observation supports the hypothesis that bone tissue hardens with maturation, aligned with the progress of mineralization. Notably, the scattering of the data in Figure 40 is more pronounced than that of Young's modulus 38.

Discrepancies in hardness and Young's modulus values, in comparison to findings in existing literature, might be attributed to variations in bone maturation, species, or testing direction. Nevertheless, the orders of magnitude obtained for the Young's modulus and the hardness in this work align with previous research. In the case of healing for 24 weeks, the bone contains roughly equivalent calcified content as mature bone. The hardness values examined in this work exhibited a similar increasing trend to Young's modulus. For instance, a statistically significant decrease in hardness toward the implant from 0.72 GPa

to 0.51 GPa for a healing time of 2 weeks was found, which is highly significant at a level of 0.001. As healing progressed, the hardness values of newly formed bone approached those of bulk bone tissue. At 24 weeks, no statistically significant difference was apparent between values close to the implant and those further away. Moreover, hardness also increased with the duration of implantation. This is likely attributable to the growth of juvenile bone, resulting in a natural increase in bone hardness. Hardness showed a continuous, slight rise throughout the study period. Values doubled from 0.51 GPa at 2 weeks to 1.03 GPa at 24 weeks. However, for a healing duration of 52 weeks, the hardness of the bulk tissue seemed to decrease. No irregularities were detected in terms of mechanical properties due to implant degradation.

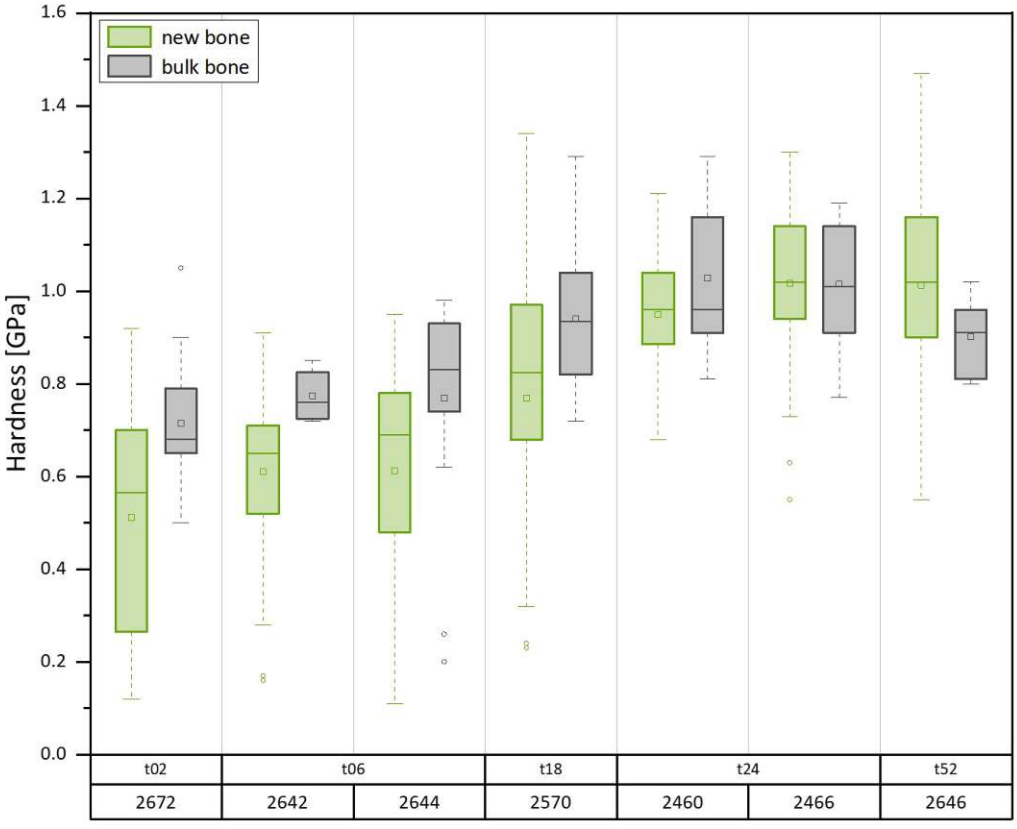

Figure 40: The hardness changes with time and distance from the implant. The hardness of the newly formed bone, which corresponds to the regions close to the bone-implant interface, as well as the hardness of the bulk bone corresponding to bone regions further away from the implant, were measured using nanoindentation. These values were plotted against healing time (2, 6, 18, 24, and 52 weeks postoperative). Denotation: for instance, 2 weeks postoperative euthanasia is indicated with t02 (t = time point). The sample ID numbers are provided below each time point. Box limits indicate the range of the central 50 % of the data, with a horizontal line within the box representing the median. The rectangles show the mean values. Lines extend from each box to capture the range of the remaining values, with circles placed past the line edges to represent outliers. The corresponding numerical values are given in Table 7.

5.3.3 Correlation between Young's Modulus and Hardness

The increasing trend of indentation hardness perpendicular to the bone-implant interface, illustrated in Figure 40 resembled the trend seen in Young's modulus (Figure 38). Consequently, a correlation between these mechanical properties was assumed. Analysis revealed a linear relationship between Young's modulus and hardness ($R^2 = 0.92$) within the bone tissue. However, a considerable amount of scattering is present (Figure 41). The depicted regression line (highlighted in orange) represents that Young's modulus is proportional to indentation hardness with a factor of $E/H \approx 25$, consistent with literature [210].

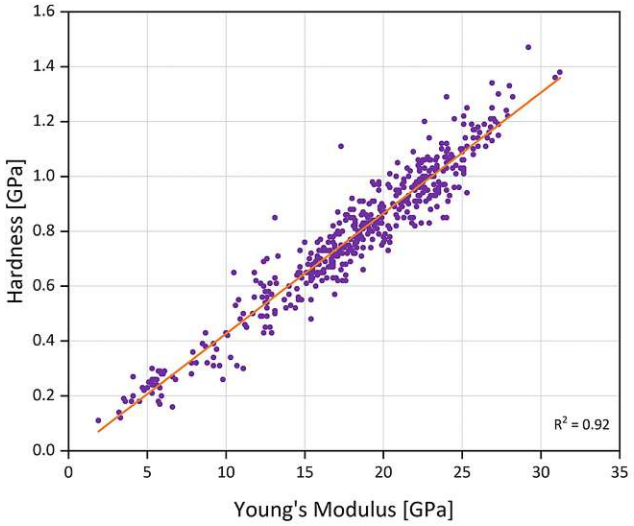

Figure 41: There exists a linear correlation between Young's modulus and hardness across all samples ($R^2 = 0.92$). The solid line shows the best fit linear regression.

5.4 Energy-Dispersive X-Ray Spectroscopy

EDX measurements were performed to obtain semiquantitative information on the chemical composition of the degradation layer and the Ca content in newly formed and bulk bone tissue.

5.4.1 Degradation Layer

The degradation layer formed due to the degrading implant was examined using EDX. Figure 42 depicts an SEM analysis of the longitudinal section from a 24-week sample (ID: 2460), combined with an EDX elemental mapping to investigate the elemental composition at the bone-implant interface. The BSE signal displayed lower atomic number values of the degradation layer compared to that of the bone tissue, resulting in a darker appearance. The area of interest at the bone-implant interface, analyzed by EDX, is highlighted in Figure 42 with a black rectangle. The four panels at the top right corner show the elemental distribution maps. They display the distribution according to their intensities within the scanned region: Mg is shown in yellow, oxygen (O) in purple, Ca in pink, and P in green. A line scan was selected from the corresponding elemental map and is plotted at the bottom of Figure 42. Intensities of Ca, Mg, O, and P were measured across the bone-implant interface. The specific region was marked by a dashed line in the upper left panel of Figure 42. The area for both the elemental maps and the line scan encompassed various regions, starting from the implant (I) and covering the degradation zone (II), the direct bone-implant interface (III), and the adjacent bone tissue (IV). Changes in the distribution of the selected elements along these regions were observable. Region I represents the implant and is characterized by high amounts of Mg (Figure 42). A noticeable decline follows in region II, accompanied by a simultaneous elevation of O, indicating the degradation layer of the implant. This region, spanning approximately 15 μm, was considered the known degradation by-product $Mg(OH)_2$ [92]. A small crack between the implant and the bone is discernible. An initial drop up to 45 μm and a subsequent increase in Mg with a peak at around 55 μm are evident. The direct bone-implant interface is characterized by this renewed Mg rise with a concurrent increase in Ca and P levels. Both peaks exhibit a drastic increase, starting at about 50 μm. Subsequently, Ca and P levels dropped again, while Mg experienced a slight delay in peak reduction compared to Ca and P. Moving away from the implant surface, gradually increasing Ca and

P levels were co-localized with low Mg levels until Ca and P content reached a plateau, representing mineralized bone. The O intensity demonstrates a steep decline after area III and stabilizes in area IV. Small variations in Ca and P levels in proximity to an osteocyte are also depicted at a distance of approximately 125 μm in the line scan.

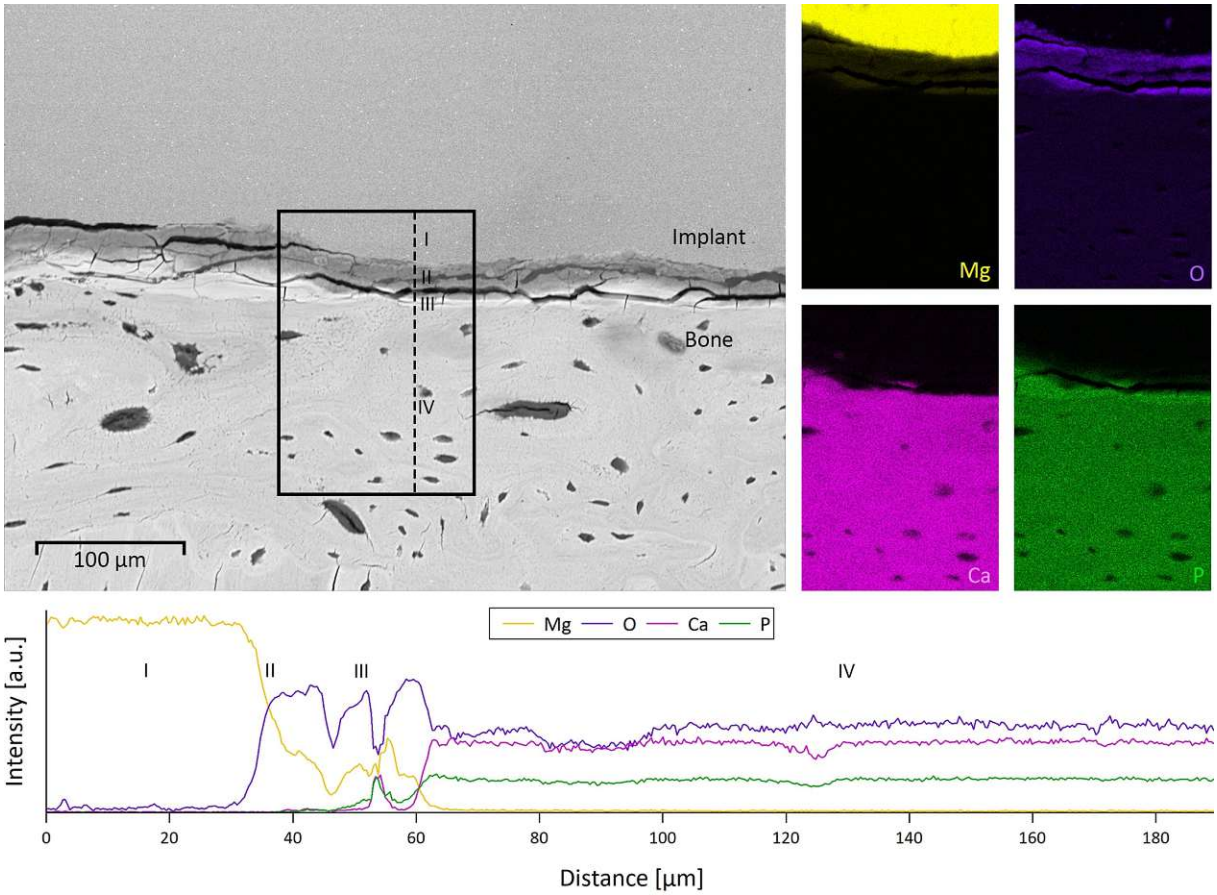

Figure 42: Top: SEM/EDX mapping of the bone-implant interface (ID: 2460, 24 weeks) in a sample cross-section. The SEM image shows the morphology of the bone-implant interface. The black rectangle outlines the interfacial region of investigation. The corresponding EDX maps (top, right panels) of the marked area (top, left panel) reveal the elemental distribution at the bone-implant interface: Mg is represented in yellow, O in purple, Ca in pink, and P in green. Bottom: A line profile from the corresponding elemental map was measured from top to bottom along the dashed line (top, left panel), indicating the presence of the degradation layer as Mg/O-rich. Additionally, it shows a gradual increase in Ca and P levels toward the bone. "I" denotes the implant region, "II" corresponds to the degradation zone, "III" designates the second layer in the degradation zone referred to as the direct bone-implant interface, and "IV" represents the bone tissue.

5.4.2 Mineral Content

To be able to quantify the Ca content, EDX measurements were performed. The mean values $\pm$ standard deviation for the Ca concentration in both newly formed and bulk bone are summarized in Table 8. The utilization of boxplots allowed for the graphical representation of the relationship between Ca concentration, tissue age, and distance to the implant.

Table 8: The mean values ± their standard deviation of the Ca concentration assessed by EDX measurements in newly formed bone close to the bone-implant interface and bulk bone situated further away from the implant in the cortical bone of the rat femurs.

Sample identifier (ID)	Healing time [week]	Ca concentration [wt%]	
		New bone	Bulk bone
2672	2	17.9 ± 4.1	22.2 ± 1.2
2642	6	20.2 ± 1.5	22.3 ± 1.8
2644	6	20.0 ± 2.1	22.5 ± 1.5
2570	18	20.5 ± 1.4	22.9 ± 1.6
2642	24	24.9 ± 1.2	26.1 ± 1.2
2466	24	25.5 ± 1.9	25.1 ± 1.8
2646	52	24.8 ± 2.3	24.0 ± 2.0

The degree of mineralization directly affects the mechanical properties of bone. Notably, a correlation between mechanical properties and Ca concentration has been established. Figure 43 displays the Ca concentration in newly formed bone in the proximity of the bone-implant interface and bulk bone corresponding to regions further away from the implant, observed for five distinct euthanasia time points. Differences in mineralization levels were observed, corresponding to the general bone development over time. Given the compositional heterogeneity of bone, the scattering of the data could be due to a natural gradient in tissue mineral content. Nevertheless, a discernible trend can still be seen in Figure 43. Until week 24, both the regions distant from the implant and those proximate to it had almost constant Ca concentrations. The newly formed bone at week two exhibited the lowest concentration, which then increased by the 6^{th} week. Then, it only slightly rose until week 18, and no significant difference was noted compared to the 6-week samples. Subsequently, a more rapid increase was detectable by the 24^{th} week. Among the postoperative samples at 24 weeks, the highest Ca content was recorded in the growing rat. A slight, non-significant drop was recognized in the 52-week sample in comparison to the 24-week sample. Notably, the youngest tissue (2-week sample) contained a quarter of the Ca present in the tissue with the highest Ca amount (24-week sample). The Kruskal-Wallis test revealed a significant influence of healing time on the Ca content. The determined concentration showed a similar course to that of hardness and Young's modulus. In the tissue up to week 24, the mineral content tended to rise less

rapidly than Young's Modulus and hardness, suggesting that the mechanical properties might not be solely explicable by the Ca concentration. Other factors, such as structural changes, could also contribute.

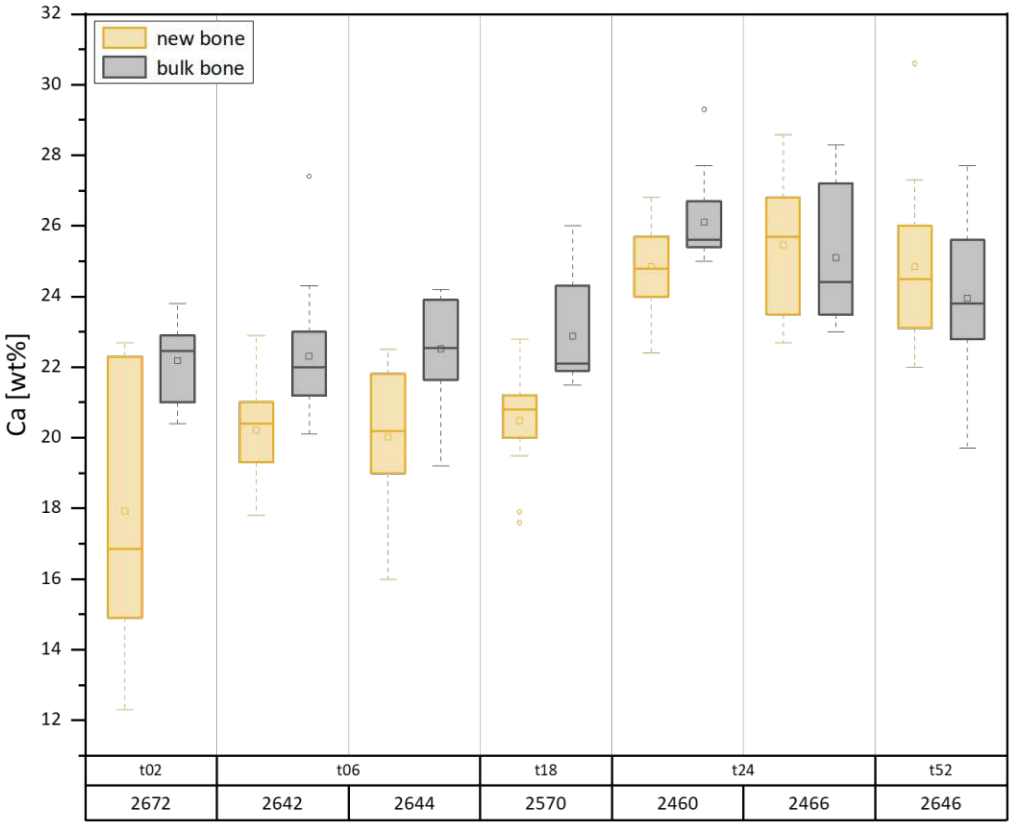

Figure 43: Change of the Ca concentration over time and distance from the implant. The term "newly formed bone" corresponds to regions close to the bone-implant interface, while "bulk bone" pertains to areas further away from the implant. The Ca concentration was assessed using EDX measurements and was plotted with respect to healing time (2, 6, 18, 24, and 52 weeks postoperative). For instance, t02 (t = time point) denotes the euthanasia time point and bone extraction operation 2 weeks after implantation. The sample ID numbers are provided below each time point. Box limits indicate the range of the central 50 % of the data, with a horizontal line within the box representing the median. The rectangles show the mean values. Lines extend from each box to capture the range of the remaining values, with circles placed past the line edges to represent outliers. The corresponding numerical values are given in Table 8.

5.5 Relation between Mechanical Properties and Chemical Composition

The Ca concentration was plotted among Young's modulus (Figure 44, left) and hardness (Figure 44, right) to examine the interrelationships between these variables. The underlying hypothesis was that variations in tissue age would lead to differences in mineral content, consequently affecting Young's modulus and hardness of bone material. Especially younger, less mineralized tissue was thought to be less stiff and hard than older, more mineralized tissue. The data demonstrate significant variations in tissue mechanical

characteristics as a function of tissue age and relate them to the chemical composition at the nanoscale. Here, finding the exact same measuring position is subjected to inaccuracy. However, as anticipated, the mechanical properties and chemical composition varied, corresponding to tissue composition and maturation levels. The average Ca content correlates moderately well with the Young's modulus and hardness (E: $R^2 = 0.95$ and H: $R^2 = 0.92$) (Figure 44). The concentration of Ca (Figure 43) and the mechanical properties (Figure 38 and Figure 40) assessed in this study increased in a similar manner with tissue age.

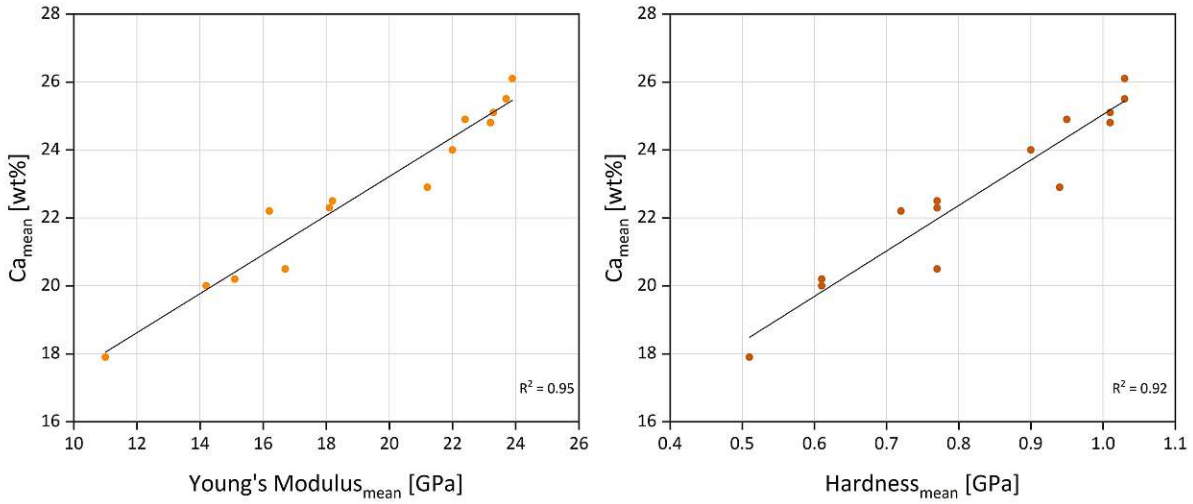

Figure 44: Correlation between Ca concentration and Young's modulus and hardness, respectively. Left: The mean Ca concentration is plotted against the mean Young's modulus ($R^2 = 0.95$). Right: The mean Ca concentration is plotted against the hardness ($R^2 = 0.92$). The solid lines represent the best fit linear regression.

6 Discussion

μCT

The μCT results generally demonstrated good compatibility with slow degradation and a tight bone-implant interface. The presence of newly formed bone tissue around the implant suggests that the ZX00 implant neither impeded bone healing nor hindered new bone formation. However, in one case, a discrepancy between the right and left femur of the 24-week sample was observed. A relatively large gap between the bone and the implant was evident on the right site, particularly at the proximal end. It seems that the drill hole diameter on the right femur was larger compared to the left, which could also affect the network formation. A darker region in the μCT image around the implant could be attributed to a gas bubble. A previous study stated that bone formation is more pronounced at the distal site of an implant in the diaphysis of a rat's femur due to the movement and the forces acting on the bone [211]. In contrast, bone formation was more distinctive at the proximal site in this work. A sclerotic rim formed in response to the pressure exerted from the H_2 bubble to provide mechanical support and protect the bone marrow [212]. Since the implant degrades moderately slowly, the pressure might not be too high and act like a force comparable to that of everyday movement, leading to a higher bone formation rate at the proximal site based on Wolff's law. Even though new bone formation occurred, no network was formed between bone and implant, which may be attributed to this H_2 pocket. If the gas formation rate exceeds the body's ability to remove it, H_2 accumulates and hinders an implant-bone connection. It is also worth mentioning that a tight bone-implant interface was established on the left femur, where no gap existed. However, all other samples showed the formation of new bone and a tight bone-implant interface, as well as a slow and homogenous degradation rate. These findings lead to the assumption that this type of implant fosters good osteoconduction and osseointegration.

Microscopy

Light microscopic images were taken to provide an overview of both new bone formation and implant degradation. Callus formation was observed as an essential stage of the heal-

ing process that bridges fractured bone gaps. By the second week post-operation, SEM images revealed the presence of callus (Figure 32A), which is in accordance with literature [59]. This implies that the ZX00 implant had no adverse effect on callus formation. In the subsequent bone remodeling process, excess material on the bone's exterior and within the medullary cavity is removed to restore the original bone architecture. The light microscopic images demonstrated a robust attachment between the callus, new bone tissue, and the implant. Therefore, it can be concluded that the Mg implant serves as a scaffold for new bone and exhibits good osteoconduction and osseointegration capabilities. Due to the slow and controlled degradation rate, visible changes concerning the overall implant volume occurring over the observed period are of minor magnitude. Previous investigations also showed that the ZX00 alloying system reveals gradual degradation rates, resulting in a 15 % reduction in mean implant volume compared to its initial volume over a 24-week period [213], a trend in accordance with the results of this work.

For enhanced visualization, SEM images were taken. Discrepancies between the μCT, light microscopic, and SEM images may arise from differences in cross-sectional views. The SEM images were acquired *ex vivo* rather than *in vivo*, as was the case with μCT image. Additionally, differences could result from the timing of image acquisition relative to the slicing and grinding processes. For instance, the distinction between Figure 32D and Figure 33D can be attributed to these factors. The series of SEM images revealed both a partially lacuna-shaped (pit corrosion) and uniformly distributed degradation of the implant, as well as an enhanced bone formation activity at the bone-implant interface and within the bone marrow. Pits were detected, especially in regions where the implant was surrounded by well-vascularized soft tissue. The mechanical forces caused by the musculature surrounding the bone-protruding implant might lead to an amplified degradation rate. This phenomenon can be circumvented in the implant's clinical application in humans by customizing the implant's length individually to match the patient's anatomy. SEM images made it possible to assess changes in osteocyte lacunar density (Figure 35), which refers to the number of osteocyte lacunae per bone area. As the healing time progressed, the density seemed to decrease, a trend similar to what was stated in the literature for human bones, and indicates the transition to a more mature bone [208]. Osteocytes are regarded as sensory cells that can detect local mechanical and biochemical conditions, transmitting signals to each other as well as to osteoblasts, consequently influencing the

bone remodeling response [208]. Interestingly, variations were noted in the orientation of osteocyte lacunae based on their maturation stage. The continuous implant degradation and a simultaneous bone healing process cause a constant bone-implant interface shifting. The healing front moves toward the implant center, resulting in altered loading patterns. As newly formed bone adapts to evolving conditions by orienting the bone architecture, collagen orientation might be influenced by stresses imposed by the implant. Figure 35 demonstrates such an adaptation in the region close to the implant, where fibers appear aligned along the implant axis. Due to a continuously changing healing front adjacent to the degrading implant, one can assume that the collagen orientation is steadily modified according to the shifting loading conditions. Once the implant degrades entirely, the collagen direction will finally be aligned along the main bone axis as a result of ongoing remodeling. It has to be mentioned that direct comparison of the 6-week and 24-week samples (Figure 35) in terms of their mineralization state is limited because the SEM images were individually adjusted for brightness and contrast for each sample. Thus, mineral density can only be visually compared within one sample. Within the brighter and more mineralized bulk bone, lacunae were preferentially aligned along the bone axis, conforming to the collagen matrix orientation and main loading direction. Conversely, lacunae were oriented more parallel to the implant in newly formed, less mineralized bone regions. Upon closer examination, magnified images show cracks that could have arisen as a consequence of ethanol dehydration and the polishing procedure undertaken during the sample preparation process.

Implant Corrosion, Gas Production and Degradation Layer

During the degradation of Mg, hydrogen gas, which is formed as a consequence of Mg degradation as part of the electrochemical reaction along with the generation of magnesium hydroxide, could potentially impact osseointegration and new bone formation. Previous studies have reported the highest level of hydrogen gas volume at around 18 weeks post-implantation. Over time, the gas evolution diminishes and eventually disappears. Since the implant degrades homogeneously and gradually, with a calculated degradation rate of approximately 0.08 mm/year [77], the formation of hydrogen was moderate and did not impair bone formation. It has been reported that the degradation rates vary depending on the implantation site, with the diaphyseal area exhibiting lower rates com-

pared to the epiphyseal region. These differences are attributed to higher epiphyseal perfusion [214]. Furthermore, the surrounding tissue is supplied with blood to a more considerable extent compared to bone, causing faster degradation (Figures 33B and E). Additional measurements at different bone sites are recommended for a comprehensive understanding of mechanical property differences attributed to various bone regions. An adverse effect of a hydrogen pocket concerning osseointegration was evident in just one case in this study (Figure 33F). A significant gap between the implant and adjacent bone was observed at the proximal side. No direct bone-implant contact existed, resulting in weak implant stability. The presence of such a gas bubble in only one sample may be attributed to an impurity at that specific site, potentially intensifying hydrogen gas generation. Kraus et al. [150] documented in experiments concerning Mg alloy degradation that gas formed during degradation exerted mechanical pressure on the bone, initiating increased callus formation and negatively affecting bone formation. Interestingly, in our case, the gas bubble did not impede bone formation but rather osseointegration. A higher degree of bone formation, especially within the medullary cavity, was obvious compared to the other samples. The gas pocket might have eventually dissipated in the subsequent weeks of implantation. However, no significant differences in mechanical properties were noted between the two investigated 24-week samples.

The implants used in this work are larger than those used in clinical scenarios. The size of the Mg implant is oversized relative to the dimensions of a rat's femur. Given the dissimilarity between bone structures in rats and humans – such as the absence of osteons in rats – and the smaller scale of rat anatomy, differences in blood flow can be presumed to exist, making direct comparison of corrosion rates challenging. In a study by Grün et al., the long-term bone tissue response to the ZX00 alloy was investigated using small and large growing-animal models. Their results showed a six-fold higher average degradation rate in a sheep animal model compared to rats [77]. Therefore, it is plausible that degradation may occur more rapidly in the human femur compared to that in rats or sheep. In addition, the force transmission differs between humans and quadruped animals like rats, where body weight is distributed across all four extremities. Metabolic and immunological changes due to diseases might also cause increased degradation of magnesium implants with larger amounts of gas formation [72,215]. Further investigations are needed to elucidate how implants behave during degradation *in vivo* within the context

of human subjects.

Furthermore, the degradation layer was investigated. It is not solely the formation of hydrogen gas that impacts bone development but also the corrosion layer itself. In aqueous environments, Mg degrades according to the reaction $Mg + H_20 \rightarrow Mg(OH)_2 + H_2$. This reaction leads to a protective $Mg(OH)_2$ layer encasing the implant, which mitigates the degradation rate. Through EDX analysis, it becomes feasible to distinguish between the implant and the bone matrix based on the prominent signature of Mg and Ca, respectively. In general, the implant volume is gradually reduced during degradation. Hence, the bone-implant interface is shifted toward the center of the implant, with newly formed bone tissue substituting for the vacant degradation site. There are two possibilities of bone formation during bone healing: contact osteogenesis and distance osteogenesis. In the latter, bone growth originates from the cut bone surface and extends toward the implant surface, while osteoconduction allows for contact osteogenesis to occur, where new bone forms directly on the implant surface [216]. Due to the effective osteoconduction of Mg implants, a combination of both variants can be assumed. The degradation layer, illustrated in Figure 42 as region II, is characterized by elevated levels of Mg and O. This region is recognized as the well-known degradation product $Mg(OH)_2$, produced by the degradation of the Mg alloy. Almost no Ca and P could be detected in this zone, with a small crack visible between the implant and the bone. One can expect that the bonding strength at the interface between the degradation layer and the newly formed bone tissue is the weakest. This might explain the initial decline to 45 μm and the subsequent increase in Mg at approximately 55 μm. This renewed elevation in Mg, coupled with a simultaneous increase in Ca and P in a second layer (Figure 42, region III), signifies the direct bone-implant interface. A degrading Mg alloy in the physiological environment experiences a local rise in the pH value. Due to that, the precipitation of calcium phosphate compounds can be triggered in close proximity to the implant surface. Thus, this initial increase in Ca and P (Figure 42, region III) might signify a layer primarily composed of calcium phosphates, aligning with literature findings [217]. One can conclude that the degradation layer exhibits a two-layer structure. The higher Mg concentrations in region II predominantly lead to the formation of $Mg(OH)_2$, while calcium phosphate crystallization took place in the lower Mg region III. Witte et al. [218] described an enrichment of Ca and P in the corrosion layer that forms around the implant during

degradation and was in direct contact with the surrounding bone tissue. Thereby, an increased formation of bone mass around the Mg implant was found, suggesting that the released Mg ions stimulate osteoblast activation and support bone formation positively. To make an accurate statement about this beneficial effect, further measurements and comparisons between samples with ZX00 implants and sham samples or other implant materials need to be conducted.

The usage of Mg-based ZX00 implants, characterized by their low degradation rate, may overcome the disadvantages associated with implants exhibiting significantly higher degradation rates and additionally meet the mechanical property requirements for stabilizing fractured bones.

Mechanical Values

Nanoindentation was employed to investigate differences in mechanical properties due to the continuous degradation of the ZX00 implant. It has to be mentioned that in this work, the term "Young's modulus" is used instead of "indentation modulus", as the former term is predominantly used in the existing literature. In this study, experiments were exclusively conducted on the right femur, as the left ones were reserved for other research purposes.

The fracture healing process can be divided into four main stages, as explained in Section 2.1.5. The mechanism of bone healing with an implant closely resembles those stages without an implant. Post-implantation, the initial stage entails hematoma formation. Subsequently, fibrocartilaginous callus forms to stabilize the bone and establish a network between the fractured ends and the implant. In rat models, soft callus formation peaks 7–10 days after surgery [59]. It gets then replaced by immature bone through endochondral ossification. The final stage of fracture repair involves remodeling, where the mature (lamellar) bone gradually replaces the immature (woven) bone in response to external load to restore the anatomical structure of the preinjured bone. This step starts after 3–4 weeks and can extend for several months [59]. Given that the earliest euthanasia time point for the samples used was 2 weeks post-implantation, the formation of callus and immature bone could already be expected. The ongoing degradation makes the whole fracture healing procedure more dynamic. Moreover, the implant-related alteration of mechanical forces results in modified loading patterns that could affect bone

healing. This phenomenon, known as mechanotransduction, is even more complex in the case of degradable implants [36]. Woven bone, a tissue produced during fracture healing attributed to the disorganized collagen fiber arrangement, possesses lower stiffness compared to mature lamellar tissue. Consequently, in this study, it was hypothesized that bone nearest the implant interface would be less stiff and less hard than bone located several millimeters from the implant. The obtained results were summarized in a boxplot diagram (Figure 38 and Figure 40). The results demonstrate that the mechanical properties assessed by nanoindentation vary with distance perpendicular to the implant and with the progression of time.

Introducing an implant into the rat's femur disrupts the natural development of mechanical properties. In general, a slight and, in most cases, statistically significant increase in stiffness toward the bulk bone tissue was detected along with the same trend for hardness. This behavior can be attributed to the presence of newly formed bone with a lower degree of mineralization at the bone-implant interface. The Kruskal-Wallis test revealed a significant effect of healing time on Young's modulus ($p < 0.05$) and hardness ($p < 0.05$) of bone tissue. This might be explained by the growth of juvenile bone and a closely related natural increase in bone stiffness due to the reorientation of collagen fibers. The mechanical parameters of the newly formed tissue exhibited a rapid initial change from 2 weeks to 6 weeks postoperative, which might be attributed to the Mg-ions released from the implant. The relatively low Young's modulus value of 11.0 GPa at the vicinity of the implant likely corresponds to the earliest stage of bone material. The considerable amount of scattering and, thus, the box height in the diagram is attributable to microstructural effects within the bone tissue and were more noticeable for hardness compared to Young's modulus data, possibly due to the smaller scale of the former parameter. Furthermore, in newly formed bone (Figure 38 and Figure 40), the scattering of the obtained values was higher than that of the host bone. These results imply that newly formed bone exhibits a broader range of Young's modulus, which may be explained by the heterogeneous mixture of multiple tissue types (granulation tissue, chondroid tissue, woven bone) present during early bone formation. Since the bulk bone tissue was primarily intended as a reference, fewer measurements were performed compared to the number in the new bone tissue, which might also affect the scattering of the data. But it may also be a consequence of implant degradation, as a localized elevated Mg content at the interface could impact

bone formation, resulting in deviations in mineral crystal structure and, thus, variations in the mechanical properties. It is known from the literature that bone is compositionally heterogeneous, and areas with distinct moduli hinder crack propagation associated with increased fracture resistance. To sum it up, the observed scattering seemed to be within a normal range [219].

The obtained results concerning healing time can be explained by variations in mineralization levels and changes in bone microstructure. The microstructure of newly formed bone differs from that of mature bone, particularly in terms of collagen fiber orientation. During the early stages of bone healing, the tissue frequently comprises woven bone with randomly oriented fibers, resulting in lower mechanical characteristics. Considering the relatively low Young's modulus for the 2-week sample and its distinct appearance as mentioned in Section 5.2, the possibility that this animal might suffer from cancer can not be excluded. Diseased bones, such as those affected by cancer, frequently exhibit an increased bone turnover associated with nanomechanical abnormalities, including reduced stiffness and a diminished mineral-to-matrix ratio [220]. Gauging the extent to which these measurements were affected is quite challenging, given that this sample represents the "youngest" in the set, and hence, lower mechanical properties were anticipated anyway. Nanoindentation experiments are susceptible to measurement errors in regions with higher lacunar density in younger bone, potentially leading to underestimated mechanical properties. Although measurements directly contacting blood vessels or osteocytes have been excluded, nearby areas may still exert influence on the results. Variations in these properties might also correlate with structural attributes like porosity. As bone matures, woven bone turns into lamellar bone, characterized by lower porosity. However, at a later stage, cortical porosity increases again due to the natural changes in the bone material with age. Zhang et al. [221] found biphasic progression in porosity. Porosity decreased linearly until seven months of age, followed by an increase at nine months. Considering that seven months corresponds to 28 weeks, those values found in the literature can be compared to the 24-week samples in this work, as the animals were 6 weeks old at the implantation operation. Thus, after 24 weeks of implantation, the animals reached an age of 30 weeks. Zhang et al. [221] also noted a variation in Young's modulus with age. Up to seven months of age, Young's modulus increased, aligning well with the findings in this work. After 24 weeks, the values for newly formed tissue became statistically

indistinguishable from those of bulk tissue. This concurs with existing literature, as rats are known to reach skeletal maturation at approximately 24–40 weeks [72]. Given the relatively large time gap between 24 and 52 weeks in this study, any alterations in mechanical properties during this period can only be inferred. Although the measured values at 52 weeks are slightly lower, they do not differ significantly from the 24-week values. Bone tissue quality is affected by age-related changes such as alterations in collagen and its cross-linking, non-collagenous proteins, and bone mineral crystals. Because of bone remodeling, a process involving bone formation by osteoblasts and bone resorption by osteoclasts, the properties of bone do not remain constant with age. In healthy and younger bones, an equilibrium between those two processes exists. However, in older individuals, the process of resorption exceeds bone formation, leading to worse bone tissue quality. Assuming that bone quality loss in rats proceeds in a manner analogous to humans could explain the decrease observed at week 52.

Disparities in Young's modulus and hardness values, when compared to those found in literature, may be attributed to several parameters. These might encompass variations in bone maturation, moisture content, species differences, anatomical site variations, testing methodologies and profiles, embedding materials, or the specific indentation depth region utilized for Young's modulus calculation [186, 222]. The testing direction is also relevant, given the anisotropic nature of bone [223]. Further complexity arises from the direction and load-dependence of the Poisson's ratio of bone, which impacts the measured values [67]. Performing indentation measurements on bone presents problems, as bone is an anisotropic solid that displays viscoelastic behavior. The widely used classical OPM for analyzing nanoindentation data assumes material elasticity and isotropy. However, as these prerequisites are not met by bone tissue, parameters derived from indentation measurements, such as Young's modulus and hardness, exhibit a dependency on the load-time sequence. Thus, it must be kept in mind that quantitative values should be taken with caution. Since this study aims to point out differences among seven samples, all prepared and tested in a similar way, this concern is less of an issue. Moreover, due to the animal movement acting on the implant and interface, forces vary between proximal and distal sites. If one side experiences higher loads on the bone-implant interface, the bone remodeling and formation process might be stimulated, potentially yielding higher values. Since nanoindentation measurements were performed at different locations with respect

to the implant, either proximal or distal, depending on the bone formation, differences in measured values are likely. Further measurements on both sides of the implant have to be made to determine if significant differences emerge due to these forces. It becomes evident that values from different studies cannot directly be compared. Depending on all those mentioned factors that might have an impact on the results, the focus in this study was placed on examining the relative differences between newly formed and bulk bone rather than absolute values. A uniform sample preparation method was applied across all femurs, and all results were acquired under the same conditions to obtain comparable values between the samples used in this set of experiments.

Given that the experiments involved growing animals, a time-dependent influence on the mechanical properties and bone tissue's chemical composition due to skeletal maturation remains a factor that cannot be ignored. However, the ZX00 alloy is mainly designed for pediatric orthopedic trauma [77, 175]. Bone metabolism varies between adults and children. Consequently, investigations involving these degradable implants should ideally be carried out in juvenile growing animal models, as the bone turnover rate of such animals aligns more closely with that of children [77]. It is important to note that conditions such as osteoporotic bone in elderly patients could exhibit completely different behavior in terms of degradation rate. This, in turn, could affect factors such as gas volume, new bone formation, and the mechanical properties of bone. However, no abnormalities in the mechanical properties attributed to implant degradation were observed. The order of magnitudes obtained for Young's modulus and the hardness in this study is consistent with previous research. Since the measured values converge with time, it leads to the assumption that the initial stiffness and hardness values can be received after complete implant degradation.

Chemical Composition

Alterations in bone composition directly impact the mechanical properties during the process of bone healing. For a better understanding and surgical success, it is essential to understand changes in mechanical and compositional properties over healing time at the bone-implant interface. The quality of the contact areas around the implant predicts surgical outcomes and determines the overall healing process of patients.

The interactions at the bone-implant interface are sophisticated, and the stages are com-

parable to those typically involved in fracture healing. In cases where the optimal conditions for repair are lacking, secondary fracture healing, characterized by callus formation, is expected. This occurrence depends on mechanical conditions and the distance between bone and implant [58, 224]. The initial formation of a soft callus can provide mechanical support, bridge the gap between bone and implant, and act as a template for the bony callus (Figure 34). Blood vessels invade the fibrocartilaginous callus, delivering osteoblasts, osteoclasts, and chondroclasts. Osteoblasts lay down osteoid, primarily composed of disordered collagen type I fibers. In a step known as primary bone formation, these collagen fibers are mineralized, resulting in a rise in Ca concentration [224, 225]. The boxplot depicted in Figure 43 indicates an initial increase in calcium concentration between the 2-week and 6-week samples, followed by an almost constant level until 18 weeks. Taking the 24-week sample as a reference exhibiting the highest Ca content, approximately 80 % of the final Ca concentration could be observed at 6 weeks. Nevertheless, the observed increase between week 18 and week 24 remains unclear but might be attributed to the different mineralization sites regarding the collagen fiber, either intrafibrillar or extrafibrillar. During development, crystals may nucleate and grow within collagen fibrils before accumulating on extrafibrillar surfaces. It is known that the larger part of minerals is presented as extrafibrillar minerals, but the exact details of these stiffening time points are uncertain [19]. Mineralization patterns of healing bone tissues may differ considerably from those of healthy tissues. However, to examine these two processes concerning Ca concentration and its evolution over time, further investigations have to be made to be able to explain the rise between weeks 18 and 24.

Throughout life, changes in the chemical composition of bone tissue occur due to growth and remodeling processes. In this study, the Ca content increases with age, reaches a maximum at week 24, and decreases again at the end of the test period. At the healing front adjacent to the implant, it is plausible to speculate with a lower mineral concentration due to new bone formation and the lower maturation stage of the mineral particles, which could be confirmed (Figure 43). Magnesium has been reported to influence the HAp crystal size since the substitution with Ca is associated with crystal lattice distortion and hindrance of crystal growth, leading to poor mineralization [226]. A study by Serre et al. indicated reduced osteoblastic activity and, thus, an absence of calcification of the newly formed extracellular matrix [135]. Zhang et al. have illustrated that con-

tinuous elevated Mg^{2+} concentration influences mineralization by reducing collagen and calcium phosphate production. However, it is important to note that a proper Mg^{2+} ion concentration from Mg alloys is known to promote osteogenesis [227]. Further studies are required to elucidate the contradictory phenomena of Mg^{2+}. However, since the degradation rate is minimal in the case of a ZX00 implant and no excessive Mg concentration can be expected, there should be no negative effect on bone formation. To provide more reliable information, bone tissue at the position of the previously degraded implant has to be investigated after complete degradation to make a statement about the influence of the biodegradable implant and, thus, about the final bone quality.

As hypothesized, the local tissue modulus and hardness varied according to the tissue composition. The combination of nanoindentation and EDX measurements provides a way to correlate mechanical properties and mineral content in bone tissue. The results prove that structural differences in the biological material bone are reflected in the mechanical properties. Hardness was a reliable measure of the mineralization degree since it is predominantly determined by the inorganic mineral component, mainly composed of HAp, which contains Ca. Therefore, the progression of mineralization that accompanies bone maturation was reflected by an increase in hardness 44.

In the bone tissue until week 24, the mechanical properties tended to increase more rapidly than the mineral content, suggesting that other factors might also contribute to them. For more precise information, the whole bone-implant interface instead of the relatively small array could be investigated by means of nanoindentation experiments and EDX measurements since previous studies showed that the mineral platelet orientation, thickness, and size vary along the interface, which in turn strongly affect the mechanical properties of bone [228]. Additionally, it has been demonstrated that newly formed bone in the bone marrow region may be much more affected by locally elevated Mg levels due to implant degradation compared to areas in the corticalis [76]. For future investigations, a larger set of samples could be analyzed for a more accurate correlation between mechanical and compositional parameters and the effect of healing time and measuring position. Further experiments, such as SAXS measurements, could provide information on the extent to which the crystal size at the bone-implant interface has changed due to the degrading implant. In addition, Raman spectroscopy would provide a valuable tool to measure the mineral-to-matrix ratio, indicating the amount of mineralization at the bone-

implant interface [66]. However, this work revealed a lower Ca concentration due to the lower maturation stage but no adverse effect in terms of implant degradation. The results of this study provide valuable information about the mechanical properties and chemical composition and their relation concerning the implantation duration of a ZX00 implant. As there are no inconsistencies in the results, and they coincide with values found in the literature, it can be assumed that the fracture healing process and associated mechanical and chemical properties are not negatively affected by the degradation of a ZX00.

Limitations

This study is subjected to some limitations. Seven rats across five different age groups were used to investigate the influence of a degrading implant on mechanical properties and chemical composition with time. Age differences among animals result in significant weight variations, leading to varying forces acting on the implant. Thus, potential influences on the statistics of bone properties due to individual abnormalities and inherent tissue inhomogeneities cannot be disregarded. The relatively small number of test animals allows only a limited prediction. Future studies should include a larger number of animals per group and encompass more groups of various ages to statistically minimize individual differences and weight disparities among age categories.

Because growing animals were used in these experiments, a time-dependent change in both the mechanical properties and the chemical composition of the bone tissue is always present. This natural gradient in tissue properties and mineral content emerges from skeletal development. In rats, the majority of appositional growth occurs at the periosteal surface, leading to younger bone near the periosteum and older bone toward the interior of the cortex [66]. Hence, variations in the measured values could be a fact of localized differences in bone tissue age. Furthermore, adjusting the dimensions of the nanoindentation array to cover more bone tissue along the implant could be beneficial. Another limitation pertains to the sample preparation. As mentioned, the number of available samples was limited, and the samples were used for other experiments prior to nanoindentation tests. Considering the different experimental requirements, a compromise had to be made in terms of sample preparation. Consequently, only slices with a maximum thickness of 200 µm were deemed suitable. However, thicker slices should be preferred for improved and easier handling of the specimens. In certain instances, the

occurrence of implant breakout was unavoidable.

To gain insight into microscopic effects within the bone tissue that may not be discernible in microscopic images, histological analyses would be valuable. They would enable a more precise differentiation between tissue types like callus, fibrous, or bone tissue. Finding the appropriate measurement range can be challenging because the different types merge into each other. Therefore, employing histological staining could aid in identifying areas for nanoindentation measurements that are more informative.

Given the relatively substantial time span between 24 and 52 weeks in this study, any changes in mechanical properties during this period can only be hypothesized. Furthermore, making a statement about the impact of implant degradation on mechanical properties after complete degradation and regarding long-term effects is not feasible. Implants with the used dimension are expected to completely degrade after two years. Further investigations with an implantation period twice as long would be necessary to ascertain the fully restored tissue properties. However, one must remember that animal experiments are costly, especially for long-term studies. Therefore, each animal trial must be well planned to avoid unnecessary use of animals. Since the measured values of bone tissue at the implant and further away tend to approach with implantation time, it is reasonable to assume that the mechanical properties after complete degradation would correspond to those of a reference bone without an implant.

However, having in mind the variations across different species and considering the variability in size and shape of implants utilized in clinical practice, the results obtained from this animal study perhaps cannot be directly applied to potential applications in practical medicine. Further, the medical relevance of a bicortical implanted pin is limited compared to intramedullary nails or screws. Bone regeneration occurs only in a narrow area around the implant during the study period due to the moderate degradation of the ZX00 alloy. Ideally, implants with a smaller diameter could be chosen for subsequent trials. This would provide a larger measurement area within the same timeframe and potentially shorten the study period as the implant would fully degrade.

7 Conclusion

Biodegradable implants present an interesting and promising alternative to permanent implants in orthopedics. Their advantage lies in their complete degradation within the body, thereby eliminating the need for a second surgery for implant removal, which minimizes the general associated risk and costs in the healthcare system. Studies indicated that implantation of Mg alloys into bone positively influences bone healing and promotes new bone tissue formation. Nonetheless, the fast degradation behavior and the related hydrogen gas formation have limited the application of Mg implants in clinics. Various Mg alloys have been developed to adjust the desired properties. ZX00 is a Mg-Zn-Ca alloy with a low amount of alloying elements based on materials naturally occurring in the human body. The present study aimed to investigate the effect of implant degradation on bone tissue. The main focus was on assessing the influence in terms of stiffness, hardness, and the associated alterations in chemical composition close to the implant. This was accomplished through nanoindentation experiments, as it is an appropriate way to obtain information on the mechanical properties of bone around an implant. Combined with EDX measurements, variations in the chemical composition due to pin degradation could be evaluated. Moreover, visual methods were applied to evaluate bone formation, osteoinduction, and degradation behavior. The study revealed natural variations in mechanical properties and chemical composition based on healing time in newly formed and bulk bone. Further, it was able to correlate these mechanical and chemical properties. In summary, the study yielded the following results:

- Increase of Young's modulus and hardness as a function of healing time and distance from the implant.
- Approximation of the mechanical properties at the implant to the original ones within 24 weeks.
- Increase of Ca concentration as a result of skeletal maturation.
- Correlation between chemical composition and both Young's modulus and hardness.
- No negative impact on bone healing and formation due to implant degradation.

In conclusion, regarding the obtained results, it is evident that fracture healing and bone formation remain unaffected by a ZX00 alloy. The degrading material did not negatively influence the mechanical properties and the chemical composition. It can be assumed that the original condition can be restored after complete degradation. Therefore, ZX00 implants hold immense promise for successful clinical applications in orthopedics and traumatology.

Bibliography

[1] Die Bundesarbeitsgemeinschaft Mehr Sicherheit für Kinder e. V. Trend der Krankenhausfälle 2002–2012. `https://www.kindersicherheit.de/fachinformationen/unfallstatistiken.html`, n.d. Accessed: 2022 Jan.

[2] M. Donabauer. KFV Unfallstatistik 2019. `https://www.kfv.at/forschung/sport-und-freizeitsicherheit/fachpublikationen/`, 2019. Accessed: 2022 Jan.

[3] J. Schalamon, S. Dampf, G. Singer, et al. Evaluation of fractures in children and adolescents in a Level i Trauma Center in Austria. *J. Trauma Acute Care Surg.*, 71(2):E19–E25, 2011.

[4] M. Niinomi. Recent metallic materials for biomedical applications. *Metall. Mater. Trans. A: Phys. Metall. Mater. Sci.*, 33(3):477–486, 2002.

[5] B. T. Clement. Frakturstabilisierung mittels resorbierbaren Magnesium-basierten Schrauben im wachsenden Großtiermodell. Master's thesis, Medizinische Universität Graz, 2019.

[6] V. K. Ganesh, K. Ramakrishna, and D. N. Ghista. Biomechanics of bone-fracture fixation by stiffness-graded plates in comparison with stainless-steel plates. *Biomed. Eng. Online*, 4(46), 2005.

[7] Y. Chen, Z. Xu, C. Smith, and J. Sankar. Recent advances on the development of magnesium alloys for biodegradable implants. *Acta Biomater.*, 10(11):4561–4573, 2014.

[8] R. B. Kahla and A. Barkaoui. Bone multiscale mechanics. In *Bone remodeling process: Mechanics, biology, and numerical modeling*, chapter 1, pages 1–47. Academic Press, London, UK, 2021.

[9] J. Streicher and M. L. Pretterklieber. Bewegungsapparat. In F. Anderhuber, F. Pera, and J. Streicher, editors, *Waldeyer - Anatomie des Menschen*, chapter 4, pages 95–425. De Gruyter, Berlin, DE, 19th edition, 2012.

[10] D. H. Copp and S. S. Shim. The homeostatic function of bone as a mineral reservoir. *Oral Surg. Oral Med. Oral Pathol. Oral Radiol.*, 16(6):738–744, 1963.

[11] A. L. Boskey. Mineralization, structure and function of bone. In M. J. Seibel, S. P. Robins, and J. P. Bilezikian, editors, *Dynamics of bone and cartilage metabolism*, chapter 12, pages 201–212. Academic Press, San Diego, California, 2nd edition, 2006.

[12] G. J. Tortora and B. Derrickson. The skeletal system: Bone tissue. In *Principles of anatomy and physiology*, chapter 6, pages 171–193. John Wiley and Sons, Hoboken, NJ, 15th edition, 2017.

[13] J. Wolff. *Das Gesetz der Transformation der Knochen*. Hirschwald, Berlin, DE, 1892.

[14] F. A. Schulte, F. M. Lambers, G. Kuhn, and R. Müller. In vivo micro-computed tomography allows direct three-dimensional quantification of both bone formation and bone resorption parameters using time-lapsed imaging. *Bone*, 48(3):433–442, 2011.

[15] R. Ruimerman, P. Hilbers, B. van Rietbergen, and R. Huiskes. A theoretical framework for strain-related trabecular bone maintenance and adaptation. *J. Biomech.*, 38(4):931–941, 2005.

[16] E. E. Wilson, A. Awonusi, M. D. Morris, et al. Three structural roles for water in bone observed by solid-state NMR. *Biophys. J.*, 90(10):3722–3731, 2006.

[17] N. Little, B. Rogers, and M. Flannery. Bone formation, remodelling and healing. *Surgery*, 29(4):141–145, 2011.

[18] X. Lin, S. Patil, Y.-G. Gao, and A. Qian. The bone extracellular matrix in bone formation and regeneration. *Front. Pharmacol.*, 11:757, 2020.

[19] B. M. Oosterlaken, M. P. Vena, and G. de With. In vitro mineralization of collagen. *Adv. Mater.*, 33(16):2004418, 2021.

[20] F. Mottaghitalab, H. Hosseinkhani, M. A. Shokrgozar, et al. Silk as a potential candidate for bone tissue engineering. *J. Control. Release*, 215:112–128, 2015.

[21] X. Feng. Chemical and biochemical basis of cell-bone matrix interaction in health and disease. *Curr. Chem. Biol.*, 3(2):189–196, 2009.

[22] A. L. Boskey. Bone composition: Relationship to bone fragility and antiosteoporotic drug effects. *Bonekey Rep.*, 2(447):1–11, 2013.

[23] R. Lüllmann-Rauch and E. Asan. Binde- und Stützgewebe. In *Taschenlehrbuch Histologie*, chapter 8, pages 147–210. Georg Thieme Verlag, Stuttgart, DE, 6th edition, 2019.

[24] S. Weiner and H. D. Wagner. The material bone: Structure-mechanical function relations. *Annu. Rev. Mater. Res.*, 28(1):271–298, 2003.

[25] A. Barkaoui, A. Chamekh, T. Merzouki, et al. Multiscale approach including microfibril scale to assess elastic constants of cortical bone based on neural network computation and homogenization method. *Int. J. Numer. Methods Biomed. Eng.*, 30(3):318–338, 2014.

[26] E. Hamed, Y. Lee, and I. Jasiuk. Multiscale modeling of elastic properties of cortical bone. *Acta Mech.*, 213:131–154, 2010.

[27] D. P. Bhattarai, L. E. Aguilar, C. H. Park, and C. S. Kim. A review on properties of natural and synthetic based electrospun fibrous materials for bone tissue engineering. *Membranes*, 8(3):62, 2018.

[28] U. G. K. Wegst, H. Bai, E. Saiz, et al. Bioinspired structural materials. *Nat. Mater.*, 14(1):23–36, 2015.

[29] E. N. Marieb and K. Hoehn. Bones and skeletal tissues. In *Human anatomy & physiology*, chapter 6, pages 173–198. Pearson Education, Hoboken, NJ, 11th edition, 2019.

[30] D. P. Fyhrie and J. H. Kimura. Cancellous bone biomechanics. *J. Biomech.*, 32(11):1139–1148, 1999.

[31] W. Suchanek and M. Yoshimura. Processing and properties of hydroxyapatite-based biomaterials for use as hard tissue replacement implants. *J. Mater. Res.*, 13(1):94–117, 1998.

[32] E. B. W. Giesen, M. Ding, M. Dalstra, and T. M. G. J. van Eijden. Changed morphology and mechanical properties of cancellous bone in the mandibular condyles of edentate people. *J. Dent. Res.*, 83(3):255–259, 2004.

[33] G. A. P. Renders, L. Mulder, L. J. van Ruijven, and T. M. G. J. van Eijden. Porosity of human mandibular condylar bone. *J. Anat.*, 210(3):239–248, 2007.

[34] S. Wu, X. Liu, K. W. K. Yeung, et al. Biomimetic porous scaffolds for bone tissue engineering. *Mater. Sci. Eng. R Rep.*, 80:1–36, 2014.

[35] Y.-C. Fung. Bone and cartilage. In *Biomechanics: Mechanical properties of living tissues*, chapter 12, pages 500–544. Springer, New York, NY, 2nd edition, 1993.

[36] V. I. Sikavitsas, J. S. Temenoff, and A. G. Mikos. Biomaterials and bone mechanotransduction. *Biomaterials*, 22(19):2581–2593, 2001.

[37] A. T. M. Phillips. Structural optimisation: Biomechanics of the femur. *Proc. Inst. Civ. Eng.: Eng. Comput. Mech.*, 165(2):147–154, 2012.

[38] H. M. Britz, C. D. L. Thomas, J. G. Clement, and D. M. L. Cooper. The relation of femoral osteon geometry to age, sex, height and weight. *Bone*, 45(1):77–83, 2009.

[39] P. Fratzl and R. Weinkamer. Hierarchical structure and repair of bone: Deformation, remodelling, healing. In S. van der Zwaag, editor, *Self healing materials: An alternative approach to 20 centuries of materials science*, pages 323–335. Springer, Dordrecht, NL, 1st edition, 2007.

[40] M. M. Giraud-Guille. Twisted plywood architecture of collagen fibrils in human compact bone osteons. *Calcif. Tissue Int.*, 42(3):167–180, 1988.

[41] S. Weiner, W. Traub, and H. D. Wagner. Lamellar bone: Structure-function relations. *J. Struct. Biol.*, 126(3):241–255, 1999.

[42] W. Wagermaier, H. S. Gupta, A. Gourrier, et al. Spiral twisting of fiber orientation inside bone lamellae. *Biointerphases*, 1(1):1–5, 2006.

[43] S. M. Siadat, A. A. Silverman, C. A. DiMarzio, and J. W. Ruberti. Measuring collagen fibril diameter with differential interference contrast microscopy. *J. Struct. Biol.*, 213(1):1–8, 2021.

[44] P. J. Thurner. Atomic force microscopy and indentation force measurement of bone. *Wiley Interdiscip. Rev. Nanomed. Nanobiotechnol*, 1(6):624–649, 2009.

[45] J.-Y. Rho, L. Kuhn, and P. Zioupos. Mechanical properties and the hierarchical structure of bone. *Med. Eng. Phys.*, 20(2):9102, 1998.

[46] J. Hardin and G. Bertoni. Beyond the cell: Cell adhesions, cell junctions, and extracellular structures. In *Becker's world of the cell*, chapter 15, pages 429–454. Pearson, Harlow, UK, 9th edition, 2018.

[47] J. Parvizi. Collagen. In J. Parvizi and G. K. Kim, editors, *High yield orthopaedics*, chapter 53, pages 107–109. Saunders Elsevier, Philadelphia, PA, 2010.

[48] W. J. Landis and F. H. Silver. The structure and function of normally mineralizing avian tendons. *Comp. Biochem. Physiol. A Mol. Integr. Physiol.*, 133(4):1135–1157, 2002.

[49] H. Boedtker and P. Doty. The native and denatured states of soluble collagen. *J. Am. Chem. Soc.*, 78(17):4267–4280, 1956.

[50] M. J. Glimcher. Bone: Nature of the calcium phosphate crystals and cellular, structural, and physical chemical mechanisms in their formation. *Rev. Mineral Geochem.*, 64(1):223–282, 2006.

[51] P. Fratzl, H. S. Gupta, E. P. Paschalis, and P. Roschger. Structure and mechanical quality of the collagen–mineral nano-composite in bone. *J. Mater. Chem.*, 14(14):2115–2123, 2004.

[52] R. M. Hoerth, B. M. Seidt, M. Shah, et al. Mechanical and structural properties of bone in non-critical and critical healing in rat. *Acta Biomater.*, 10(9):4009–4019, 2014.

[53] F. F. Safadi, M. F. Barbe, S. M. Abdelmagid, et al. Bone structure, development and bone biology. In J. S. Khurana, editor, *Bone pathology*, chapter 1, pages 1–50. Humana Press, New York, NY, 2nd edition, 2009.

[54] X. Feng and J. M. McDonald. Disorders of bone remodeling. *Annu. Rev. Pathol.*, 6:121–145, 2011.

[55] B. Gueorguiev-Rüegg and M. Stoddart. Biology and biomechanics in bone healing. In R. E. Buckley, C. G. Moran, and T. Apivatthakakul, editors, *AO principles of fracture management*, volume 1, chapter 1.2, pages 9–26. Thieme, Stuttgart, DE, 3rd edition, 2018.

[56] P. J. Wraighte and B. E. Scammell. Principles of fracture healing. *Surgery*, 24(6):198–207, 2006.

[57] P. V. Giannoudis, T. A. Einhorn, and D. Marsh. Fracture healing: The diamond concept. *Injury*, 38:3–6, 2007.

[58] F. U. Niethard, J. Pfeil, and P. Biberthaler. Grundlagen der Unfallchirurgie. In *Duale Reihe Orthopädie und Unfallchirurgie*, chapter 10, pages 292–356. Thieme, Stuttgart, DE, 8th edition, 2017.

[59] J. Li, M. A. Kacena, and D. L. Stocum. Fracture healing. In D. B. Burr and M. R. Allen, editors, *Basic and applied bone biology*, chapter 12, pages 235–253. Academic Press, London, UK, 2nd edition, 2019.

[60] M. S. Ghiasi, J. E. Chen, E. K. Rodriguez, et al. Computational modeling of human bone fracture healing affected by different conditions of initial healing stage. *BMC Musculoskelet. Disord.*, 20(1):562, 2019.

[61] T. Kim, C. W. See, X. Li, and D. Zhu. Orthopedic implants and devices for bone fractures and defects: Past, present and perspective. *ER*, 1:6–18, 2020.

[62] W. J. Landis, M. Song, A. Leith, et al. Mineral and organic matrix interaction in normally calcifying tendon visualized in three dimensions by high-voltage electron microscopic tomography and graphic image reconstruction. *J. Struct. Biol.*, 110(1):39–54, 1993.

[63] K. Nawrot-Wawrzyniak, F. Varga, A. Nader, et al. Effects of tumor-induced osteomalacia on the bone mineralization process. *Calcif. Tissue Int.*, 84(4):313–323, 2009.

[64] P. Roschger, E. Paschalis, P. Fratzl, and K. Klaushofer. Bone mineralization density distribution in health and disease. *Bone*, 42(3):456–466, 2008.

[65] G. Lewis and J. S. Nyman. The use of nanoindentation for characterizing the properties of mineralized hard tissues: State-of-the art review. *J. Biomed. Mater. Res. Part B Appl. Biomater.*, 87B(1):286–301, 2008.

[66] E. Donnelly, A. L. Boskey, S. P. Baker, and M. C. H. van der Meulen. Effects of tissue age on bone tissue material composition and nanomechanical properties in the rat cortex. *J. Biomed. Mater. Res. A*, 92A(3):1048–1056, 2010.

[67] P. K. Zysset, X. E. Guo, C. E. Hoffler, et al. Elastic modulus and hardness of cortical and trabecular bone lamellae measured by nanoindentation in the human femur. *J. Biomech.*, 32(10):1005–1012, 1999.

[68] J.-Y. Rho, T. Y. Tsui, and G. M. Pharr. Elastic properties of human cortical and trabecular lamellar bone measured by nanoindentation. *Biomaterials*, 18(20):1325–1330, 1997.

[69] H. Isaksson, S. Nagao, M. Kempa, et al. Precision of nanoindentation protocols for measurement of viscoelasticity in cortical and trabecular bone. *J. Biomech.*, 43(12):2410–2417, 2010.

[70] D. A. Chakkalakal, J. R. Novak, E. D. Fritz, et al. Inhibition of bone repair in a rat model for chronic and excessive alcohol consumption. *Alcohol*, 36(3):201–214, 2005.

[71] L. Karim, A. Kwaczala, D. Vashishth, and S. Judex. Dose-dependent effects of pharmaceutical treatments on bone matrix properties in ovariectomized rats. *Bone Rep.*, 15:101137, 2021.

[72] N. G. Sommer, D. Hirzberger, L. Paar, et al. Implant degradation of low-alloyed Mg–Zn–Ca in osteoporotic, old and juvenile rats. *Acta Biomater.*, 147:427–438, 2022.

[73] F. A. Shah, A. Stoica, C. Cardemil, and A. Palmquist. Multiscale characterization of cortical bone composition, microstructure, and nanomechanical properties in experimentally induced osteoporosis. *J. Biomed. Mater. Res. A*, 106(4):997–1007, 2018.

[74] R. Ozasa, T. Ishimoto, S. Miyabe, et al. Osteoporosis changes collagen/apatite orientation and Young's modulus in vertebral cortical bone of rat. *Calcif. Tissue Int.*, 104(4):449–460, 2019.

[75] P. P. Lelovas, T. T. Xanthos, S. E. Thoma, et al. The laboratory rat as an animal model for osteoporosis research. *Comp. Med.*, 58(5):424–430, 2008.

[76] T. A. Grünewald, H. Rennhofer, B. Hesse, et al. Magnesium from bioresorbable implants: Distribution and impact on the nano- and mineral structure of bone. *Biomaterials*, 76:250–260, 2016.

[77] N. G. Grün, P. Holweg, S. Tangl, et al. Comparison of a resorbable magnesium implant in small and large growing-animal models. *Acta Biomater.*, 78:378–386, 2018.

[78] T. Kraus, S. Fischerauer, S. Treichler, et al. The influence of biodegradable magnesium implants on the growth plate. *Acta Biomater.*, 66:109–117, 2018.

[79] R. L. Maynard and N. Downes. Introduction to the skeleton: Bone, cartilage and joints. In *Anatomy and histology of the laboratory rat in toxicology and biomedical research*, chapter 3, pages 11–22. Academic Press, London, UK, 2019.

[80] M. Vanleene, C. Rey, and M.-C. Ho Ba Tho. Relationships between density and Young's modulus with microporosity and physico-chemical properties of wistar rat cortical bone from growth to senescence. *Med. Eng. Phys.*, 30(8):1049–1056, 2008.

[81] J. Y. Rho, P. Zioupos, J. D. Currey, and G. M. Pharr. Variations in the individual thick lamellar properties within osteons by nanoindentation. *Bone*, 25(3):295–300, 1999.

[82] J. Krämer and J. Grifka. Behandlungsmethoden. In *Orthopädie Unfallchirurgie*, chapter 3, pages 59–82. Springer, Heidelberg, DE, 8th edition, 2007.

[83] D. F. Williams. On the mechanisms of biocompatibility. *Biomaterials*, 29(20):2941–2953, 2008.

[84] H. Rössler and W. Rüther. *Orthopädie und Unfallchirurgie*. Elsevier, München, DE, 19th edition, 2005.

[85] G. Reith, V. Schmitz-Greven, K. O. Hensel, et al. Metal implant removal: Benefits and drawbacks - a patient survey. *BMC Surg.*, 15(1):1–8, 2015.

[86] M. Haseeb, M. F. Butt, T. Altaf, et al. Indications of implant removal: A study of 83 cases. *Int. J. Health Sci.*, 11(1):1–7, 2017.

[87] C. Liu, Y. Xin, G. Tang, and P. K. Chu. Influence of heat treatment on degradation behavior of bio-degradable die-cast AZ63 magnesium alloy in simulated body fluid. *Mater. Sci. Eng. A*, 456(1–2):350–357, 2007.

[88] R. I. M. Asri, W. S. W. Harun, M. Samykano, et al. Corrosion and surface modification on biocompatible metals: A review. *Mater. Sci. Eng. C.*, 77:1261–1274, 2017.

[89] P. Tian and X. Liu. Surface modification of biodegradable magnesium and its alloys for biomedical applications. *Regen. Biomater.*, 2(2):135–151, 2015.

[90] N. Coen, M. A. Kadhim, E. G. Wright, et al. Particulate debris from a titanium metal prosthesis induces genomic instability in primary human fibroblast cells. *Br. J. Cancer*, 88(4):548–552, 2003.

[91] C. Vermes, T. T. Glant, N. J. Hallab, et al. The potential role of the osteoblast in the development of periprosthetic osteolysis: review of in vitro osteoblast responses to wear debris, corrosion products, and cytokines and growth factors. *J. Arthroplasty*, 16(8):95–100, 2001.

[92] M. P. Staiger, A. M. Pietak, J. Huadmai, and G. Dias. Magnesium and its alloys as orthopedic biomaterials: A review. *Biomaterials*, 27(9):1728–1734, 2006.

[93] Y. Okazaki and E. Gotoh. Metal release from stainless steel, Co–Cr–Mo–Ni–Fe and Ni–Ti alloys in vascular implants. *Corros. Sci.*, 50(12):3429–3438, 2008.

[94] M. Salahshoor and Y. Guo. Biodegradable orthopedic magnesium-calcium (MgCa) alloys, processing, and corrosion performance. *Materials*, 5(1):135–155, 2012.

[95] J. Nagels, M. Stokdijk, and P. M. Rozing. Stress shielding and bone resorption in shoulder arthroplasty. *J. Shoulder Elb. Surg.*, 12(1):35–39, 2003.

[96] C. A. Engh, J. D. Bobyn, and A. H. Glassman. Porous-coated hip replacement. The factors govering bone ingrowth, stress shielding, and clinical results. *J. Bone Jt. Surg.*, 69(1):45–55, 1987.

[97] M. Niinomi and M. Nakai. Titanium-based biomaterials for preventing stress shielding between implant devices and bone. *Int. J. Biomater.*, 2011:1–10, 2011.

[98] R. Huiskes, H. Weinans, and B. van Rietbergen. The relationship between stress shielding and bone resorption around total hip stems and the effects of flexible materials. *Clin. Orthop. Relat. Res.*, pages 124–134, 1992.

[99] H. Hermawan. Biodegradable metals: State of the art. In *Biodegradable metals: From concept to applications*, chapter 2, pages 13–22. Springer, Heidelberg, DE, 1st edition, 2012.

[100] V. Tsakiris, C. Tardei, and F. M. Clicinschi. Biodegradable Mg alloys for orthopedic implants – A review. *J. Magnes. Alloy.*, 9(6):1884–1905, 2021.

[101] F. Witte, N. Hort, F. Feyerabend, and C. Vogt. Magnesium (Mg) corrosion: A challenging concept for degradable implants. In G.-L. Song, editor, *Corrosion of magnesium alloys*, chapter 10, pages 403–425. Woodhead Publishing, Oxford, UK, 2011.

[102] N. G. Grün, N. Donohue, P. Holweg, and A.-M. Weinberg. Resorbierbare Implantate in der Unfallchirurgie. *J. Miner. Stoffwechs. Muskuloskelet. Erkrank.*, 25(3):82–89, 2018.

[103] H. Haferkamp, V. Kaese, M. Niemeyer, et al. Untersuchungen an magnesium-basierten Legierungen als neue Materialien in der Implantologie. *Mater. Werkst.*, 32:116–120, 2001.

[104] D. Shekhawat, A. Singh, M. K. Banerjee, et al. Bioceramic composites for orthopaedic applications: A comprehensive review of mechanical, biological, and microstructural properties. *Ceram. Int.*, 47(3):3013–3030, 2021.

[105] P. Layrolle and G. Daculsi. Physicochemistry of apatite and its related calcium phosphates. In B. León and J. A. Jansen, editors, *Thin calcium phosphate coatings for medical implants*, chapter 2, pages 9–24. Springer, New York, NY, 1st edition, 2009.

[106] T. Kraus, F. Moszner, S. Fischerauer, et al. Biodegradable Fe-based alloys for use in osteosynthesis: Outcome of an in vivo study after 52 weeks. *Acta Biomater.*, 10(7):3346–3353, 2014.

[107] M. Peuster, C. Hesse, T. Schloo, et al. Long-term biocompatibility of a corrodible peripheral iron stent in the porcine descending aorta. *Biomaterials*, 27(28):4955–4962, 2006.

[108] G. Poologasundarampillai and A. Nommeots-Nomm. Materials for 3D printing in medicine: Metals, polymers, ceramics, hydrogels. In D. M. Kalaskar, editor, *3D printing in medicine*, chapter 3, pages 43–71. Woodhead Publishing, Duxford, UK, 2017.

[109] M. Pogorielov, E. Husak, A. Solodivnik, and S. Zhdanov. Magnesium-based biodegradable alloys: Degradation, application, and alloying elements. *Interv. Med. Appl. Sci.*, 9(1):27–38, 2017.

[110] C. Kammer. Anwendung. In *Magnesium Taschenbuch*, chapter 16, pages 651–677. Aluminium-Verlag, Düsseldorf, DE, 1st edition, 2000.

[111] L. Wu, F. Feyerabend, A. F. Schilling, et al. Effects of extracellular magnesium extract on the proliferation and differentiation of human osteoblasts and osteoclasts in coculture. *Acta Biomater.*, 27:294–304, 2015.

[112] M. A. Rauschmann, D. Thomann, and L. Zichner. *Geschichte operativer Verfahren an den Bewegungsorganen*, volume 2. Steinkopff, Darmstast, DE, 1st edition, 2000.

[113] A. Lambotte. L'utilisation du magnesium comme materiel perdu dans l'osteosynthèse. *Bull. Mém. Soc. Nat. Cir.*, 28(3):1325–1334, 1932.

[114] C. Castellani, R. A. Lindtner, P. Hausbrandt, et al. Bone-implant interface strength and osseointegration: Biodegradable magnesium alloy versus standard titanium control. *Acta Biomater.*, 7(1):432–440, 2011.

[115] J. T. Black and R. A. Kohser. Nonferrous metals and alloys. In *DeGarmo's materials and processes in manufacturing*, chapter 8, pages 182–207. John Wiley and Sons, Hoboken, NJ, 11th edition, 2012.

[116] C. Kammer. Eigenschaften von reinem Magnesium. In *Magnesium Taschenbuch*, chapter 4, pages 77–97. Aluminium-Verlag, Düsseldorf, DE, 1st edition, 2000.

[117] L. J. Gibson and M. F. Ashby. Material properties. In *Cellular solids: Structure and properties*, chapter 3, pages 52–92. Cambridge University Press, Cambridge, UK, 2nd edition, 1997.

[118] S. Sahoo, R. Sabat, S. Panda, et al. Mechanical property of pure magnesium: From orientation perspective pertaining to deviation from basal orientation. *J. Mater. Eng. Perform.*, 24(6):2346–2353, 2015.

[119] F. Witte, N. Hort, C. Vogt, et al. Degradable biomaterials based on magnesium corrosion. *Curr. Opin. Solid State Mater. Sci.*, 12(5-6):63–72, 2008.

[120] M. Cuppone, B. B. Seedhom, E. Berry, and A. E. Ostell. The longitudinal Young's modulus of cortical bone in the midshaft of human femur and its correlation with CT scanning data. *Calcif. Tissue Int.*, 74(3):302–309, 2004.

[121] Y.-S. Lai, W.-C. Chen, C.-H. Huang, et al. The effect of graft strength on knee laxity and graft in-situ forces after posterior cruciate ligament reconstruction. *PLoS One*, 10(5), 2015.

[122] M. Peron, F. Berto, and J. Torgersen. Challenges and common strategies. In *Magnesium and its alloys as implant materials: Corrosion, mechanical and biological performances*, chapter 1, pages 1–9. CRC Press, Boca Raton, FL, 1st edition, 2020.

[123] U. Gröber, J. Schmidt, and K. Kisters. Magnesium in prevention and therapy. *Nutrients*, 7(9):8199–8226, 2015.

[124] A. M. Al Alawi, S. W. Majoni, and H. Falhammar. Magnesium and human health: Perspectives and research directions. *Int. J. Endocrinol.*, 2018:1–17, 2018.

[125] A. C. Ross, B. Caballero, R. J. Cousins, et al. *Modern nutrition in health and disease*. Wolters Kluwer Health/Lippincott Williams and Wilkins, Philadelphia, PA, 11th edition, 2014.

[126] S. Schaal, K. Kunsch, and S. Kunsch. *Der Mensch in Zahlen: Eine Datensammlung in Tabellen mit über 20000 Einzelwerten*. Springer, Heidelberg, DE, 4th edition, 2016.

[127] E. Koç, M. B. Kannan, M. Ünal, and E. Candan. Influence of zinc on the microstructure, mechanical properties and in vitro corrosion behavior of magnesium–zinc binary alloys. *J. Alloys Compd.*, 648:291–296, 2015.

[128] P. Möhnle and A. E. Goetz. Physiologische Effekte, Pharmakologie und Indikationen zur Gabe von Magnesium. *Anaesthesist*, 50:377–391, 2001.

[129] J. M. Seitz, R. Eifler, F. W. Bach, and H. J. Maier. Magnesium degradation products: Effects on tissue and human metabolism. *J. Biomed. Mater. Res. A*, 102(10):3744–3753, 2014.

[130] A. Hartwig. Role of magnesium in genomic stability. *Mutat. Res.*, 475(1-2):113–121, 2001.

[131] J. Zhang, C. Xu, Y. Jing, et al. New horizon for high performance Mg-based biomaterial with uniform degradation behavior: Formation of stacking faults. *Sci. Rep.*, 5(1):1–16, 2015.

[132] H. Zhou, B. Liang, H. Jiang, et al. Magnesium-based biomaterials as emerging agents for bone repair and regeneration: From mechanism to application. *J. Magnes. Alloy.*, 9(3):779–804, 2021.

[133] C. Liu, X. Fu, H. Pan, et al. Biodegradable Mg-Cu alloys with enhanced osteogenesis, angiogenesis, and long-lasting antibacterial effects. *Sci. Rep.*, 6(27374):1–17, 2016.

[134] G. Anders. Die Wirkung von Magnesium auf kalzergische Reaktionen und auf den Knochen. *Magnesium-Bulletin*, 8:5–42, 1986.

[135] C. M. Serre, M. Papillard, P. Chavassieux, et al. Influence of magnesium substitution on a collagen-apatite biomaterial on the production of a calcifying matrix by human osteoblasts. *J. Biomed. Mater. Res.*, 42(4):626–633, 1998.

[136] H. Zreiqat, C. R. Howlett, A. Zannettino, et al. Mechanisms of magnesium-stimulated adhesion of osteoblastic cells to commonly used orthopaedic implants. *J. Biomed. Mater. Res.*, 62(2):175–184, 2002.

[137] I. V. Antoniac and D. Lăptoiu. Magnesium alloys - current orthopedic applications. *Revista de Ortopedie si Traumatologie*, 4(20):1–10, 2010.

[138] G. Song and S. Song. A possible biodegradable magnesium implant material. *Adv. Eng. Mater.*, 9(4):298–302, 2007.

[139] Y. Song, D. Shan, R. Chen, et al. Biodegradable behaviors of AZ31 magnesium alloy in simulated body fluid. *Mater. Sci. Eng. C*, 29(3):1039–1045, 2009.

[140] S. Schrenk. *Abbauverhalten degradierbarer Magnesiumlegierungen in körperähnlichen Elektrolyten*. Doctoral dissertation, Friedrich-Alexander-Universität Erlangen-Nürnberg, 2011.

[141] N. T. Tran, Y.-K. Kim, S.-Y. Kim, et al. Comparative osteogenesis and degradation behavior of magnesium implant in epiphysis and diaphysis of the long bone in the rat model. *Materials*, 15(16):5630, 2022.

[142] G. Neroth. Korrosion der Metalle. In G. Neroth and D. Vollenschaar, editors, *Wendehorst Baustoffkunde: Grundlagen - Baustoffe - Oberflächenschutz*, chapter 12, pages 735–749. Vieweg + Teubner Verlag, Wiesbaden, DE, 27th edition, 2011.

[143] X.-N. Gu and Y.-F. Zheng. A review on magnesium alloys as biodegradable materials. *Front. Mater. Sci.*, 4(2):111–115, 2010.

[144] G. E. J. Poinern, S. Brundavanam, and D. Fawcett. Biomedical magnesium alloys: A review of material properties, surface modifications and potential as a biodegradable orthopaedic implant. *Am. J. Biomed. Eng.*, 2(6):218–240, 2012.

[145] M. Pourbaix. *Atlas of electrochemical equilibria in aqueous solutions*. NACE International, Houston, TX, 2nd edition, 1974.

[146] G. L. Makar and J. Kruger. Corrosion of magnesium. *Int. Mater. Rev.*, 38(3):138–153, 1993.

[147] N. T. Kirkland and N. Birbilis. *Magnesium biomaterials: Design, testing, and best practice*. Springer, Heidelberg, DE, 1st edition, 2014.

[148] S. Virtanen. Biodegradable Mg and Mg alloys: Corrosion and biocompatibility. *Mater. Sci. Eng. B: Solid-State Mater. Adv. Technol.*, 176(20):1600–1608, 2011.

[149] G. Song. Control of biodegradation of biocompatable magnesium alloys. *Corros. Sci.*, 49(4):1696–1701, 2007.

[150] T. Kraus, S. F. Fischerauer, A. C. Hänzi, et al. Magnesium alloys for temporary implants in osteosynthesis: In vivo studies of their degradation and interaction with bone. *Acta Biomater.*, 8(3):1230–1238, 2012.

[151] D. Noviana, D. Paramitha, M. F. Ulum, and H. Hermawan. The effect of hydrogen gas evolution of magnesium implant on the postimplantation mortality of rats. *J. Orthop. Translat.*, 5:9–15, 2016.

[152] W. D. Müller, M. L. Nascimento, M. Zeddies, et al. Magnesium and its alloys as degradable biomaterials: Corrosion studies using potentiodynamic and EIS electrochemical techniques. *Mater. Res.*, 10(1):5–10, 2007.

[153] R. Ambat, N. N. Aung, and W. Zhou. Studies on the influence of chloride ion and pH on the corrosion and electrochemical behaviour of AZ91D magnesium alloy. *J. Appl. Electrochem.*, 30(7):865–874, 2000.

[154] J. Hofstetter, E. Martinelli, S. Pogatscher, et al. Influence of trace impurities on the in vitro and in vivo degradation of biodegradable Mg-5Zn-0.3Ca alloys. *Acta Biomater.*, 23:347–353, 2015.

[155] L. Yang and E. Zhang. Biocorrosion behavior of magnesium alloy in different simulated fluids for biomedical application. *Mater. Sci. Eng. C* ., 29(5):1691–1696, 2009.

[156] W. F. Ng, K. Y. Chiu, and F. T. Cheng. Effect of pH on the in vitro corrosion rate of magnesium degradable implant material. *Mater. Sci. Eng. C*, 30(6):898–903, 2010.

[157] F. Witte, J. Fischer, J. Nellesen, et al. In vitro and in vivo corrosion measurements of magnesium alloys. *Biomaterials*, 27(7):1013–1018, 2006.

[158] N. T. Kirkland, N. Birbilis, and M. P. Staiger. Assessing the corrosion of biodegradable magnesium implants: A critical review of current methodologies and their limitations. *Acta Biomater.*, 8(3):925–936, 2012.

[159] A. H. M. Sanchez, B. J. C. Luthringer, F. Feyerabend, and R. Willumeit. Mg and Mg alloys: How comparable are in vitro and in vivo corrosion rates? A review. *Acta Biomater.*, 13:16–31, 2015.

[160] P. Gunde, A. C. Hänzi, A. S. Sologubenko, and P. J. Uggowitzer. High-strength magnesium alloys for degradable implant applications. *Mater. Sci. Eng. A*, 528(3):1047–1054, 2011.

[161] D. Persaud-Sharma and A. McGoron. Biodegradable magnesium alloys: A review of material development and applications. *J. Biomim. Biomater. Biomed. Eng.*, 12:25–39, 2012.

[162] J. Z. Ilich and J. E. Kerstetter. Nutrition in bone health revisited: A story beyond calcium. *J. Am. Coll. Nutr.*, 19(6):715–737, 2000.

[163] J. Hofstetter, M. Becker, E. Martinelli, et al. High-strength low-alloy (HSLA) Mg–Zn–Ca alloys with excellent biodegradation performance. *JOM*, 66(4):566–572, 2014.

[164] B. Zhang, Y. Hou, X. Wang, et al. Mechanical properties, degradation performance and cytotoxicity of Mg–Zn–Ca biomedical alloys with different compositions. *Mater. Sci. Eng. C* ., 31(8):1667–1673, 2011.

[165] E. Zhang and L. Yang. Microstructure, mechanical properties and bio-corrosion properties of Mg–Zn–Mn–Ca alloy for biomedical application. *Mater. Sci. Eng. A*, 497(1-2):111–118, 2008.

[166] E. O. Hall. The deformation and ageing of mild steel: Iii discussion of results. *Proc. Phys. Soc. B*, 64(9):747, 1951.

[167] N. J. Petch. The cleavage strength of polycrystals. *J. Iron Steel Inst.*, 174(1):25–28, 1953.

[168] D. H. StJohn, M. Qian, M. A. Easton, et al. Grain refinement of magnesium alloys. *Metall Mater Trans A Phys Metall Mater Sci*, 36(7):1669–1679, 2005.

[169] N. T. Kirkland, N. Birbilis, J. Walker, et al. In-vitro dissolution of magnesium–calcium binary alloys: Clarifying the unique role of calcium additions in bioresorbable magnesium implant alloys. *J. Biomed. Mater. Res.*, 95B(1):91–100, 2010.

[170] Y. Sun, B. Zhang, Y. Wang, et al. Preparation and characterization of a new biomedical Mg–Zn–Ca alloy. *Mater. Des.*, 34:58–64, 2012.

[171] F.-W. Bach, M. Schaper, and C. Jaschik. Influence of lithium on hcp magnesium alloys. *Materials Science Forum*, 419:1037–1042, 2003.

[172] B. Zberg, P. J. Uggowitzer, and J. F. Löffler. MgZnCa glasses without clinically observable hydrogen evolution for biodegradable implants. *Nat. Mater.*, 8(11):887–891, 2009.

[173] M. Cihova, E. Martinelli, P. Schmutz, et al. The role of zinc in the biocorrosion behavior of resorbable Mg–Zn–Ca alloys. *Acta Biomater.*, 100:398–414, 2019.

[174] F. Amerstorfer, S. F. Fischerauer, L. Fischer, et al. Long-term in vivo degradation behavior and near-implant distribution of resorbed elements for magnesium alloys WZ21 and ZX50. *Acta Biomater.*, 42:440–450, 2016.

[175] P. Holweg, L. Berger, M. Cihova, et al. A lean magnesium–zinc–calcium alloy ZX00 used for bone fracture stabilization in a large growing-animal model. *Acta Biomater.*, 113:646–659, 2020.

[176] B. J. Inkson. Scanning electron microscopy (SEM) and transmission electron microscopy (TEM) for materials characterization. In G. Hübschen, I. Altpeter, R. Tschuncky, and H.-G. Herrmann, editors, *Materials characterization using nondestructive evaluation (NDE) methods*, chapter 2, pages 17–43. Woodhead Publishing, Cambridge, UK, 1st edition, 2016.

[177] J. I. Goldstein, D. E. Newbury, D. C. Joy, et al. *Scanning electron microscopy and X-ray microanalysis*. Springer, New York, NY, 3rd edition, 2003.

[178] D. H. Krinsley, K. Pye, J. Boggs, Sam, and N. K. Tovey. *Backscattered scanning electron microscopy and image analysis of sediments and sedimentary rocks*. Cambridge University Press, Cambridge, UK, 2005.

[179] F. A. Shah, K. Ruscsák, and A. Palmquist. 50 years of scanning electron microscopy of bone - a comprehensive overview of the important discoveries made and insights gained into bone material properties in health, disease, and taphonomy. *Bone Res.*, 7(1):1–15, 2019.

[180] A. C. Fischer-Cripps. *Nanoindentation*. Springer, New York, NY, 3rd edition, 2011.

[181] A. Martens. Die Festigkeitseigenschaften und die Härte. In *Handbuch der Materialienkunde für den Maschinenbau*, volume 2, chapter 6, pages 248–418. Springer, Heidelberg, DE, 1st edition, 1912.

[182] W. C. Oliver and G. M. Pharr. An improved technique for determining hardness and elastic modulus using load and displacement sensing indentation experiments. *J. Mater. Res.*, 7(6):1564–1583, 1992.

[183] X. E. Guo and S. A. Goldstein. Vertebral trabecular bone microscopic tissue elastic modulus and hardness do not change in ovariectomized rats. *J. Orthop. Res.*, 18(2), 2000.

[184] F. Haque. Application of nanoindentation development of biomedical to materials. *Surf. Eng.*, 19(4):255–268, 2003.

[185] S. E. Olesiak, M. L. Oyen, and V. L. Ferguson. Viscous-elastic-plastic behavior of bone using berkovich nanoindentation. *Mech. Time-Depend. Mater.*, 14(2):111–124, 2010.

[186] N. Rodriguez-Florez, M. L. Oyen, and S. J. Shefelbine. Insight into differences in nanoindentation properties of bone. *J. Mech. Behav. Biomed. Mater.*, 18:90–99, 2013.

[187] P. K. Zysset. Indentation of bone tissue: A short review. *Osteoporos. Int.*, 20(6):1049–1055, 2009.

[188] T. Jämsä, J. Y. Rho, Z. Fan, et al. Mechanical properties in long bones of rat osteopetrotic mutations. *J. Biomech.*, 35(2):161–165, 2002.

[189] H. S. Gupta, S. Schratter, W. Tesch, et al. Two different correlations between nanoindentation modulus and mineral content in the bone–cartilage interface. *J. Struct. Biol.*, 149(2):138–148, 2005.

[190] L. Mulder, J. H. Koolstra, J. M. den Toonder, and T. M. van Eijden. Relationship between tissue stiffness and degree of mineralization of developing trabecular bone. *J. Biomed. Mater. Res. A*, 84(2):508–515, 2007.

[191] K. I. Schiffmann. Area function calibration in nanoindentation using the hardness instead of Young's modulus of fused silica as a reference value. *Int. J. Mater. Res.*, 98(5):424–429, 2007.

[192] B. J. Briscoe, L. Fiori, and E. Pelillo. Nano-indentation of polymeric surfaces. *J. Phys. D: Appl. Phys*, 31(19):2395–2405, 1998.

[193] T. Chudoba and F. Richter. Investigation of creep behaviour under load during indentation experiments and its influence on hardness and modulus results. *Surf. Coat. Technol.*, 148(2–3):191–198, 2001.

[194] G. Feng and A. H. W. Ngan. Effects of creep and thermal drift on modulus measurement using depth-sensing indentation. *J. Mater. Res.*, 17(3):660–668, 2002.

[195] W. C. Oliver and G. M. Pharr. Measurement of hardness and elastic modulus by instrumented indentation: Advances in understanding and refinements to methodology. *J. Mater. Res.*, 19(1):3–20, 2004.

[196] F. Rupin, A. Saied, D. Dalmas, et al. Experimental determination of young modulus and poisson ratio in cortical bone tissue using high resolution scanning acoustic microscopy and nanoindentation. *J. Acoust. Soc. Am.*, 123(5):3785–3786, 2008.

[197] X. Li and B. Bhushan. A review of nanoindentation continuous stiffness measurement technique and its applications. *Mater. Charact.*, 48(1):11–36, 2002.

[198] A. Faingold, S. R. Cohen, and H. D. Wagner. Nanoindentation of osteonal bone lamellae. *J. Mech. Behav. Biomed. Mater.*, 9:198–206, 2012.

[199] T. Iqbal, B. J. Briscoe, S. Yasin, and P. F. Luckham. Continuous stiffness mode nanoindentation response of poly(methyl methacrylate) surfaces. *Chin. J. Polym. Sci.*, 31(8):1096–1107, 2013.

[200] R. Vayron, E. Barthel, V. Mathieu, et al. Nanoindentation measurements of biomechanical properties in mature and newly formed bone tissue surrounding an implant. *J. Biomech. Eng.*, 134(2):021007, 2012.

[201] E. S. Berkovich. Three-faceted diamond pyramid for studying microhardness by indentation. *Zavod. Lab.*, 13(3):345–347, 1950.

[202] H. Nili, K. Kalantar-Zadeh, M. Bhaskaran, and S. Sriram. In situ nanoindentation: Probing nanoscale multifunctionality. *Prog. Mater. Sci.*, 58(1):1–29, 2013.

[203] A. Leitner. *Advanced nanoindentation techniques for the extraction of material flow curves*. Doctoral dissertation, Montanuniversität Leoben, 2017.

[204] K. Partale. *Einfluss von Belastung und einer Implantatbeschichtung auf die knöcherne Integration von Schanz'Schrauben*. Doctoral dissertation, Freie Universität Berlin, 2003.

[205] K. GmbH. Technovit - Histotechnik, 2022.

[206] P. Sudharshan Phani and W. C. Oliver. A critical assessment of the effect of indentation spacing on the measurement of hardness and modulus using instrumented indentation testing. *Mater. Des.*, 164:107563, 2019.

[207] D. Shindo and T. Oikawa. Energy dispersive X-ray spectroscopy. In *Analytical electron microscopy for materials science*, chapter 4, pages 81–102. Springer, Tokyo, JP, 1st edition, 2002.

[208] D. Vashishth, O. Verborgt, G. Divine, et al. Decline in osteocyte lacunar density in human cortical bone is associated with accumulation of microcracks with age. *Bone*, 26(4):375–380, 2000.

[209] M. C. Chang, C. C. Ko, C. C. Liu, et al. Elasticity of alveolar bone near dental implant-bone interfaces after one month's healing. *J. Biomech.*, 36(8):1209–1214, 2003.

[210] L.-w. Sun, Y.-b. Fan, D.-y. Li, et al. Evaluation of the mechanical properties of rat bone under simulated microgravity using nanoindentation. *Acta Biomater.*, 5(9):3506–3511, 2009.

[211] L. Regele. Vergleich der bioresorbierbaren Magnesiumlegierungen ZX10 und ZX20 als Implantat im Femur der Ratte. Master's thesis, Medizinische Universität Graz, 2017.

[212] M. T. Vestermark, J. E. Bechtold, P. Swider, and K. Søballe. Mechanical interface conditions affect morphology and cellular activity of sclerotic bone rims forming around experimental loaded implants. *J. Orthop. Res.*, 22(3):647–652, 2004.

[213] L. Paar. Evaluation of a magnesium-based implant in the growing rat model. Master's thesis, Medizinische Universität Graz, 2021.

[214] T. Wirth, M. M. Syed Ali, C. Rauer, et al. The blood supply of the growth plate and the epiphysis: A comparative scanning electron microscopy and histological experimental study in growing sheep. *Calcif. Tissue Int.*, 70(4):312–319, 2002.

[215] P. Holweg, V. Herber, M. Ornig, et al. A lean bioabsorbable magnesium-zinc-calcium alloy ZX00 used for operative treatment of medial malleolus fractures. *Bone Joint Res.*, 9(8):477–483, 2020.

[216] P. R. Kuzyk and E. H. Schemitsch. The basic science of peri-implant bone healing. *Indian J. Orthop.*, 45(2):108–115, 2011.

[217] J.-W. Lee, H.-S. Han, K.-J. Han, et al. Long-term clinical study and multiscale analysis of in vivo biodegradation mechanism of Mg alloy. *Proc. Natl. Acad. Sci. USA*, 113(3):716–721, 2016.

[218] F. Witte, V. Kaese, H. Haferkamp, et al. In vivo corrosion of four magnesium alloys and the associated bone response. *Biomaterials*, 26(17):3557–3563, 2005.

[219] P. Fratzl, H. Gupta, F. Fischer, and O. Kolednik. Hindered crack propagation in materials with periodically varying Young's modulus - Lessons from biological materials. *Adv. Mater.*, 19(18):2657–2661, 2007.

[220] H. H. Malluche, D. S. Porter, M.-C. Monier-Faugere, et al. Differences in bone quality in low- and high-turnover renal osteodystrophy. *J. Am. Soc. Nephrol.*, 23(3):525–532, 2012.

[221] R. Zhang, H. Gong, D. Zhu, et al. Multi-level femoral morphology and mechanical properties of rats of different ages. *Bone*, 76:76–87, 2015.

[222] V. Pepe, S. Oliviero, L. Cristofolini, and E. Dall'Ara. Regional nanoindentation properties in different locations on the mouse tibia from C57BL/6 and balb/C female mice. *Front. bioeng. biotechnol*, 8(478):1–8, 2020.

[223] C. Luo, J. Liao, Z. Zhu, et al. Analysis of mechanical properties and mechanical anisotropy in canine bone tissues of various ages. *Biomed Res. Int.*, 2019:3503152, 2019.

[224] A. Schindeler, M. M. McDonald, P. Bokko, and D. G. Little. Bone remodeling during fracture repair: The cellular picture. *Semin. Cell Dev. Biol.*, 19(5):459–466, 2008.

[225] C. Kiernan, C. Knuth, and l. Farrel. Endochondral ossification: Recapitulating bone development for bone defect repair. In M. J. Stoddart, A. M. Craft, G. Pattappa, and O. F. Gardner, editors, *Developmental biology and musculoskeletal tissue engineering*, chapter 6, pages 125–148. Academic Press, Boston, MA, 1st edition, 2018.

[226] E. Hernandez-Becerra, S. M. Londoño-Restrepo, M. I. Hernández-Urbiola, et al. Determination of basal bone mineral density in the femur bones of male and female wistar rats. *Lab. Anim.*, 55(1):30–42, 2021.

[227] J. Zhang, L. Tang, H. Qi, et al. Dual function of magnesium in bone biomineralization. *Adv. Healthcare Mater.*, 8(21):1901030, 2019.

[228] T. A. Grünewald, A. Ogier, J. Akbarzadeh, et al. Reaction of bone nanostructure to a biodegrading Magnesium WZ21 implant – A scanning small-angle X-ray scattering time study. *Acta Biomater.*, 31:448–457, 2016.

List of Figures

List of Tables